SCATTERING AND OPTIMIZATION METHODS FOR RADAR AND MILLIMETER WAVE APPLICATIONS

A Dissertation
Presented to
The Academic Faculty

By

Eric Huang

In Partial Fulfillment
of the Requirements for the Doctor of Philosophy Degree in the
School of Electrical and Computer Engineering
College of Engineering

Georgia Institute of Technology

December 2022

SCATTERING AND OPTIMIZATION METHODS FOR RADAR AND MILLIMETER WAVE APPLICATIONS

Thesis committee:

Dr. Madhavan Swaminathan, Advisor
School of Electrical and Computer Engineering
Georgia Institute of Technology

Dr. Andrew F. Peterson
School of Electrical and Computer Engineering
Georgia Institute of Technology

Dr. Justin Romberg
School of Electrical and Computer Engineering
Georgia Institute of Technology

Dr. Suresh K. Sitaraman
School of Mechanical Engineering
Georgia Institute of Technology

Dr. Saibal Mukhopadhyay
School of Electrical and Computer Engineering
Georgia Institute of Technology

Date approved: December 1st, 2022

ACKNOWLEDGMENTS

Time flies, and now my doctoral degree journey is coming to an end. I still remember myself being nervous and confused at the beginning of the journey worrying about the hardship and challenges. Yet, I am extremely grateful and excited now to be able to present this thesis with pride and confidence. At Georgia Institute of Technology, I was extremely fortunate to be surrounded by many amazing individuals who made this journey joyful. I would like to express my sincere gratitude for all the support. There are too many people to thank.

First, I would like to thank my supervisor, Professor Madhavan Swaminathan. I am grateful to be guided by him for the past few years. Dr. Swaminathan's profound professional knowledge, rigorous academic attitude, and persistence provided me with the opportunities to always learn and improve myself. What I learned benefits me a lot in life. Despite his tight schedule, Professor always took the time to guide my research with enormous care. Thus, I developed the ability to think independently and manage time. I will always keep in mind the academic knowledge and attitude that Professor taught me.

Also, I would like to thank thesis committee members, Dr. Justin Romberg, Dr. Saibal Mukhopadhyay, Dr. Suresh K. Sitaraman, and Dr. Andrew F. Peterson for their time and valuable feedback which improved the quality of this research. They worked tirelessly to review the thesis and provided me with many valuable suggestions. The thesis is thus more completed and rigorous after revision.

I would like to thank everyone who works at 3D Systems Packaging Research Center (PRC), especially Hakki Torun, Majid Ahadi, Mercy Aguebor, Oluwaseyi Akinwande, Osama Bhatti, Yiliang Guo, Seunghyup Han, Yifan Wang, and Rahul Kumar. Although we worked on different research topics, they still provided valuable advice and helped me successfully complete the thesis. I would also like to thank Defense Advanced Research Projects Agency (DARPA) for providing the resources and opportunity to solve problems

that will potentially change the world.

Finally, I would like to express my sincere gratitude to my wife, parents, family, and friends who have supported me. I sincerely appreciate the accompany and enjoyed the experience as a Ph.D. student. This is a memory that I will cherish for a lifetime. I wish you all become your ideal selves, and be safe, healthy, and happy in your future life.

TABLE OF CONTENTS

LIST OF TABLES

LIST OF FIGURES

CHAPTER 1

INTRODUCTION

Throughout the eighteenth century, scientists such as Coulomb, Ampere, Faraday, and Maxwell studied the nature of electricity. In the late nineteenth century, the relationship between electricity and magnetism was also discovered and studied. The electromagnetic (EM) field consists of the electric field and the magnetic field. These fields are perpendicular to each other and are perpendicular to the traveling direction of the wave. The characteristic of a far-field EM wave is defined by the propagating direction, polarization, frequency, magnitude, and phase. Analysis of EM waves from both the signal processing and microwave design sides has grown significantly since the requirements of electronic devices have become stricter in order to serve various applications.

One application of EM analysis is the EM wave propagation and scattering emulation. EM wave emulation has long been studied in the radar communities [1] [2] [3]. There is a growing need to simulate real-time complex EM wave interactions between multiple radar targets, transmitters, and receivers (Figure 1.1). The study will permit the evaluation of radar systems [4], antenna designs [5], and stealth technologies [6]. In radar scenarios, EM waves from transmitters illuminate radar targets. Modulated EM waves are then scattered toward the receivers. The modulation of the scattered signals is determined by the materials and geometry of the radar target, impacting the propagation channel between receivers and transmitters. The radar cross section (RCS) represents the reflection profile of a radar target. It is known as the cross-section area of a perfectly electric reflecting sphere that produces the same reflectivity as the target:

$$\sigma = \lim_{r \to \infty} 4\pi r^2 \frac{S_s}{S_i} \tag{1.1}$$

where S_s is the scattered power density from the target. S_i is the incident power density at the target. r is the distance between the target and the observer. The RCS can also be defined as:

$$\sigma = \lim_{r \to \infty} 4\pi r^2 \frac{|E_s|^2}{|E_i|^2} \tag{1.2}$$

where E_s and E_i are the scattered and incident EM insensitivity, respectively. In addition, RCS can represent the complex numbered reflection profile of a radar target and is an angular dependent frequency response. Monostatic RCS data consists of RCS where the incident angle and scatter angle are identical, while bistatic RCS data consists of RCS where the angles differ as shown in Figure 1.2. The monostatic RCS data is a subset of the bistatic RCS data.

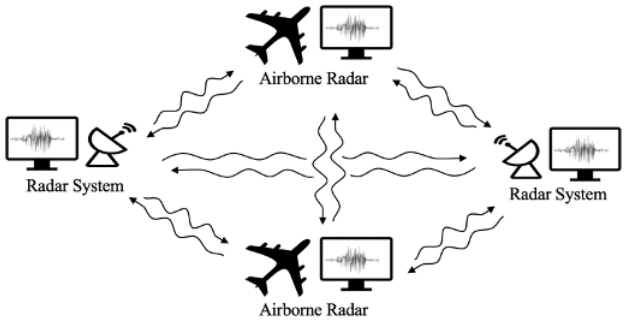

Figure 1.1: Illustration of the real-time EM wave interaction for radar applications

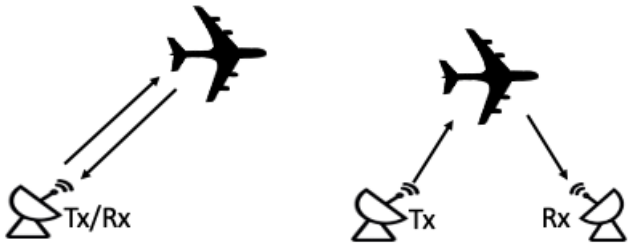

(a) Monostatic (b) Bistatic

Figure 1.2: RCS for two scenarios

High performance computing (HPC) EM emulators can be used to simulate real-time complex EM wave interactions between numerous radar targets. Conventionally, when the HPC EM emulator simulates the scattering effect, the transmitted signal is decomposed

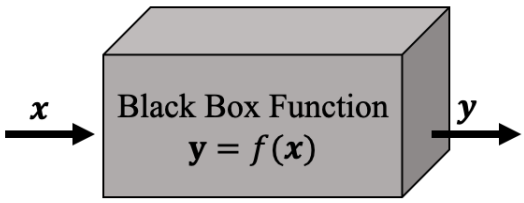

Figure 1.3: Black-boxed function

with Fourier transform. Then, each frequency component is multiplied by the RCS of the scattering target at the aspect angle and corresponding frequencies. The total scattered signal is computed as the summation of these modulated signals. The reflection profiles of radar targets are oftentimes required to be stored as a table. The needed storage size increases linearly with the frequency sampling density and the number of target types used in the emulator. In addition, with denser aspect angle sampling, the needed storage size increases quadratically in the monostatic RCS data and with the fourth power in the bistatic RCS data. The large quantity of data needed often exceeds storage capability and limits the feasibility of manipulation and representation of the objects. We implement optimization methods to compress the data in a way such that the HPC emulators can use it directly as part of the computations.

Another arising application of EM analysis is microwave design optimization problems. The optimization problem can be written as:

$$\min_{\boldsymbol{x}}/\max f(\boldsymbol{x}) \text{ subject to } \boldsymbol{x} \in \mathcal{X} \tag{1.3}$$

where $\boldsymbol{x}$ is the vector of input parameters, $f(\boldsymbol{x})$ is the objective function, and $\mathcal{X}$ is the feasible range of input parameters, also called the design space. Linear and convex optimization problems (LP and CP) can be solved efficiently using iterative methods or linear algebraic techniques due to the properties of simple function surfaces [7] [8]. However, in microwave design scenarios, the nonconvex function surfaces often consist of many local optima and make the optimization problems more challenging. In addition, the black-boxed nature of

the problem (Figure 1.3) indicates the lack of gradient information. In addition, due to the complex EM structures in microwave designs, the function evaluation $f(\boldsymbol{x})$ often requires lengthy EM simulations. We manage to optimize two emerging system designs, namely the beamforming antenna in package design for wireless communication and the wireless power transfer (WPT) for the Internet of Things (IoT), where the dimensionality of the problems to be addressed needs to be quite large.

CHAPTER 2
LITERATURE SURVEY

In this Chapter, methods of radar cross section (RCS) compression are reviewed. The objective of these RCS compression methods is to identify a model that represents the RCS of a given object. Multiple microwave design strategies are also reviewed along with encountered issues while implementing Bayesian optimization to high dimensional design problems.

2.1 Prior Arts for RCS Compression

RCS data is often compressed using the point scatterer model transformation. The point scatterer model, also referred to as the scattering center model, includes the scatterer positions and a reflection profile of each scatterer. Hurst [9] proposed the damped exponential point scatterer model, where the reflection profile is defined as an exponential function that depends on the signal frequency. Potter [10] constructed a geometrical theory of diffraction (GTD) based parametric model, where GTD is an extension of geometrical optics which accounts for diffraction [11]. The GTD-based model also extracts frequency-dependent scattering information. It estimates not only the amplitude of each point scatterer, but also a parameter characterizing the geometry of each point scatterer. Compared to the damped exponential model, the GTD-based model successfully describes more details of the diffraction scattering behaviors.

Bhalla [12] found a 3D point scatterer model based on the shooting and bouncing ray (SBR) technique, which is a ray-tracing algorithm used to simulate the RCS of realistic object models [13]. The 3D image of the object is first computed with the SBR-based inverse synthetic aperture radar (ISAR) algorithm [14] making use of the target motions to create the synthetic aperture. Then, the CLEAN algorithm is used to extract the 3D

positions and strengths of the point scatterers by choosing the dominating points from the image. Gerry [15] also constructed frequency-dependent scatterer models to analyze synthetic aperture radar (SAR) measurements.

Hugh [16] also created the ISAR image to obtain the reflective information of radar objects. The locations of the scatterers are computed with a modified genetic algorithm (GA), which mimics the process of natural selection and improves the performance using mutation, crossover, and selection from a population in the parameter space. Wang and Schuler conducted similar approaches to compute the point scatterer model by extracting the highly reflected areas of the ISAR images [17] [18]. The results show good representations of the highly reflected areas yet ignore the nuances of the detailed reflection profiles of the radar target. Also, these methods represent a small view angle range of the RCS with a large number of scatterers. A binary space partition tree is required to select different point scatterer models according to the aspect angle.

Analyzing the dominant features of a radar object is the most classical method for RCS representation. A complex object can be represented using a number of primitive scattering shapes (plates, cylinders, etc.). Each shape has its own RCS and can be computed analytically [19]. For example, the dominant RCS contribution of an aircraft is from the wings and fuselages. Complex radar targets can also be modeled as a collection of scattering elements randomly distributed throughout the spatial region of the radar target [20]. The randomness of the RCS data can also be represented according to the probability density functions. Delano [21] used this statistical model to analyze RCS and the glints of radar targets.

2.2 Challenges for RCS Compression

The large quantity of storage needed for the RCS data table exceeds the capability and limits the feasibility of manipulation and representation of the objects. The frequency-dependent scatterer models mentioned in the previous section fit the RCS data well. Yet, the

frequency dependency hinders the feasibility of HPC EM emulator computations. More details will be discussed in Chapter 3. In addition, these approaches generate a large number of point scatterers needed for each radar object, which also hinders efficient EM emulations. Although the larger RCS values of radar objects can be captured using primitive scattering shapes, the lower values cannot be captured since the resonance effects are significantly dependent to the complex geometric configuration. We propose to simulate real-time complex EM wave interactions between multiple radar targets, transmitters, and receivers with high performance computing (HPC) based EM emulators. The problem is described by introducing a new perspective of the point scatterer model and channel model used for the HPC EM emulator. Then, a number of innovative approaches for constructing 3D point scatterer models are presented. By defining real numbered and frequency-independent reflection gains, the channel between the EM waves before and after the modulation can be implemented as a finite impulse response (FIR) filter.

2.3 Prior Arts for Microwave Design Optimizations

Beamforming array antennas have been used in 5G/6G wireless communication systems to ease to manufacture process and reduce component failures [22]. Beamforming array antennas electronically steer the beam to the desired direction without physically moving the antennas. This is achieved by the digital beam controllers, which are variable phase shifters behind the array elements. As the operating frequency and number of array elements increase, the negative effect from sidelobes becomes non-negligible and the interference from other radiating sources may degrade the performance of the antenna.

One solution is constructing nonuniform spacing linear antenna array where the parameters are defined as the spacing between array elements of a linear antenna array. Zaman [23] proposed to solve the spacing using the firefly algorithm and a modified particle swarm optimization (PSO) algorithm. PSO is a powerful method for gradient-free optimization problems. In this algorithm, a number of candidates, denoted as particles, are updated iter-

atively using the information of the global optimal particle position and the local optimal particle positions. The particles are guaranteed to converge to the global optima with a sufficiently large number of particles and iterations [24]. The firefly algorithm is the generalized version of the PSO algorithm and mimics the flashing behavior of fireflies [25] [26]. Both algorithms solve the optimization problem by improving a candidate solution with regard to a given evaluation of cost in an iterative fashion. The allowed spacing distance between the elements is constrained to avoid mutual coupling between the elements. The sidelobes reduction can also be achieved by other global optimization approaches as well. Yet, the search spaces of the parameters are usually large and the algorithms become time-consuming due to the large number of iterations.

Another approach for sidelobe nulling is to optimize selected elements in the linear antenna arrays. For example, Mohammed [27] added a small number of controllable elements on each side of the linear antenna array. Then, the beam controllers, which include the amplifiers and phase shifters, of the extra elements are optimized. Furthermore, he proposed to optimize the beam controllers for the extra elements with less computational time using GA. The method can be extended to creating multiple nulls at undesired directions to reduce the unwanted gains towards certain aspect angles. The nulls are created by turning off selected elements in the uniformly spaced linear arrays by means of binary GA [28]. For applications that require large arrays, the cost and size can be reduced by grouping elements into subarrays as shown in Figure 2.1, that form the entire array. To reduce the sidelobes, Haupt [29] computed amplitude tapers for each subarray, where the elements in a subarray are tapered at the same amount. The result shows that the sidelobes are reduced, and the performance can even be further improved with GA. Yang [30] constructed a large antenna array with subarrays of different orientations. The element positions of the subarrays are optimized to obtain low sidelobe levels for the entire antenna using the PSO. The spacing between elements is also constrained in this optimization process to reduce the coupling effect. He further proposed a modified PSO algorithm to solve the optimization

problem with this constraint.

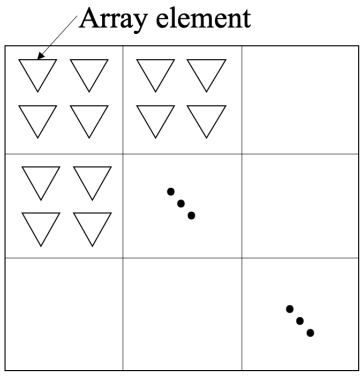

Figure 2.1: Top-view antenna array configuration illustration

A WPT system targets power transmission and conversion without wires or physical links. The power is transmitted through the magnetic fields with inductive couplings by coils. The challenges arise when the coils are operated at high frequency due to the low efficiency and increased power loss [31] [32]. The goal of this design problem is to maximize the RF-to-DC conversion efficiency of IoT devices. Literature shows that increasing the number of power receivers enhances the power transfer efficiency. Yet, it also increases the cost, the number of design parameters, and space wastage of IoT devices. In addition, the crosstalk between multiple receivers interferes the performance [33] [34]. As in the problem of antenna designs, GA and PSO were proposed to optimize the matching capacitors while maximizing the power transfer efficiency [35] [36].

The above mentioned microwave design problems are usually treated as black-boxed functions, where the black-boxed nature of the problems indicates the lack of gradient information. Thus, gradient-free global optimization algorithms have been proposed to solve optimization problems using heuristic methods [37]. For example, GA has also been used for designing the 3-dimensional integrated circuits [38]. It has also shown promising results optimizing the shape and topology of EM structures [39]. Several other applications using PSO for microwave design problems have been discussed as well [40] [41] [42]. Due to the complex EM structures in microwave designs, the function evaluation often requires

lengthy EM simulations. The accumulated computation time hinders the feasibility of GA and PSO due to the large number of iterations that these algorithms require. Bayesian Optimization (BO) is a machine learning based method that enables fast convergence towards a global optimum and is well-known for reducing the computation time by efficient sampling. This is achieved by fitting a probabilistic surrogate model with existing data and optimizing the acquisition function to decide the next sampling point in a heuristic manner. This method has shown promising optimization results for functions without closed-form expressions [43] [44] [45].

2.4 Challenges for Microwave Design Optimizations

A general problem with BO is the low dimensionality of the problem that needs to be addressed which is contrary to microwave design that often requires many parameters to be optimized with precision. The challenges of implementing conventional BO to high dimensional problems are due to the curse of dimensionality [46] [47]. For example, the search space expands exponentially as the number of input parameters increases. Thus, the surrogate models cannot well represent a function without an extremely large number of data. This is infeasible for microwave designs due to the CPU-intensive and time-consuming EM simulations. In addition, the acquisition function optimization becomes unsolvable or time-consuming, which leads to poor suggestions of the next sampling point. Existing literature suggests a high to low dimensional linear mapping to the input space [48] [49]. However, this linear mapping is oftentimes not obtainable and provides unstable solutions. Also, applying a linear mapping to a function without such linear characteristics leads to poor function approximation. Another common solution to high dimensional BO problems is assuming additive structures [50] [51], which assumes that the objective function is decomposed into a summation of multiple low dimensional functions. Yet again, this decomposition is not always obvious. We propose an innovative method that prioritizes a subset of the design parameters for GP regression and acquisition function optimization in

each iteration, where the subset selections are based on the estimated sensitivity of each parameter to the objective function. This process is then applied to two emerging system designs, namely the beamforming antenna in package design for wireless communication and the wireless power transfer for Internet of Things (IoT).

In the following chapters, we present a number of innovative approaches for constructing concise point scatterer models that the HPC EM emulators can use as part of the computations to solve the RCS compression problem. To solve the high dimensional black-boxed microwave design problems, we propose an innovative method that prioritizes a subset of the design parameters for GP regression and acquisition function optimization in each iteration, where the subset selections are based on the estimated sensitivity of each parameter to the objective function.

CHAPTER 3

POINT SCATTERER MODELS

Electromagnetic (EM) wave propagation and scattering emulation have long been studied in the radar communities. High performance computing (HPC) based EM emulators are used to simulate real-time complex EM wave interactions between multiple radar targets, transmitters, and receivers. We describe the problem by introducing the point scatterer model and the channel model used for the HPC EM emulator. Then, a number of innovative approaches for constructing 3D point scatterer models are presented.

3.1 Problem Description

The reflection profile of a radar target can be represented as a point scatterer model, which consists of a number of isotropic or anisotropic scatterers. An isotropic scatterer modulates and scatters signals identically in all directions, while an anisotropic scatterer modulates and scatters signals differently depending on the aspect angle. The aspect angle consists of the incident angle and the scatter angle. The incident angle indicates the direction of where the signal is illuminating the scatterer from. The scatter angle indicates the direction

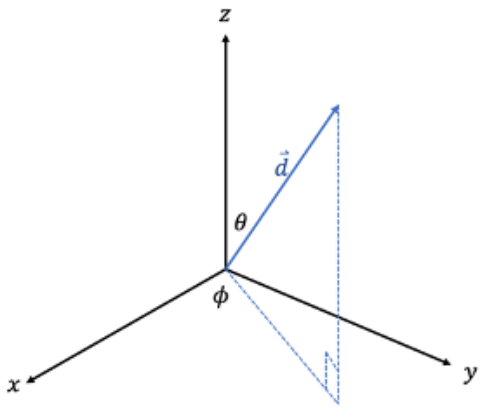

Figure 3.1: Spherical coordinate illustration

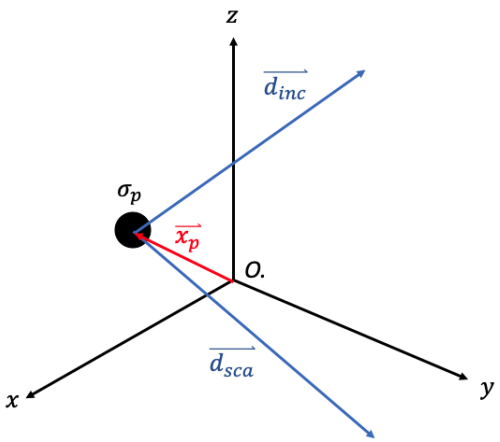

Figure 3.2: Single scatterer example

of the scattered signal. The incident angle and scatter angle are represented in elevation $0 \leq \theta \leq \pi$ and azimuth $0 \leq \phi < \pi$ using spherical coordinates as shown in Figure 3.1 and are denoted by $\boldsymbol{\Psi}_{inc} = [\theta_{inc}, \phi_{inc}]^T$ and $\boldsymbol{\Psi}_{sca} = [\theta_{sca}, \phi_{sca}]^T$, respectively. We denote the unit vectors of the incident angle and the scatter angle direction in Cartesian coordinates as $\boldsymbol{d}_{inc}$ and $\boldsymbol{d}_{sca}$, respectively. As shown in Figure 3.2, the point scatterer model possesses a local coordinate origin in the 3D space. The position of each scatterer p is $\boldsymbol{x}_p$. τ_p is the time delay between the signal illuminating scatterer p and the signal illuminating the scatterer at the origin as shown in

$$\tau_p = \frac{-\left(\langle \boldsymbol{x}_p, \boldsymbol{d}_{inc} \rangle + \langle \boldsymbol{x}_p, \boldsymbol{d}_{sca} \rangle\right)}{c} \tag{3.1}$$

where c represents the speed of light and $\langle \cdot, \cdot \rangle$ is the standard inner product in $\mathbb{R}^3$.

The RCS, namely the reflection frequency response, of the point scatterer model is shown in Equation 3.1. It is important to note that Equation 3.1 accounts for the propagation from the transmitter to the scatterer and the propagation from the scatterer scattering back to the receiver.

$$G\left(f; \boldsymbol{\Psi}_{inc}, \boldsymbol{\Psi}_{sca}\right) = \sum_{p=1}^{K} \sigma_p e^{-i2\pi f \tau_p} = \sum_{p=1}^{K} \sigma_p e^{i2\pi f (\langle \boldsymbol{x}_p, \boldsymbol{d}_{inc} \rangle + \langle \boldsymbol{x}_p, \boldsymbol{d}_{sca} \rangle)/c} \tag{3.2}$$

In Equation 3.2, K is the total number of scatterers, σ_p is the frequency-independent reflec-

tion gain of the p^{th} scatterer and f is the signal frequency. The σ of the isotropic scatterers are identical across all aspect angles, while the σ of the anisotropic scatterers depend on $\mathbf{\Psi}_{inc}$ and $\mathbf{\Psi}_{sca}$. Constructing an isotropic point scatterer model means finding the positions $\boldsymbol{x}$ and the angular independent reflection gains σ for all K scatterers, while constructing an anisotropic point scatterer model means finding the positions $\boldsymbol{x}$ and the angular dependent reflection gains $\sigma\left(\mathbf{\Psi}_{inc}, \mathbf{\Psi}_{sca}\right)$ for all K scatterers, which best represent a given radar target.

3.2 Defining the Channel Models

There are two channel models to choose from while simulating the EM propagation, namely the path delay model and the scatterer separable model. The fundamental concepts of these channel models are addressed below.

3.2.1 Path Delay Model

The path delay model views each end-to-end propagation path as a channel as shown in Figure 3.3. The channel starts with a transmitter sending signals to a radar target. The target then scatters the modulated signals to another target. The signals are repeatedly scattered until a receiver receives the end signals. As shown in Equation 3.3, the bistatic scattered frequency response is dependent to both the incident and scatter angles. The channel model can include multiple objects.

$$G(f; \mathbf{\Psi}_{inc}, \mathbf{\Psi}_{sca}) = \sum_{p=1}^{K} \alpha_p(\mathbf{\Psi}_{inc}, \mathbf{\Psi}_{sca}) e^{-i2\pi f(-(\langle \mathbf{x}_p, \mathbf{d}_{inc} \rangle + \langle \mathbf{x}_p, \mathbf{d}_{sca} \rangle)/c)} \tag{3.3}$$

3.2.2 Scatterer Separable Model

In the separable channel model, each transmitter, target, or receiver is represented as an object that receives and/or transmits signals as shown in Figure 3.4. Each pair of two objects defines a channel. The received signals of an object come from all other objects in the

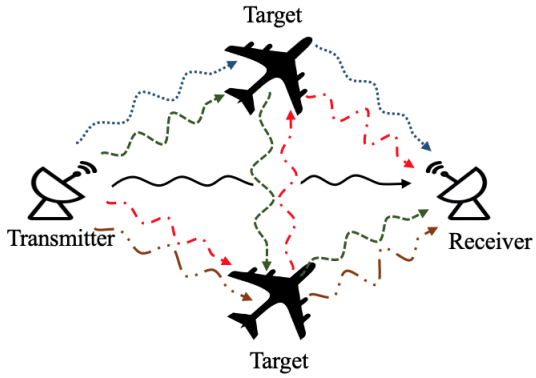

Figure 3.3: Path Delay Model

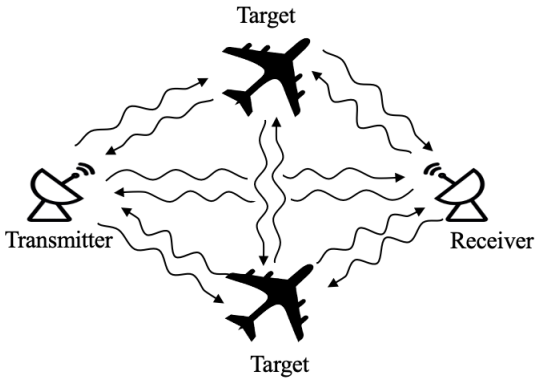

Figure 3.4: Scatterer Separable Model

EM environment. The transmitted signals of an object include the signal generated from its own source and the scattered signals. The modulation of the scattered signals is determined by the point scatterer model of the illuminated object as described in Equation 3.4. It is important to note that the reflection gains should be two separable functions of the incident and scatter angles, respectively. This model is primarily used when the number of radar targets is large or when accounting for signals that are scattered multiple times.

$$G(f;\boldsymbol{\Psi}_{inc},\boldsymbol{\Psi}_{sca}) = \sum_{p=1}^{K} \alpha_{inc,p}(\boldsymbol{\Psi}_{inc})\alpha_{sca,p}(\boldsymbol{\Psi}_{sca})e^{-i2\pi f(-(\langle \mathbf{x}_p,\mathbf{d}_{inc}\rangle+\langle \mathbf{x}_p,\mathbf{d}_{sca}\rangle)/c)} \tag{3.4}$$

By defining real numbered and frequency-independent reflection gains, the channel

between the EM waves before and after the modulation can be implemented as a finite impulse response (FIR) filter with K taps, where the tap locations are defined based on the scatterer locations, and the tap coefficients are defined based on the reflection profiles of the scatterers. In other words, when simulating the scenario of an object scattering EM signals back to a radar, the signal received by the radar can be computed by passing through the transmitted signal through the FIR filter. When K is reduced, the simulation of the scattering effects can be performed efficiently in the hardware.

The complex numbered angular dependent frequency response, namely the RCS, denotes the magnitude and phase changes of the scattered far-field EM wave signal after the EM wave interacts with the radar target. The RCS of a target can be either measured from the real object [52] or generated approximately using an EM field simulation software such as CST Studio Suite which uses physical optics-based methods [53][54]. Our objective is to find a point scatterer model which has frequency-independent reflection gains, where the point scatterer model best represents such RCS data.

3.3 Constructing the Scatterer Models

We proposed two modeling methods that are suitable for the path delay channel model:

- Shape Approximation
- Anisotropic Ellipsoid Scatterer Model

In addition, we proposed two modeling methods suitable for the scatterer separable channel model:

- Isotropic Sphere Point Scatterer Model
- Spherical Harmonic based Anisotropic Point Scatterer Model

3.3.1 Shape Approximation

A complex object can be represented using a number of simple shapes (plates, cylinders, etc.), each with its own RCS, which can be computed analytically. Although the larger values of the RCS data of objects can be captured using this approach, the lower values cannot be captured since the resonance effects are significantly dependent to the complex geometric configuration. We therefore further propose constructing a more accurate scatterer model using the RCS data of objects available from the EM solvers by solving a nonlinear least square optimization problem.

3.3.2 Isotropic Sphere Point Scatterer Model and Anisotropic Ellipsoid Scatterer Model

In the isotropic sphere point scatterer model, each scatterer point is represented as a perfect electric conductor (PEC) smooth sphere with radius r. The analytical RCS representation of the scatterer is πr^2 and the reflection gain is $\sqrt{\pi r^2}$, which are constant at all aspect angles. The scatterer separable model can be computationally efficient with the isotropic scatterer model due to its separable property. We define the scatterer locations in the local coordinate system and the radii of the spheres as control variables.

Besides spheres, other simple shapes such as plates and cylinders with anisotropic scattering properties also have analytical RCS solutions. However, only the RCS of an ellipsoid is frequency-independent, which is consistent with the channel models shown in Equation 3.3 and Equation 3.4. Therefore, we use the analytical RCS representation of a large PEC ellipsoid shown in Equation 3.5, where a, b, and c represent the principal semi-axes of the ellipsoid, as the basis function to determine the angular dependency of the RCS of each scatterer [55]. Anisotropic scatterer models capture the reflection features better because the ellipsoid model has high degrees of freedom as compared to the spherical model. We define the scatterer locations, principal semi-axes, and rotation angles (defined as the offset angles of θ and ϕ) of the ellipsoids as control variables.

$$\frac{4\pi a^2 b^2 c^2[(1+cos\theta_{inc}cos\theta_{sca})cos(\phi_{sca}-\phi_{inc})+sin\theta_{inc}sin\theta_{sca}]^2}{[a^2(sin\theta_{sca}cos\phi_{sca}+sin\theta_{inc}cos\phi_{inc})^2+b^2(sin\theta_{sca}sin\phi_{sca}+sin\theta_{inc}sin\phi_{inc})^2+c^2(cos\theta_{sca}+cos\theta_{inc})^2]^2} \quad (3.5)$$

The reflection frequency responses of both scatterer models can be computed as described in Section 3.1, where α_p is computed using Equation 3.6, and the model RCS, σ_{Model}, is computed using Equation 3.7:

$$\alpha_p = \sqrt{\sigma_p} \quad (3.6)$$

$$\sigma_{Model} = |G(f; \mathbf{\Psi}_{inc}, \mathbf{\Psi}_{sca})|^2 \quad (3.7)$$

where σ_p is the RCS of the p^{th} sphere or ellipsoid. Ellipsoid scatterer models are limited to the path delay channel model where its RCS fidelity is more accurate than the isotropic point scatterer model.

Using the RCS data of the radar target, the problem is then posed as a least square inverse problem with the loss function of a root mean square error (RMSE) between the RCS data (from EM simulations) and the RCS of the point scatterer model as shown in Equation 3.8:

$$Loss\ Function = \sqrt{\frac{1}{N}\sum[10log(\sigma_{True}) - 10log(\sigma_{Model})]^2} \quad (3.8)$$

where σ_{True} and σ_{Model} represent the vectors consisting of the RCS data (from EM simulations) and the RCS of the scatterer model, respectively, and N represents the length of the vector. It is important to note that the vectors are the RCS values evaluated at all frequency and aspect angle samples.

Since the RCS data at different aspect angles is significantly affected by the complex geometric configuration, it is difficult to obtain a highly correlated result even if the number of scatterer points is increased. We therefore divide the model into multiple regions, where

each region covers a set of aspect angles. The RCS at each region is then represented by a point scatterer model. We call this the "shadowing effect" since a radar target should be represented using different point scatterer models at different aspect angles. For example, if the incident and scatter angles are both on the front side of the radar target, the back side of the target is shadowed, and only the front side geometry of the target contributes to the reflection. Thus, a single optimization problem may be decomposed into multiple problems, each with a smaller N.

Ellipsoid Model Simulation Results

We demonstrate the feasibility of the proposed approach using the monostatic RCS data of a 60-meter-long aircraft made up of PEC. The incident and scatter angles are the same. The aircraft geometry STL file is obtained from [56] and is shown in Figure 3.5. The RCS data is generated from the EM simulator CST Studio Suite [53] [57] with horizontal polarization at the 3 frequencies of 1GHz, 1.5GHz, and 2GHz. The angle sampling increment is 10 degrees for both θ and ϕ. We consider the shadowing effect by equally dividing the aspect angles into 4 regions as shown in Figure 3.6 and discuss 6 cases:

(i) 16 isotropic point scatterer model without considering the shadowing effect.

(ii) 4 isotropic point scatterer model for each region.

(iii) 16 isotropic point scatterer model for each region.

(iv) 16 anisotropic point scatterer model without considering the shadowing effect.

(v) 4 anisotropic point scatterer model for each region.

(vi) 16 anisotropic point scatterer model for each region.

These case definitions are also shown in Table 3.1. We use the Sequential Quadratic Programming solver in MATLAB [58]. The initial settings are shown in Table 3.2. The ellipsoid model of case (i) is shown in Figure 3.7. When using the anisotropic point scatterer

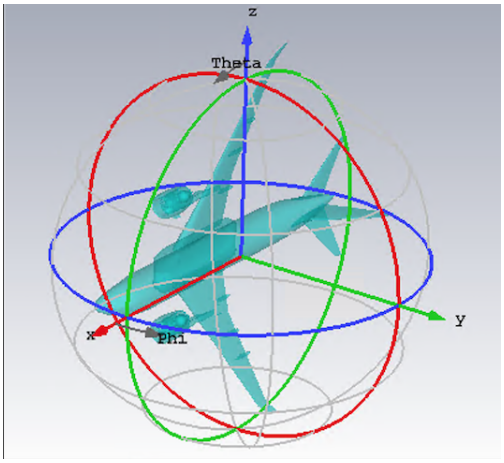

Figure 3.5: Aircraft Geometry

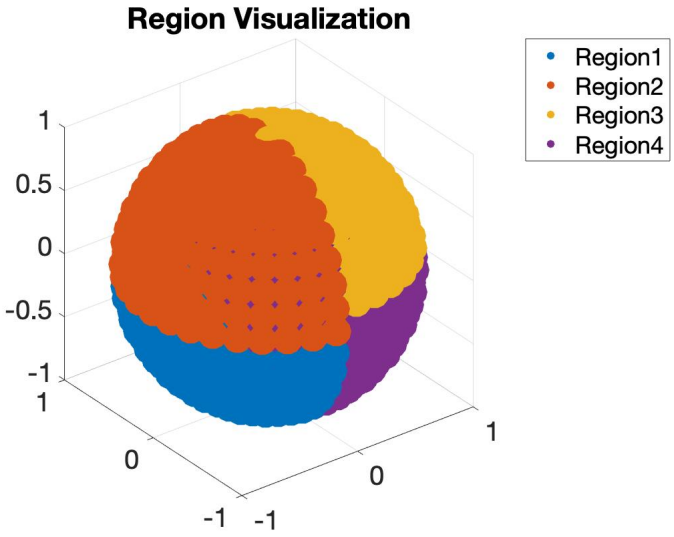

Figure 3.6: Region division visualization

model without considering the shadowing effect, as the number of ellipsoids increases, the RMSE decreases steadily and the computation time steadily increases, as shown in Figure 3.8. Figure 3.9 presents comparison results of the RCS data from CST Studio Suite and the modeled RCS in an image form. Figure 3.10 shows the 2D polar plot matching results for the RCS data from CST Studio Suite and the modeled RCS at $\theta = 0^\circ$ and $\phi = -90^\circ$. Table 3.3 shows the RMSE results of all cases.

Table 3.1: Case models definition

Case Number	**Scatterer Type**	**Shadowing Effect**	**Number of Points**
i	Isotropic	Not considered	16
ii	Isotropic	4 region, 4 point/region	16
iii	Isotropic	4 region, 16 point/region	64
iv	Anisotropic	Not considered	16
v	Anisotropic	4 region, 4 point/region	16
vi	Anisotropic	4 region, 16 point/region	64

Table 3.2: Initial settings

	Isotropic Model	**Anisotropic Model**
Initial Positions	[0, 0, 0]	[0, 0, 0]
Initial Radii/ Semi-Axes	1m	[1, 1, 1]m
Initial Rotations	NA	$[0^\circ, 0^\circ]$
Position Bounds	$[-10 - 10]$	$[-10 - 10]$
Radii Bounds	$[10^{-5} - 15]$m	$[10^{-5} - 15]$m
Rotations Bounds	NA	$[-45^\circ - 45^\circ]$

The anisotropic scatterer model exhibits better fitting than the isotropic scatterer model since cases (i), (iii), and (v) results in lower RMSE compared to cases (ii), (iv), and (vi), respectively. For the same point number, though the shadowing effect results provide a better correlation in the anisotropic case, it does not improve the results in the isotropic case. This may be due to the lack of degrees of freedom used in the spherical isotropic model. Anisotropic scatterer models are limited to the path delay channel model. The

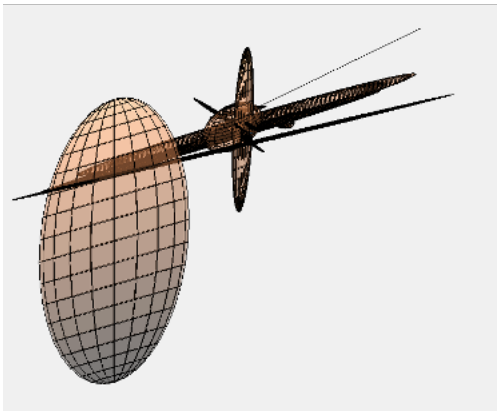

Figure 3.7: Ellip model of case (i)

Table 3.3: RMSE comparison between different models

Case Number	RMSE
i	6.71
ii	6.78
iii	5.25
iv	5.97
v	5.43
vi	3.93

downside of the path delay model is that it is only applicable to a small number of radar targets. Yet, its RCS fidelity is more accurate than that of the isotropic point scatterers.

To conclude the isotropic sphere and anisotropic ellipsoid scatterer modeling, we presented an innovative approach for representing objects using a 3D point anisotropic scatterer model for use in a radar HPC emulator. Anisotropic point scatterer models are more accurate than that of the isotropic point scatterers. The scatterer model that best represents the RCS data is obtained by solving a least square inverse problem. To improve the correlation with EM solvers, we further break down the optimization problem by considering the shadowing effect and using multiple models to represent a subset of the RCS data. The results show that the anisotropic scatterer model can effectively represent the RCS data of complex targets. More detailed information can be found in our conference paper [59]. Another anisotropic point scatterer model based on spherical harmonic functions is discussed in the next Chapter. The reflection gains of the model are defined to be both

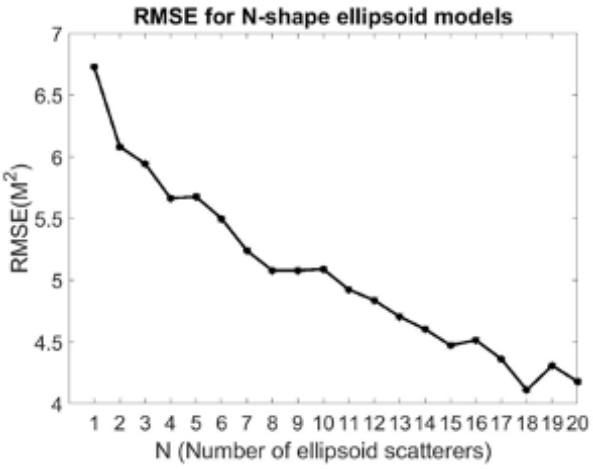

(a) Effects on RMSE

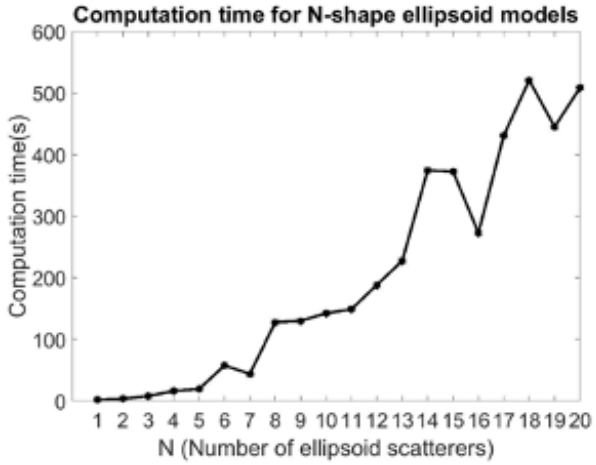

(b) Effects on computation time

Figure 3.8: The effects of increasing the ellipsoid scatterer number when not considering the shadowing effect

frequency-independent and separable, thus is suitable for the separable channel models.

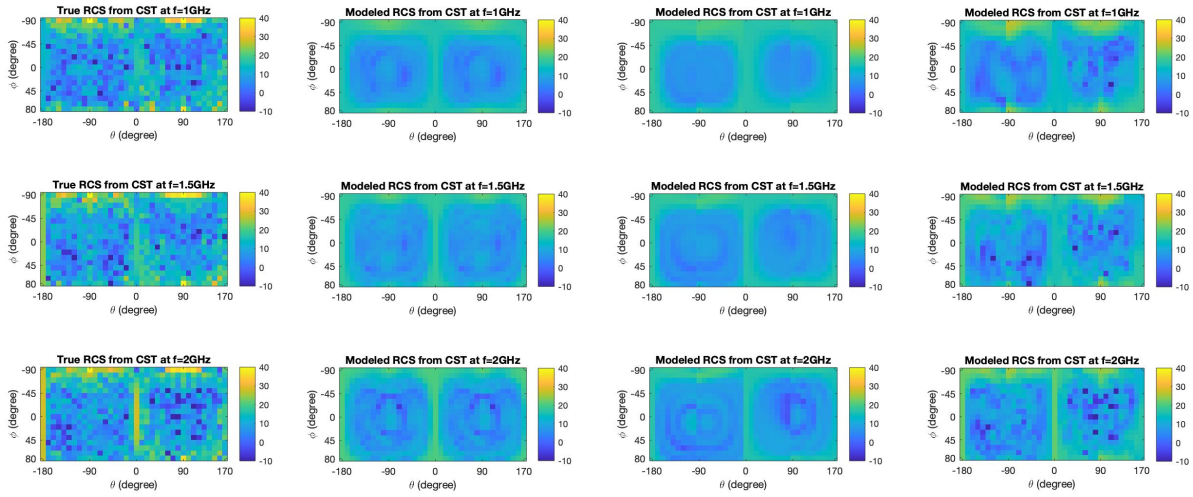

(a) True RCS from CST (b) Case i (c) Case ii (d) Case iii

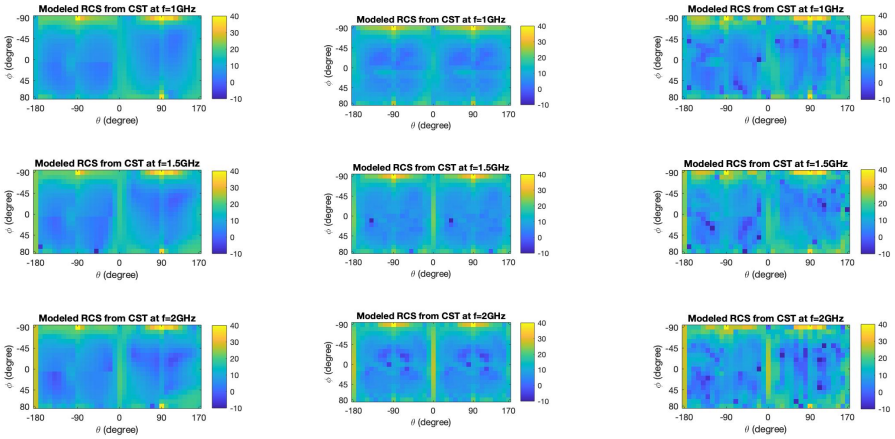

(e) Case iv (f) Case v (g) Case vi

Figure 3.9: Images of the RCS data at frequencies 1GHz, 1.5GHz, and 2GHz from top to bottom, respectively

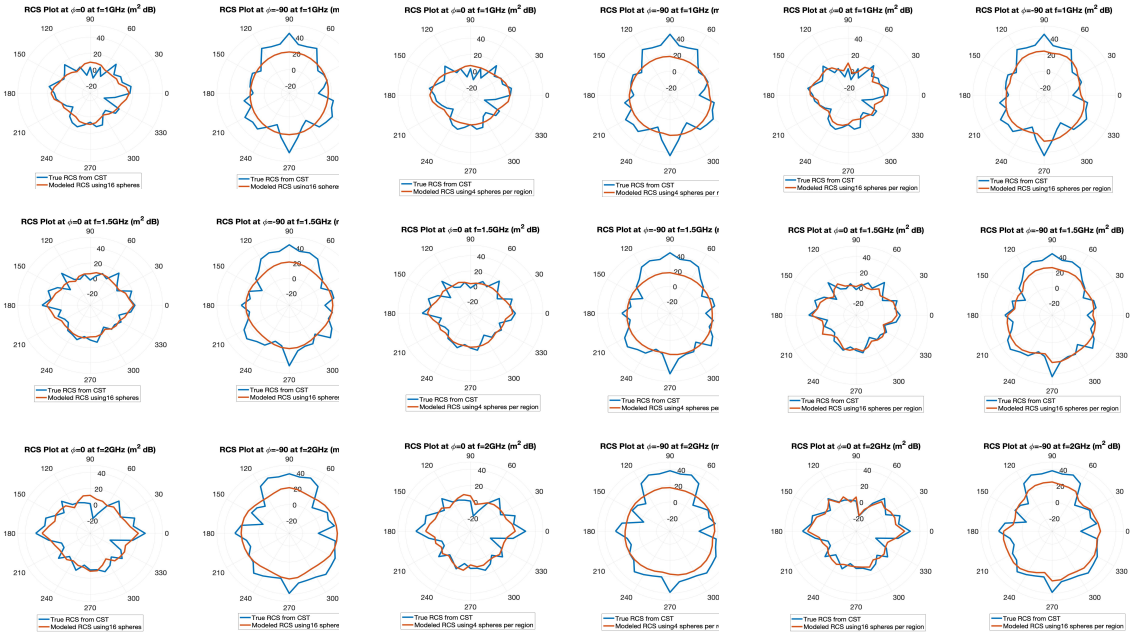

(a) Case i (b) Case ii (c) Case iii

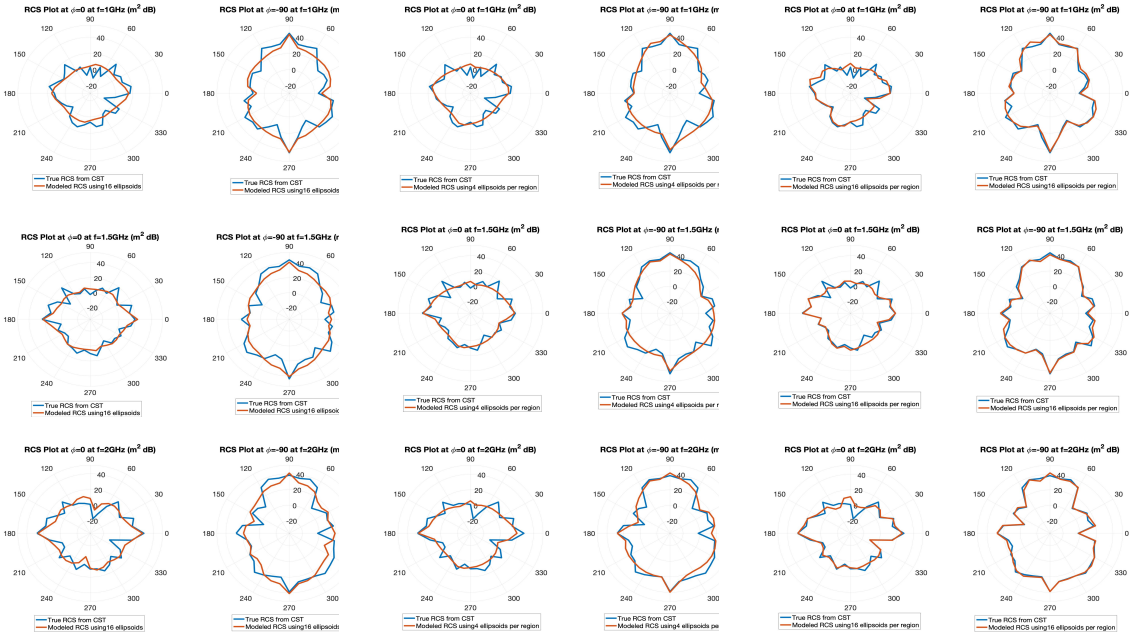

(d) Case iv (e) Case v (f) Case vi

Figure 3.10: 2D polar plot of the RCS data at frequencies 1GHz, 1.5GHz, and 2GHz from top to bottom, respectively

CHAPTER 4
SPHERICAL HARMONIC BASED ANISOTROPIC POINT SCATTERER MODEL

So far, we developed an anisotropic point scatterer model using the RCS of ellipsoids as basis functions [59]. By varying the sizes and shapes of the ellipsoids, the RCS power of an object is captured. In this section, we present another innovative approach for constructing a spherical harmonic based anisotropic 3D point scatterer model from the precomputed RCS data. This inverse problem is solved as an optimization problem. This model is constructed off-line and can be used by the HPC EM emulator to simulate EM wave interactions in real-time. This proposed model outperforms the isotropic sphere and anisotropic ellipsoid scatterer models in three aspects:

1. Spherical harmonic functions are orthogonal, therefore the spherical function that represents the RCS can be approximated better.

2. The spherical harmonic based bistatic RCS model is separable.

3. The proposed model captures the complex-numbered RCS data while the ellipsoid model captures only the RCS power.

Recall that a non-separable channel model considers each path of a transmitter, target, and receiver as a channel and makes use of the function $\sigma\left(\mathbf{\Psi}_{inc}, \mathbf{\Psi}_{sca}\right)$ in the simulation. The separable channel model, on the other hand, enables the HPC EM emulator to more efficiently simulate the EM wave interactions between multiple radar targets by separating the reflection gain σ into two spherical functions of the incident and scatter angles, respectively, as shown below:

$$\sigma_p\left(\mathbf{\Psi}_{inc}, \mathbf{\Psi}_{sca}\right) = \sigma_{inc,p}\left(\mathbf{\Psi}_{inc}\right)\sigma_{sca,p}\left(\mathbf{\Psi}_{sca}\right) \tag{4.1}$$

In the separable channel model, each transmitter, target, or receiver is represented as an object that receives and/or transmits signals. The received signals of an object come from all other objects in the EM environment. The transmitted signals of an object include the signal generated from its own source and the scattered signals. The modulation of the scattered signals is determined by the point scatterer model of the illuminated object as described in Equation 3.3. By defining real numbered and frequency independent reflection gains, the channel between the EM waves before and after the modulation can be implemented as a finite impulse response (FIR) filter with K taps, where the tap locations are defined based on the scatterer locations, and the tap coefficients are defined based on the reflection profiles of the scatterers. In other words, when simulating the scenario of an object scattering EM signals to a radar receiver, the signal received by the radar can be computed by passing through the transmitted signal through the FIR filter. When K is reduced, the simulation of the scattering effects can be performed efficiently in the hardware.

Since we use spherical harmonics as the basis for the spherical functions, the mathematical foundation of spherical harmonics is presented.

4.1 Spherical Harmonic

Spherical harmonic functions are well studied in mathematics and physical sciences [60][61]. We propose to use spherical harmonic functions to construct the reflection gains σ_{inc} and σ_{sca} of each scatterer. That is, we assume that σ_{inc} and σ_{sca} of each scatterer are linear combinations of a finite number of spherical harmonics. Consider the real numbered vector space of square integrable functions $f(\theta, \phi)$ defined on the unit sphere or 2-sphere $S^2 \triangleq \{\boldsymbol{u} \in \mathrm{R}^3 : |\boldsymbol{u}| = 1\}$, where $|\cdot|$ denotes the Euclidian norm. This spherical vector space is parameterized by the elevation $0 \leq \theta \leq \pi$ and azimuth $0 \leq \phi < 2\pi$, and is a Hilbert space with a valid inner product

$$\langle f_1, f_2 \rangle = \int_{\theta=0}^{\pi} \int_{\phi=0}^{2\pi} f_1(\theta,\phi) f_2(\theta,\phi) \sin\theta d\phi d\theta \tag{4.2}$$

Real numbered spherical harmonic functions $Y_l^m(\theta,\phi)$ of all degrees $l \geq 0$ and orders $-l \leq m < l$ form a complete orthonormal sequence of the spherical vector space as shown in Figure 4.1. The spherical harmonics are defined as

$$Y_{lm}(\theta,\phi) = \begin{cases} \bar{P}_{lm}(\cos\theta)\cos m\phi & \text{if } m \geq 0 \\ \bar{P}_{l|m|}(\cos\theta)\sin|m|\phi & \text{if } m < 0 \end{cases} \tag{4.3}$$

where the normalized associated Legendre functions $\bar{P}_{lm}$ are given by

$$\bar{P}_{lm}(\mu) = \sqrt{(2-\delta_{m0})(2l+1)\frac{(l-m)!}{(l+m)!}} P_{lm}(\mu) \tag{4.4}$$

and δ_{ij} is the Kronecker delta function. The unnormalized associated Legendre functions are derived from the standard Legendre polynomials using the relations

$$P_{lm}(\mu) = \left(1-\mu^2\right)^{m/2} \frac{d^m}{d\mu^m} P_l(\mu) \tag{4.5}$$

$$P_l(\mu) = \frac{1}{2^l l!} \frac{d^l}{d\mu^l} \left(\mu^2 - 1\right)^l \tag{4.6}$$

Basically, any spherical function can be decomposed into a sum of the orthonormal basis $f(\theta,\phi) = \sum_{l=0}^{\infty} \sum_{m=-l}^{l} c_l^m Y_l^m(\theta,\phi)$, where c_l^m is the coefficient of the corresponding $Y_l^m(\theta,\phi)$. By assuming that the spherical functions which represent the reflection gains, namely σ_{inc} and σ_{sca}, of each scatterer are linear combinations of a finite number of spherical harmonics, the problem becomes finding the spherical harmonic coefficients.

The complex numbered angular dependent frequency response, namely the RCS, denotes the magnitude and phase changes of the scattered far-field EM wave signal after the EM wave interacts with the radar target. The RCS of a target can be either measured from

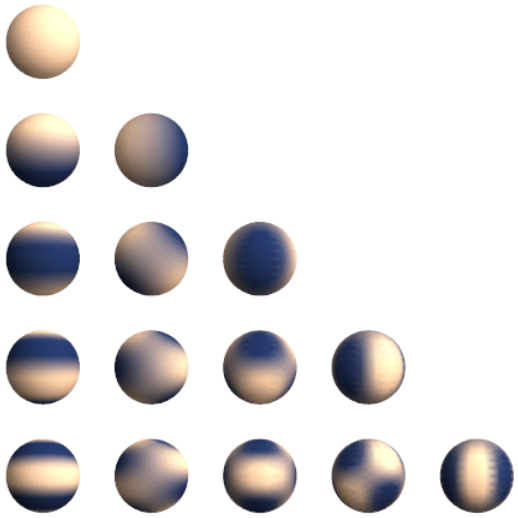

Figure 4.1: Spherical harmonic functions (figure from Wikipedia)

the real object [52] or generated approximately using an EM field simulation software such as CST Studio Suite which uses physical optics-based methods [54] [57]. Our objective is to find a point scatterer model which has separable and frequency-independent reflection gains, where the point scatterer model best represents such RCS data. Next, we illustrate methods to find the model by solving the position and the spherical harmonic coefficients of each scatterer.

4.2 Constructing the Scatterer Model for Monostatic RCS Data

In this section, we use the monostatic RCS data, to solve the positions and spherical harmonic coefficients of the scatterers. Since in the monostatic RCS data, the incident angle and the scatter angles are the same, we define $\mathbf{\Psi} = \mathbf{\Psi}_{inc} = \mathbf{\Psi}_{sca}$ and $\sigma(\mathbf{\Psi}) = \sigma_{inc}\left(\mathbf{\Psi}_{inc}\right)\sigma_{sca}\left(\mathbf{\Psi}_{sca}\right)$ for each scatterer. The problem is formulated as a linear least squares problem which has a constraint. We solve this problem with a modified orthogonal matching pursuit (OMP) algorithm.

4.2.1 Least Squares Linear Problem

Two assumptions are made:

1. The angular dependent reflection gain $\sigma(\mathbf{\Psi})$ of each anisotropic scatterer is a linear combination of $Y_l^m(\theta, \phi)$ with degree L. The number of spherical harmonics is $H = (L+1)^2$.

2. A finite number, $\bar{K}$, of possible scatterer positions are known. For example, we assume that all scatterers are located in a 10m×10m×10m grid in the local coordinate system. That is, we assume the components of $\boldsymbol{x}$ of each scatterer are integers between 0 and 10.

With these assumptions, solving the scatterer positions and the spherical harmonic coefficients becomes a linear least squares problem with a sparsity constraint. The problem is defined in Equation 4.7∼Equation 4.11.

$$\bar{S}\boldsymbol{\alpha} = \overline{\boldsymbol{r}} \tag{4.7}$$

$$\begin{bmatrix} S_{Re} \\ S_{Im} \end{bmatrix} \boldsymbol{\alpha} = \begin{bmatrix} \boldsymbol{r}_{Re} \\ \boldsymbol{r}_{Im} \end{bmatrix} \tag{4.8}$$

$$S = \begin{bmatrix} e^{-i2\pi f_1 \tau(\boldsymbol{x}_1, \mathbf{\Psi}_1)} Y_1(\mathbf{\Psi}_1) & \dots & e^{-i2\pi f_1 \tau(\boldsymbol{x}_1, \mathbf{\Psi}_1)} Y_H(\mathbf{\Psi}_1) & e^{-i2\pi f_1 \tau(\boldsymbol{x}_2, \mathbf{\Psi}_1)} Y_1(\mathbf{\Psi}_1) & \dots & e^{-i2\pi f_1 \tau(\boldsymbol{x}_{\bar{K}}, \mathbf{\Psi}_1)} Y_H(\mathbf{\Psi}_1) \\ \vdots & \ddots & \vdots & \vdots & \ddots & \vdots \\ e^{-i2\pi f_m \tau(\boldsymbol{x}_1, \mathbf{\Psi}_m)} Y_1(\mathbf{\Psi}_m) & \dots & e^{-i2\pi f_m \tau(\boldsymbol{x}_1, \mathbf{\Psi}_m)} Y_H(\mathbf{\Psi}_m) & e^{-i2\pi f_m \tau(\boldsymbol{x}_2, \mathbf{\Psi}_m)} Y_1(\mathbf{\Psi}_m) & \dots & e^{-i2\pi f_m \tau(\boldsymbol{x}_{\bar{K}}, \mathbf{\Psi}_m)} Y_H(\mathbf{\Psi}_m) \\ \vdots & \ddots & \vdots & \vdots & \ddots & \vdots \\ e^{-i2\pi f_F \tau(\boldsymbol{x}_1, \mathbf{\Psi}_M)} Y_1(\mathbf{\Psi}_M) & \dots & e^{-i2\pi f_F \tau(\boldsymbol{x}_1, \mathbf{\Psi}_M)} Y_H(\mathbf{\Psi}_M) & e^{-i2\pi f_F \tau(\boldsymbol{x}_2, \mathbf{\Psi}_M)} Y_1(\mathbf{\Psi}_M) & \dots & e^{-i2\pi f_F \tau(\boldsymbol{x}_{\bar{K}}, \mathbf{\Psi}_M)} Y_H(\mathbf{\Psi}_M) \end{bmatrix} \tag{4.9}$$

$$\boldsymbol{\alpha} = \begin{bmatrix} \boldsymbol{a}_1 & \boldsymbol{a}_2 & \dots & \boldsymbol{a}_{\bar{K}} \end{bmatrix}^T \tag{4.10}$$

$$\boldsymbol{a}_p = \begin{bmatrix} a_p^1 & a_p^2 & \dots & a_p^H \end{bmatrix}^T \tag{4.11}$$

where S_{Re} and S_{Im} represent the real and the imaginary parts of S, respectively. $\boldsymbol{r}_{Re}$ and $\boldsymbol{r}_{Im}$ represent the real and imaginary parts of the monostatic RCS data vector, respectively.

a_p^h represents the spherical harmonic coefficients of the h^{th} spherical harmonic function of the p^{th} scatterer. The sizes of the matrices and vectors are $S_{Re}, S_{Im} \in R^{FM \times H\bar{K}}$,$\boldsymbol{\alpha} \in R^{H\bar{K}}$, and $\boldsymbol{r}_{Re}, \boldsymbol{r}_{Im} \in R^{FM}$, where F and M is the number of signal frequency samples and that of aspect angle samples, respectively.

If the optimal positions are known, meaning $K = \bar{K}$, solving the least squares problem with pseudo inverse gives us the spherical harmonic coefficients for all scatterers. With these coefficients, the reflection gains $\sigma(\boldsymbol{\Psi})$ of all scatterers can be formed and the modeled RCS of the target can be computed from the point scatterer model. Yet, $\bar{K}$ is often greater than K. Therefore, solving the positions of the scatterers is also required. This can be formulated as a sparsity constraint.

4.2.2 Sparsity Constraint

In addition to solving the linear least squares problem, a group sparsity constraint is used to limit the number of scatterers by choosing K optimal scatterer positions among the finite possible scatterer positions. We define all H coefficients of one scatterer as a "group". Our goal is to solve $\boldsymbol{\alpha}$ with K groups consisting of nonzero coefficients while $\bar{K} - K$ groups consisting of zero coefficients. We propose a modified Orthogonal Matching Pursuit (OMP) method to solve this problem.

OMP is a sparse approximation algorithm that solves a system of linear equations with the specified number of nonzero entries in the variable vector [62]. The basic algorithm iteratively and greedily finds the entry in the vector variable which corresponds to the column in the system matrix that is the most correlated with the residual. Instead of finding the column in the system matrix that is the most correlated with the residual, the proposed algorithm finds which vector space of group columns is the most correlated with the residual.

As shown in Algorithm 1, we first initialize the algorithm by setting the residual e as the monostatic RCS data $\overline{\boldsymbol{r}}$. Let $\bar{S}_j$ be the j^{th} group of columns in $\bar{S}$. With singular value

decomposition (SVD), the orthonormal basis of $\bar{S}_j$ can be computed and defined as $\bar{S}_{\text{orth},\,j}$. We can then use the standard inner product of $\bar{S}_{\text{orth},\,j}$ and the residual as the correlation measurement. That is, we find the vector space:

$$\boldsymbol{\lambda} = \arg\max_{\bar{S}_j} \|\widehat{\boldsymbol{e}}_j\|_2 = \arg\max_{\bar{S}_j} \left\|\left\langle \bar{S}_{\text{orth},j}, \boldsymbol{e}\right\rangle\right\|_2 \tag{4.12}$$

where $\widehat{\boldsymbol{e}}_j$ is the residual projected on the vector space of $\bar{S}_j$. We then define the group of columns as $\boldsymbol{\lambda}$ and collect them into the set $\boldsymbol{\Lambda}$. The columns in $\boldsymbol{\Lambda}$ are used to solve for the corresponding entries in $\boldsymbol{\alpha}$. Then we update the residual and repeat by finding the next vector space that is the most correlated with the residual.

With $\boldsymbol{\alpha}$ solved, the reflection gains $\sigma(\boldsymbol{\Psi})$ of K scatterers can be formed. The modeled monostatic RCS of the target can be computed from the point scatterer model as well. This approach provides a point scatterer model that represents the monostatic RCS data.

Algorithm 1: Modified OMP

Result: $\boldsymbol{\alpha}_n$
Initialization: $\boldsymbol{e_1} = \overline{\boldsymbol{r}}, \boldsymbol{\Lambda_0} = \emptyset$;
Compute $\bar{S}_{\text{orth},j}$ for all j with SVD;
for $n = 1 \rightarrow K$ **do**
  $\boldsymbol{\lambda}_n = \arg\max_{\bar{S}_j} \left\|\left\langle \bar{S}_{orth,j}, \boldsymbol{e_n}\right\rangle\right\|_2$
  $\boldsymbol{\Lambda_n} = \boldsymbol{\Lambda_{n-1}} \cup \{\boldsymbol{\lambda_n}\}$
  $\boldsymbol{\alpha_n}\left(i \in \boldsymbol{\Lambda_n}\right) = \arg\min_{\boldsymbol{\alpha}} \left\|S_{\boldsymbol{\Lambda_n}}\boldsymbol{\alpha} - \overline{\boldsymbol{r}}\right\|_2, \boldsymbol{\alpha_n}\left(i \notin \boldsymbol{\Lambda_n}\right) = 0$
  $\boldsymbol{e_{n+1}} = \boldsymbol{r} - \bar{S}_{\boldsymbol{\Lambda_n}}\boldsymbol{\alpha_n}$
end

4.3 Constructing the Scatterer Model for Bistatic RCS Data

In this section, we further construct the point scatterer model that can represent the full bistatic RCS data. We assume that the scatterer positions are the same as the positions solved from the monostatic RCS data. This leaves us with the problem of solving the separable spherical functions of the incident and scatter angles for each scatterer, namely $\sigma_{inc}\left(\boldsymbol{\Psi}_{inc}\right)$ and $\sigma_{sca}\left(\boldsymbol{\Psi}_{sca}\right)$. By assuming that these functions are linear combinations of

spherical harmonics, the problem becomes solving $2HK$ spherical harmonic coefficients. This can be formulated as a bilinear least squares problem.

4.3.1 Least Squares Bilinear Problem

The problem of solving the spherical harmonic coefficients can be formulated as a bilinear problem as shown in Equation 4.13, which proceeds to the least squares optimization problem with the cost, $J(\boldsymbol{\alpha}, \boldsymbol{\beta})$, as shown in Equation 4.14.

$$\boldsymbol{\alpha}^T \bar{Q}_m \boldsymbol{\beta} = \overline{\boldsymbol{r}}_m \tag{4.13}$$

$$\min_{\boldsymbol{\alpha},\boldsymbol{\beta}} J(\boldsymbol{\alpha}, \boldsymbol{\beta}) = \min_{\boldsymbol{\alpha},\boldsymbol{\beta}} \frac{1}{2FM} \sum_{m=1}^{2FM} \left(\overline{\boldsymbol{r}}_m - \boldsymbol{\alpha}^T \bar{Q}_m \boldsymbol{\beta} \right)^2 \tag{4.14}$$

where $\boldsymbol{\alpha}$ is the vector consisting of HK coefficients which form $\sigma_{inc}\left(\boldsymbol{\Psi}_{inc}\right)$, and $\boldsymbol{\beta}$ is the vector consisting of HK coefficients which form $\sigma_{sca}\left(\boldsymbol{\Psi}_{sca}\right)$. $\overline{\boldsymbol{r}}$ is a vector of the RCS data at the sampled frequency and aspect angle, where its real and imaginary parts are stacked vertically. $\bar{Q}$ is the real and imaginary parts of the 3D matrix Q stacked in the third dimension. $\bar{Q}_m$ is the m^{th} 2D slice of the first two dimension of $\bar{Q}$. Each $\bar{Q}_m$ is a block diagonal matrix with block size $H \times H$. Again, F and M are the number of signal frequency samples and that of aspect angle samples, respectively. The sizes of the matrices and vectors are $\boldsymbol{\alpha} \in R^{HK}$, $\boldsymbol{\beta} \in R^{HK}$, $\bar{Q} \in R^{HK \times HK \times 2FM}$, and $\overline{\boldsymbol{r}} \in R^{2FM}$ as shown in Figure 4.2. To better explain the matrices and vectors above, we give an example of $\boldsymbol{\alpha}, \boldsymbol{\beta}$, and Q_m when $H = 2$ and $K = 2$:

$$\boldsymbol{\alpha} = \begin{bmatrix} a_1^1 & a_1^2 & a_2^1 & a_2^2 \end{bmatrix}^T \tag{4.15}$$

$$\boldsymbol{\beta} = \begin{bmatrix} b_1^1 & b_1^2 & b_2^1 & b_2^2 \end{bmatrix}^T \tag{4.16}$$

$$Q_m = Q\left(f_m, \mathbf{\Psi}_{inc,m}, \mathbf{\Psi}_{sca,m}\right) = \begin{bmatrix} q_{11} & q_{12} & 0 & 0 \\ q_{21} & q_{22} & 0 & 0 \\ 0 & 0 & q_{33} & q_{34} \\ 0 & 0 & q_{43} & q_{44} \end{bmatrix} \tag{4.17}$$

$$q_{11} = e^{-i2\pi f_m \tau(\boldsymbol{x}_1, \mathbf{\Psi}_{inc,m}, \mathbf{\Psi}_{sca,m})} Y_1\left(\mathbf{\Psi}_{inc,m}\right) Y_1\left(\mathbf{\Psi}_{sca,m}\right) \tag{4.18}$$

$$q_{21} = e^{-i2\pi f_m \tau(\boldsymbol{x}_1, \mathbf{\Psi}_{inc,m}, \mathbf{\Psi}_{sca,m})} Y_2\left(\mathbf{\Psi}_{inc,m}\right) Y_1\left(\mathbf{\Psi}_{sca,m}\right) \tag{4.19}$$

$$q_{12} = e^{-i2\pi f_m \tau(\boldsymbol{x}_1, \mathbf{\Psi}_{inc,m}, \mathbf{\Psi}_{sca,m})} Y_1\left(\mathbf{\Psi}_{inc,m}\right) Y_2\left(\mathbf{\Psi}_{sca,m}\right) \tag{4.20}$$

$$q_{22} = e^{-i2\pi f_m \tau(\boldsymbol{x}_1, \mathbf{\Psi}_{inc,m}, \mathbf{\Psi}_{sca,m})} Y_2\left(\mathbf{\Psi}_{inc,m}\right) Y_2\left(\mathbf{\Psi}_{sca,m}\right) \tag{4.21}$$

$$q_{33} = e^{-i2\pi f_m \tau(\boldsymbol{x}_2, \mathbf{\Psi}_{inc,m}, \mathbf{\Psi}_{sca,m})} Y_1\left(\mathbf{\Psi}_{inc,m}\right) Y_1\left(\mathbf{\Psi}_{sca,m}\right) \tag{4.22}$$

$$q_{43} = e^{-i2\pi f_m \tau(\boldsymbol{x}_2, \mathbf{\Psi}_{inc,m}, \mathbf{\Psi}_{sca,m})} Y_2\left(\mathbf{\Psi}_{inc,m}\right) Y_1\left(\mathbf{\Psi}_{sca,m}\right) \tag{4.23}$$

$$q_{34} = e^{-i2\pi f_m \tau(\boldsymbol{x}_2, \boldsymbol{\Psi}_{inc,m}, \boldsymbol{\Psi}_{sca,m})} Y_1\left(\boldsymbol{\Psi}_{inc,m}\right) Y_2\left(\boldsymbol{\Psi}_{sca,m}\right) \tag{4.24}$$

$$q_{44} = e^{-i2\pi f_m \tau(\boldsymbol{x}_2, \boldsymbol{\Psi}_{inc,m}, \boldsymbol{\Psi}_{sca,m})} Y_2\left(\boldsymbol{\Psi}_{inc,m}\right) Y_2\left(\boldsymbol{\Psi}_{sca,m}\right) \tag{4.25}$$

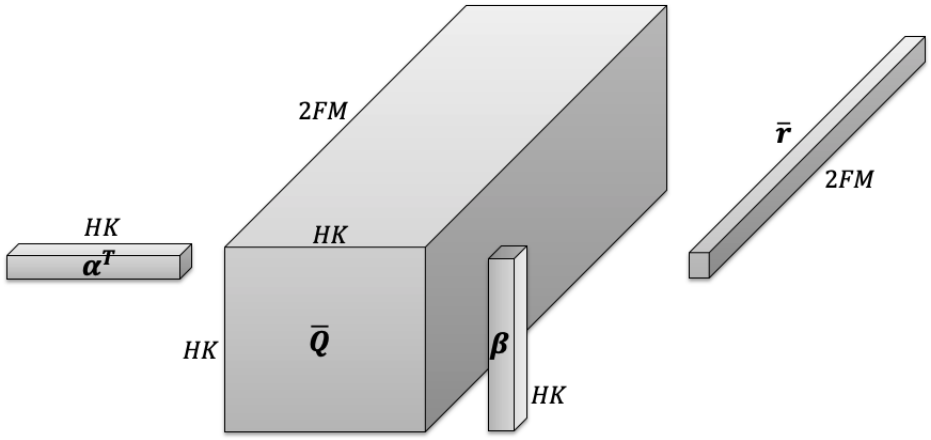

Figure 4.2: Vectors and matrices dimension illustration

4.3.2 Normalized Iterative Algorithm

There are several methods for solving the bilinear least squares problem Equation 4.14 [63]. One commonly used approach is the normalized iterative algorithm. The costs in Equation 4.14 with variables $[\boldsymbol{\alpha}, \boldsymbol{\beta}]$ and $[z\boldsymbol{\alpha}, \frac{1}{z}\boldsymbol{\beta}]$ are equal for constant scalar z. We can restrict the variable vectors by assuming $\|\boldsymbol{\alpha}\| = 1$ and the first non-zero entry of $\boldsymbol{\alpha}$ is positive. The normalized iterative algorithm solves $\boldsymbol{\alpha}$ and $\boldsymbol{\beta}$ in a back-and-forward manner. When either $\boldsymbol{\alpha}$ or $\boldsymbol{\beta}$ is fixed, solving another becomes a linear inversion problem and can be easily solved with the pseudo inverse. This algorithm is shown as Algorithm 2.

With solved $\boldsymbol{\alpha}$ and $\boldsymbol{\beta}$, the reflection gains $\sigma_{inc}\left(\boldsymbol{\Psi}_{inc}\right)$ and $\sigma_{sca}\left(\boldsymbol{\Psi}_{sca}\right)$ of all scatterers can be formed. The modeled bistatic RCS of the target can be computed from the point

scatterer model as well.

Algorithm 2: Normalized Iterative Algorithm

Result: $\boldsymbol{\alpha}_n, \boldsymbol{\beta}_n$
Initialization:$\boldsymbol{\alpha}_0 = \mathbb{1}/\sqrt{HK}$
for $n = 1 \rightarrow MaxIteration$ **do**
  $\overline{\boldsymbol{\beta}_n} = \arg\min_{\boldsymbol{\beta} \in R^{HK}} J\left(\boldsymbol{\alpha}_{n-1}, \boldsymbol{\beta}\right)$
  $\overline{\boldsymbol{\alpha}_n} = \arg\min_{\boldsymbol{\alpha} \in R^{HK}} J\left(\boldsymbol{\alpha}, \overline{\boldsymbol{\beta}_n}\right)$
  Let $\xi_n = \pm 1$ be the sign of the first non-zero entry of $\overline{\boldsymbol{\alpha}_n}$
  $\boldsymbol{\alpha}_n = \xi_n \overline{\boldsymbol{\alpha}_n} / \left\|\overline{\boldsymbol{\alpha}_n}\right\|$
  $\boldsymbol{\beta}_n = \xi_n \overline{\boldsymbol{\beta}_n} \| \overline{\boldsymbol{\alpha}_n} \mid$
end

4.4 Monostatic and Bistatic Point Scatterer Model Simulation Results

Same as in the previous simulation results section, we demonstrate the feasibility of the proposed approach using the RCS data of a 60-meter-long aircraft made up of PEC. The aircraft geometry STL file is obtained from [56] and is shown in Figure 4.3. The RCS data is generated from the EM simulator, CST Studio Suite, with horizontal polarization.

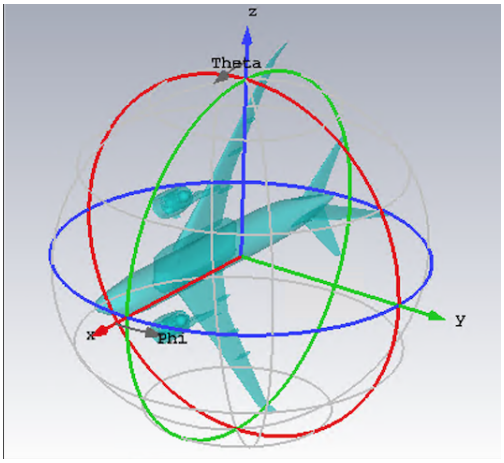

Figure 4.3: Aircraft Geometry

We sample one frequency at 1GHz i.e. $F = 1$. The angle sampling increment is 20 degrees for θ_{inc}, ϕ_{inc}, θ_{sca}, and ϕ_{sca} which means $M = 9 \times 18 \times 9 \times 18 = 26244$. Our goal is to find 16 scatterers (i.e. $K = 16$) where all scatterers are located in a 10m×10m×10m

grid in the local coordinate (i.e. $\bar{K} = 1000$). Since we use spherical harmonics of degree 12, $H = (1 + 12)^2 = 169$.

Using the computation mentioned earlier, the monostatic point scatterer model is constructed and shown in Figure 4.4. Each scatterer has a position coordinate and an angular-dependent spherical harmonic based reflection gain. The brightness indicates the value of the real numbered reflection gain at the corresponding aspect angle. The comparison of the dB scaled RCS power between the true data from CST, the spherical harmonic model, and the ellipsoid model [59] is provided in Figure 4.5.

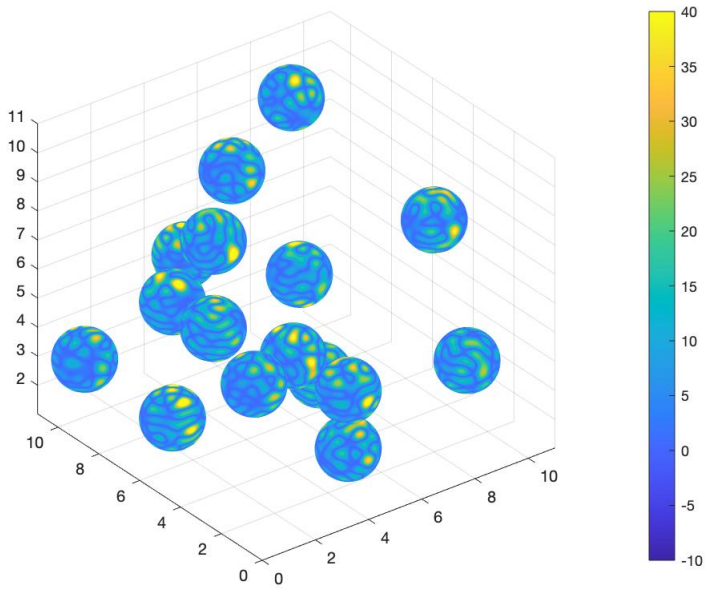

Figure 4.4: Reflection gains $\sigma(\mathbf{\Psi})$ and positions of the monostatic point scatterer model

We take the scatterer positions and proceed to the bistatic point scatterer model computation. Note that matrix $\bar{Q} \in R^{2704\times2704\times52488}$ is extremely large and hard to compute. We leverage its low-rank property to resolve this issue. Figure 4.6 shows the constructed bistatic point scatterer model. Each scatterer has a position coordinate and two angular-dependent spherical harmonic based functions. The reflection gain is determined by the multiplication of two functions evaluated at the incident and scatter angle, respectively, as mentioned in Equation 4.1.

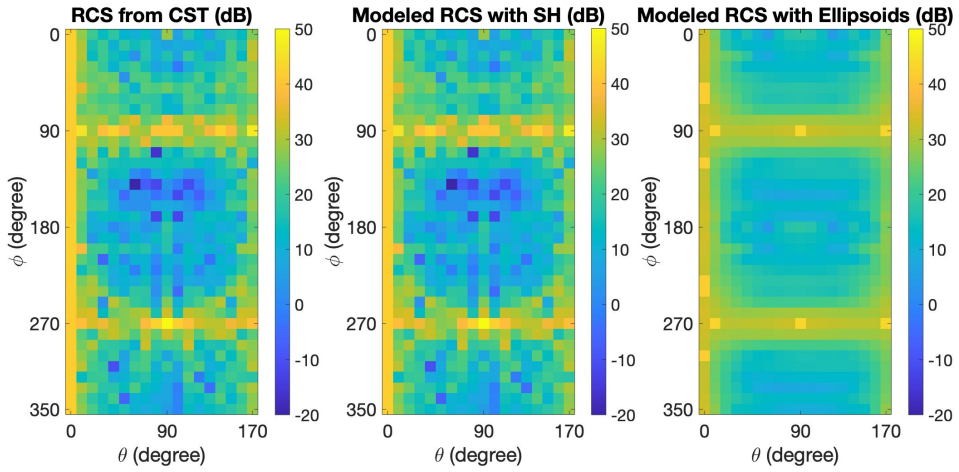

Figure 4.5: Comparison of the dB scaled RCS power between the true data from CST, the spherical harmonic model, and the ellipsoid model

Figure 4.7 shows the simulated bistatic RCS data from CST and the modeled bistatic RCS of the point scatterer model at $\theta_{inc} = 80^o$ and $\phi_{inc} = 260^o$. Figure 4.8 shows that at $\theta_{inc} = 100^o$ and $\phi_{inc} = 280^o$. As shown in Figure 4.7 and Figure 4.8, the real and imaginary parts of the bistatic RCS data are effectively represented by the point scatterer model, especially at the highly reflected areas. Particularly, in Figure 4.8, the simulated RCS and the modeled RCS at $\phi_{sca} = 270^o$ show the same pattern of dark and light distribution. Figure 4.9 shows the minimized error defined in Equation 4.14 between the modeled RCS and the simulated RCS from CST using different spherical harmonic degrees (L) and numbers of scatterers. As the number of spherical harmonics increases, the minimized cost decreases. This figure also includes the minimized cost of the same simulation but with 24 scatterers (i.e. $K = 24$). The minimized costs are lower when more scatterers are used. The root mean square errors (RMSE) can be obtained by taking the square root of the costs. The lowest RMSE computed with 16 and 24 scatterers are 11.7 and 10.9, respectively. This shows that the RMSE is reduced by 7% by increasing K from 16 to 24. The MATLAB code of this example is publicly available at https://github.com/howeri/SH_BiAnisoPSM.

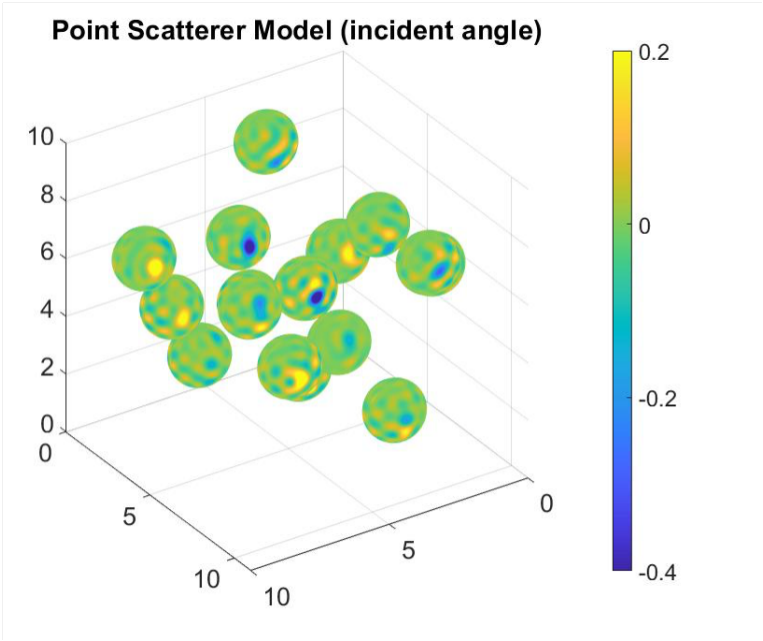

(a) $\sigma_{inc}(\mathbf{\Psi}_{inc})$

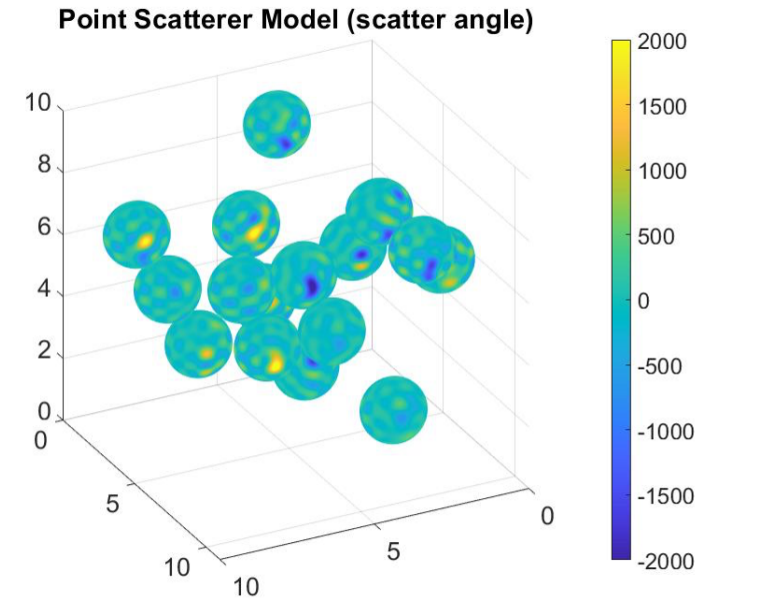

(b) $\sigma_{sca}(\mathbf{\Psi}_{sca})$

Figure 4.6: Reflection gains and positions of the bistatic point scatterer model

To conclude the spherical harmonic based anisotropic point scatterer modeling, the proposed spherical harmonic based anisotropic point scatterer model describes the bistatic RCS data of a radar target with a finite number of scatterer positions and spherical harmonic coefficients. With this model, the RCS can be reconstructed at a given aspect angle in less than 1 millisecond while it takes 5 seconds to compute the RCS using CST. Thus, HPC EM emulators can efficiently simulate the real-time EM wave interactions between multiple radar targets. The more RCS data used in the optimization, the higher fidelity of the model is. There exists a limitation to the number of data. That is, as FM increases to a certain level, the storage size of $\bar{Q}$ will become too large and limit the computations in Algorithm 2. More detailed information can be found in our journal paper [64].

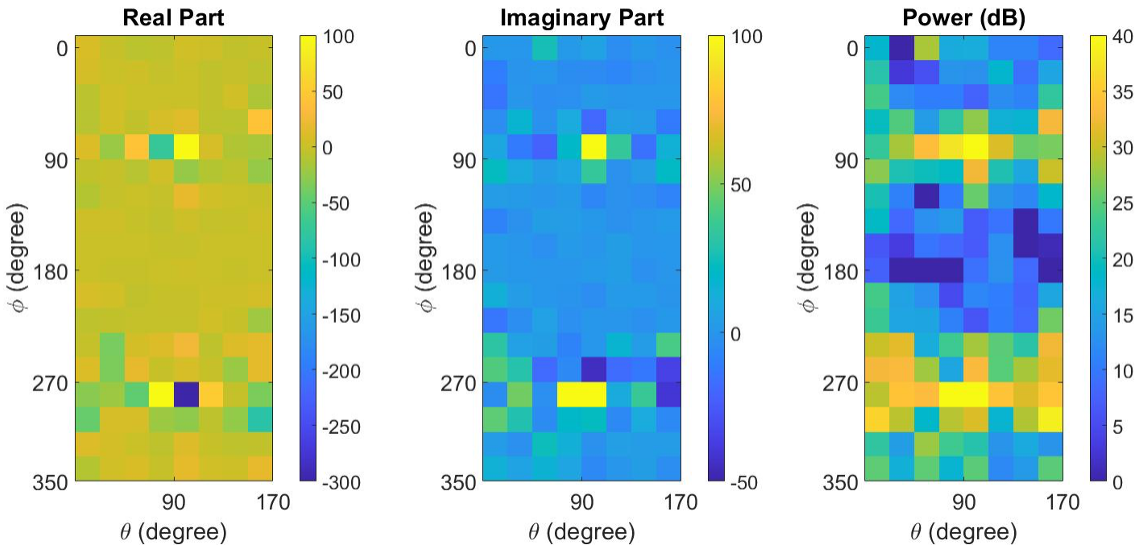

(a) Simulated bistatic RCS from CST

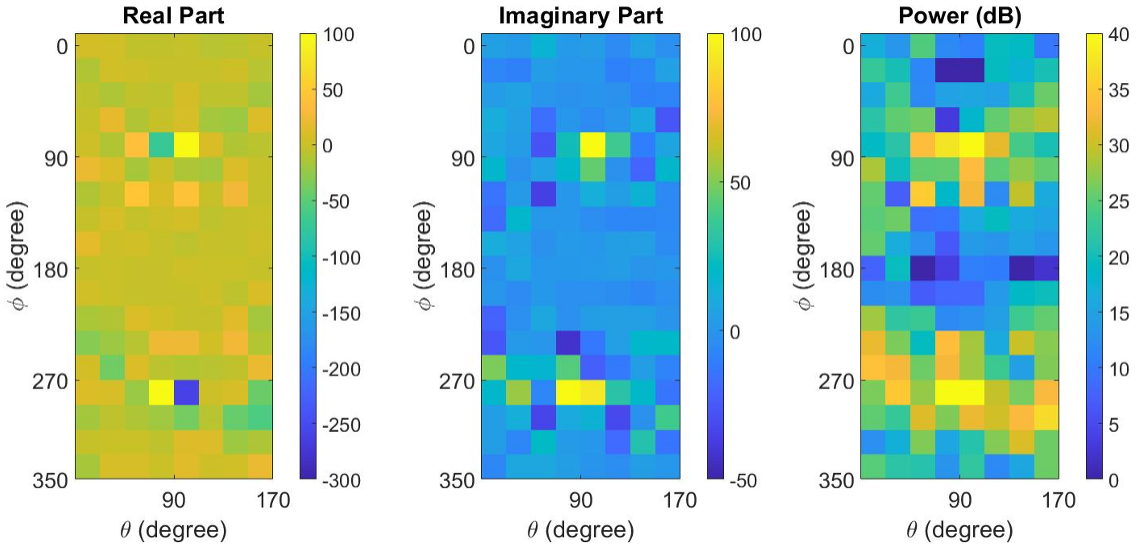

(b) Modeled bistatic RCS of the point scatterer model

Figure 4.7: RCS at $\theta_{inc} = 80^o$ and $\phi_{inc} = 260^o$

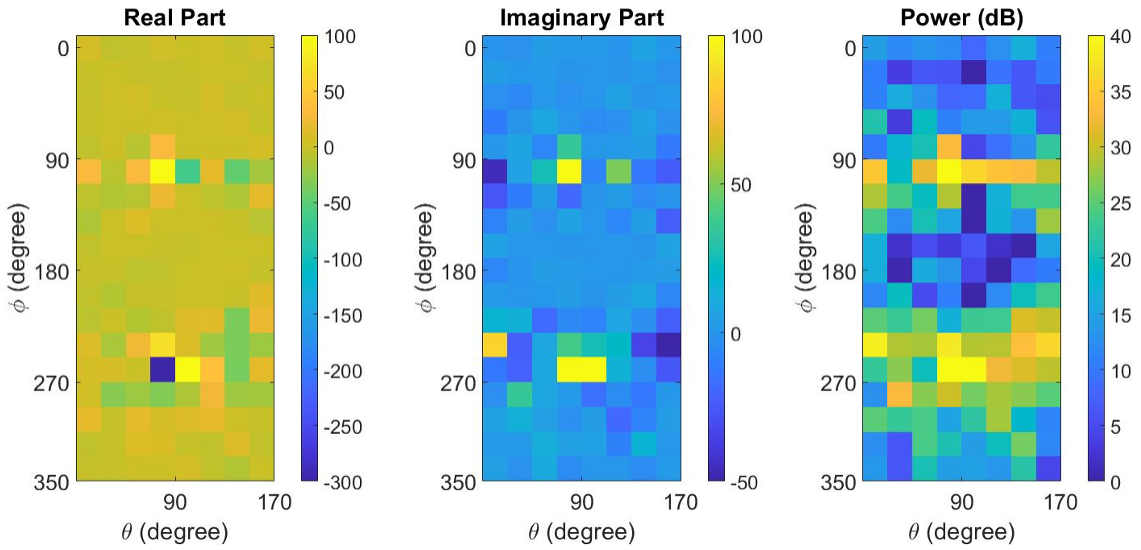

(a) Simulated bistatic RCS from CST

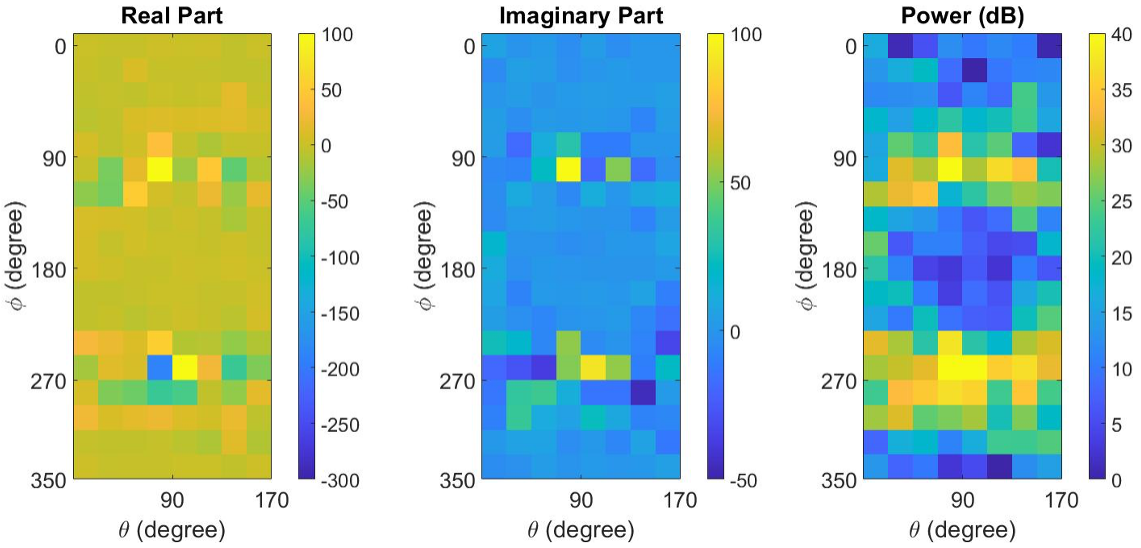

(b) Modeled bistatic RCS of the point scatterer model

Figure 4.8: RCS at $\theta_{inc} = 100^o$ and $\phi_{inc} = 280^o$

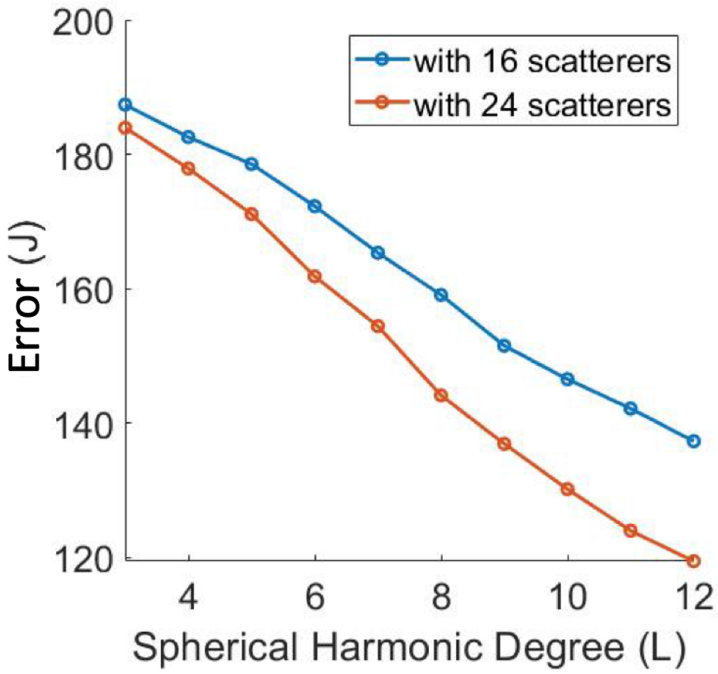

Figure 4.9: Error between the modeled RCS and the simulated RCS from CST using different spherical harmonic degrees (L) and numbers of scatterers

4.5 Efficient Spherical Harmonic based Anisotropic Point Scatterer Model

The assumption of knowing a finite number of possible scatterer positions restricts the solutions of the scatterer positions from the continuous space. By assuming that all scatterers are located in a 10m×10m×10m grid in the local coordinate system, we can only compute the scatterer positions as integer components between 0 and 10.

In this section, we illustrate an efficient method that finds the monostatic point scatterer model of continuous scatterer positions. The algorithm constructing this model with large-scale RCS data is discussed. The scatterer position and the reflection profile of each scatterer are solved using particle swarm optimization (PSO) and least squares methods. In addition, the function evaluations in PSO are accelerated by taking advantage of the matrix structure, making the algorithm 22 times faster compared to the naive approach. The results show that the point scatterer model can effectively represent the RCS data of a radar target. Same as mentioned in the previous section, the position obtained with this algorithm can be used to further compute the spherical harmonic based bistatic point scatterer model using the full bistatic RCS data. By defining real numbered and frequency-independent reflection gains, the channel between the EM waves before and after the modulation can be implemented as a finite impulse response (FIR) filter.

4.5.1 Greedy Scatterer Position Search

We propose to greedily search for one optimal scatterer position at a time.

Define

$$\overline{\boldsymbol{r}} = \begin{bmatrix} \boldsymbol{r}_{Re} \\ \boldsymbol{r}_{Im} \end{bmatrix} \tag{4.26}$$

$$\bar{\boldsymbol{S}}(\boldsymbol{p}) = \begin{bmatrix} \boldsymbol{S}_{Re}(\boldsymbol{p}) \\ \boldsymbol{S}_{Im}(\boldsymbol{p}) \end{bmatrix} \tag{4.27}$$

$$\boldsymbol{S}(\boldsymbol{p}) = \begin{bmatrix} \boldsymbol{w}_1(\boldsymbol{p}) \\ \boldsymbol{w}_2(\boldsymbol{p}) \\ \vdots \\ \boldsymbol{w}_N(\boldsymbol{p}) \end{bmatrix} \otimes \begin{bmatrix} \boldsymbol{H} \\ \boldsymbol{H} \\ \vdots \\ \boldsymbol{H} \end{bmatrix} \tag{4.28}$$

$$\boldsymbol{w}_n = \begin{bmatrix} e^{i2\pi f_n(2\langle \boldsymbol{p}, \boldsymbol{d}_1 \rangle / c)} \\ e^{i2\pi f_n(2\langle \boldsymbol{p}, \boldsymbol{d}_2 \rangle / c)} \\ \vdots \\ e^{i2\pi f_n(2\langle \boldsymbol{p}, \boldsymbol{d}_M \rangle / c)} \end{bmatrix} \tag{4.29}$$

$$\boldsymbol{H} = \begin{bmatrix} \boldsymbol{h}_1 & \boldsymbol{h}_2 & \cdots & \boldsymbol{h}_L \end{bmatrix} \tag{4.30}$$

, where $\boldsymbol{r}_{Re} \in \mathbb{R}^{MN}$ and $\boldsymbol{r}_{Im} \in \mathbb{R}^{MN}$ represents the real and imaginary part of the monostatic RCS data vector, respectively. N and M are the number of the signal frequency samples and that of the aspect angle samples, respectively. $\boldsymbol{S}_{Re} \in \mathbb{R}^{MN \times L}$ and $\boldsymbol{S}_{Im} \in \mathbb{R}^{MN \times L}$ represents the real and the imaginary part of $\boldsymbol{S}$, respectively. $\boldsymbol{p}$ represents the scatterer position. The operator $\otimes$ represents element-wise multiplication. $\boldsymbol{h}_l \in \mathbb{R}^M$ represents the l^{th} spherical harmonic function at all M aspect angels shaped vertically. The size of $\boldsymbol{H}$ is $\mathbb{R}^{M \times L}$.

As shown in the Algorithm 3, we first initialize the algorithm by setting the residual $\boldsymbol{e}$ as $\overline{\boldsymbol{r}}$, which is the real part and the imaginary parts of the monostatic RCS data stacked vertically. $\bar{\boldsymbol{S}}_{all} = [\,]$ is initialized as an empty array. The optimization problem $\min_{\boldsymbol{\alpha}_k} \left\| \bar{\boldsymbol{S}}(\boldsymbol{p})\boldsymbol{\alpha}_k - \boldsymbol{e} \right\|_2$ solves the spherical harmonic coefficients given a scatterer position. The $\arg\min_{\boldsymbol{p}}$ operator solves the scatterer position, $\boldsymbol{p}_k^*$, such that $\bar{\boldsymbol{S}}(\boldsymbol{p})\boldsymbol{\alpha}_k$ is as close

Algorithm 3: Greedy Scatterer Position Search

Result: $\boldsymbol{p}^*_{1:K}, \boldsymbol{\alpha}^*$
Initialization: $\boldsymbol{e} = \overline{\boldsymbol{r}},\ \bar{\boldsymbol{S}}_{all} = [\,]$;
for $k = 1 \rightarrow K$ **do**
  $\boldsymbol{p}^*_k = \arg\min_{\boldsymbol{p}} \min_{\boldsymbol{\alpha}_k} \left\| \bar{\boldsymbol{S}}(\boldsymbol{p})\boldsymbol{\alpha}_k - \boldsymbol{e} \right\|_2$
  $\bar{\boldsymbol{S}}_{all} = \left[\bar{\boldsymbol{S}}_{all}\ \bar{\boldsymbol{S}}(\boldsymbol{p}^*_k) \right]$
  $\boldsymbol{\alpha}^* = \arg\min_{\boldsymbol{\alpha}} \left\| \bar{\boldsymbol{S}}_{all}\boldsymbol{\alpha} - \overline{\boldsymbol{r}} \right\|_2$
  $\boldsymbol{e} = \overline{\boldsymbol{r}} - \bar{\boldsymbol{S}}_{all}\boldsymbol{\alpha}^*$
end

to the residual as possible. The matrix $\bar{\boldsymbol{S}}(\boldsymbol{p}^*_k)$ is then stacked horizontally with $\bar{\boldsymbol{S}}_{all}$ so that the information of the solved scatterer positions is stored. Next, $\bar{\boldsymbol{S}}_{all}$ is used to compute the spherical harmonic coefficients of all 1 to k scatterers obtained so far. That is, $\boldsymbol{\alpha}^* = [c_{1,1}, c_{2,1}, ..., c_{L,k}]$ The residual $\boldsymbol{e}$ is updated to indicate the difference between the modeled RCS and the RCS data. The cost function for Algorithm 3 is the norm of this residual, that is, $\left\| \overline{\boldsymbol{r}} - \bar{\boldsymbol{S}}_{all}\boldsymbol{\alpha}^* \right\|$. The above-mentioned steps are iterated K times where each time one of the scatterer positions is solved. Since the proposed algorithm contains a greedy search, a residual stopping criterion can be defined in advance. Once the search stops, the output of the algorithm indicates the least number of scatterers needed for the point scatterer model to best represent the RCS data.

4.5.2 Particle Swarm Position Search

In every iteration of the Greedy Scatterer Position Search (Algorithm 3), there are two optimization problems to be solved:

1. $\boldsymbol{p}^* = \arg\min_{\boldsymbol{p}} \min_{\boldsymbol{\alpha}_n} \left\| \bar{\boldsymbol{S}}(\boldsymbol{p})\boldsymbol{\alpha}_{\boldsymbol{n}} - \boldsymbol{e} \right\|_2$
2. $\boldsymbol{\alpha}^* = \arg\min_{\boldsymbol{\alpha}} \left\| \bar{\boldsymbol{S}}_{all}\boldsymbol{\alpha} - \boldsymbol{e} \right\|_2$

The second problem can be solved efficiently using the least squares method, QR factorization, due to its linearity. Yet, the first problem of solving the scatterer position is highly nonlinear. Note that the dimension of the control variable in this problem is three, i.e. the x, y, and z coordinates of the scatterer position. We propose to use PSO to solve this problem.

PSO is a bio-inspired iterative heuristic algorithm used to globally optimize a cost function. The algorithm is not dependent on the gradient nor other differential forms of the cost function and is suitable for solving continuous nonlinear functions. The application of the PSO algorithm is shown in Figure 4.10. The algorithm hyperparameters, c_1, c_2, c_3, and the number of particles, are initialized. The position and the velocity of the j^{th} particle are denoted $\boldsymbol{p}_j$ and $\boldsymbol{v}_j$. The positions and the velocities of all particles are also initialized. The cost function $\min_{\boldsymbol{\alpha}_n} \left\| \bar{\boldsymbol{S}}(\boldsymbol{p}_j)\boldsymbol{\alpha_n} - \boldsymbol{e} \right\|_2$ is then evaluated at all particle positions. The position of each particle's best record, denoted $\tilde{\boldsymbol{p}}_{local,j}$, is updated. The position of the best record among all particles, denoted $\tilde{\boldsymbol{p}}_{global}$, is updated as well in order to keep track of the potential optimal positions. $\boldsymbol{p}_j$ and $\boldsymbol{v}_j$ are updated with:

$$\boldsymbol{p}_j\left(t+1\right) = \boldsymbol{p}_j\left(t\right) + \boldsymbol{v}_j\left(t\right) \tag{4.31}$$

$$\boldsymbol{v}_j(t+1) = c_1\boldsymbol{v}_j(t) + c_2\left(\tilde{\boldsymbol{p}}_{local,j} - \boldsymbol{p}_j(t)\right) + c_3\left(\tilde{\boldsymbol{p}}_{global} - \boldsymbol{p}_j(t)\right) \tag{4.32}$$

The iteration ends when all particle positions converge or a stopping condition is satisfied.

4.5.3 Efficient Function Evaluation

When evaluating a scatterer position, $\boldsymbol{p}$ is fixed, and therefore QR factorization can be applied to evaluate the cost function $\min_{\boldsymbol{\alpha}_n} \left\| \bar{\boldsymbol{S}}\boldsymbol{\alpha_n} - \boldsymbol{e} \right\|_2$. Yet, it causes a long computation time due to the large dimension of $\bar{\boldsymbol{S}}$. The accumulated computation time of the PSO becomes unacceptable since PSO is an iterative algorithm and the cost function is evaluated numerous times at different scatterer positions. We propose an efficient function evaluation method taking advantage of the matrix structure and reducing the computation time of the PSO algorithm.

Instead of applying QR factorization, the problem $\min_{\boldsymbol{\alpha}_n} \left\| \bar{\boldsymbol{S}}\boldsymbol{\alpha_n} - \boldsymbol{e} \right\|_2$ can be solved with pseudoinverse. At first glance, it may seem that the computation time is longer com-

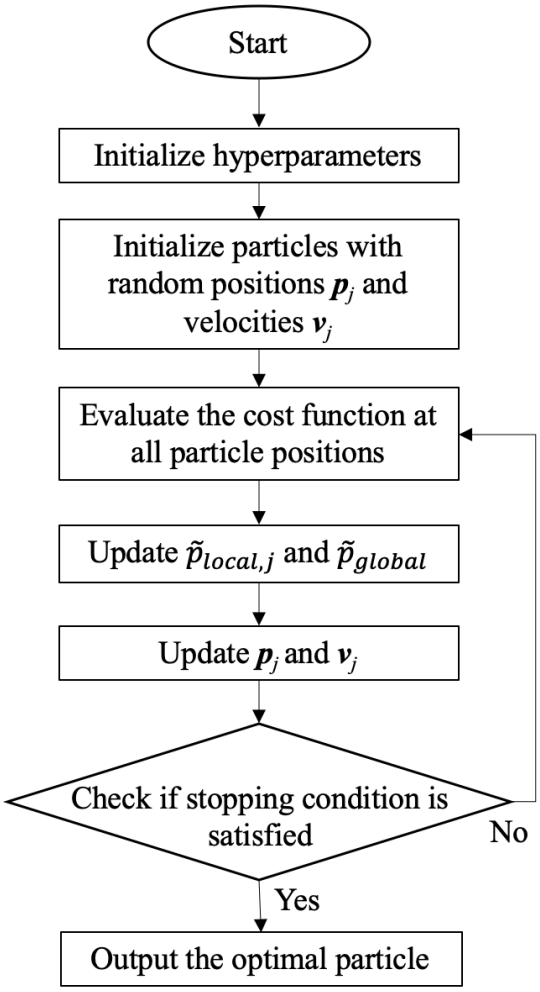

Figure 4.10: Particle swarm optimization application

pared to that when applying QR decomposition since pseudoinverse involves matrix inversion. Yet, by taking advantage of the matrix structure of Equation 4.28, the pseudoinverse method can be simplified and solves the problem in a more efficient way.

Define

$$\boldsymbol{W}_n = \text{diag}\left(\text{Re}\left(\boldsymbol{w}_n\right)\right) \tag{4.33}$$

$$\boldsymbol{W}_{N+n} = \text{diag}(\text{Im}(\boldsymbol{w}_n)) \tag{4.34}$$

The simplification is shown below:

$$\begin{aligned}
\boldsymbol{\alpha}_n^* &= \left(\bar{\boldsymbol{S}}^T\bar{\boldsymbol{S}}\right)^{-1}\bar{\boldsymbol{S}}^T\boldsymbol{e} \\
&= \left(\begin{bmatrix} \boldsymbol{H}^T\boldsymbol{W}_1 & \dots & \boldsymbol{H}^T\boldsymbol{W}_{2N} \end{bmatrix}\begin{bmatrix} \boldsymbol{W}_1\boldsymbol{H} \\ \vdots \\ \boldsymbol{W}_{2N}\boldsymbol{H} \end{bmatrix}\right)^{-1}\bar{\boldsymbol{S}}^T\boldsymbol{e} \\
&= \left(\sum_{n=1}^{2N}\boldsymbol{H}^T\boldsymbol{W}_n^2\boldsymbol{H}\right)^{-1}\bar{\boldsymbol{S}}^T\boldsymbol{e} \\
&= \left(\boldsymbol{H}^T\left(\sum_{n=1}^{2N}\boldsymbol{W}_n^2\right)\boldsymbol{H}\right)^{-1}\bar{\boldsymbol{S}}^T\boldsymbol{e} \qquad (4.35) \\
&= \left(\boldsymbol{H}^T\left(N\boldsymbol{I}\right)\boldsymbol{H}\right)^{-1}\bar{\boldsymbol{S}}^T\boldsymbol{e} \\
&= N\left(\boldsymbol{H}^T\boldsymbol{H}\right)^{-1}\bar{\boldsymbol{S}}^T\boldsymbol{e} \\
&= N\left(\boldsymbol{H}^T\boldsymbol{H}\right)^{-1}\begin{bmatrix} \boldsymbol{H}^T\boldsymbol{W}_1 & \dots & \boldsymbol{H}^T\boldsymbol{W}_{2N} \end{bmatrix}\boldsymbol{e} \\
&= N\left(\boldsymbol{H}^T\boldsymbol{H}\right)^{-1}\boldsymbol{H}^T\sum_{n=1}^{2N}\boldsymbol{w}_n\otimes\boldsymbol{e}_n
\end{aligned}$$

Note that in the fifth line of Equation 4.35, $\sum_{n=1}^{2N}\boldsymbol{W}_n^2$ is simplified as $N\boldsymbol{I}$ since each diag-

onal entry of the resulting matrix is the summation of the squares of N real and imaginary pairs derived from the exponential terms with the magnitude of one as shown in Equation 4.29. The dimension of the matrix that requires inversion is $\mathbb{R}^{L\times L}$. This inversion only needs to be computed once for the evaluation at any scatterer position since it is independent of the scatterer position. After solving $\boldsymbol{\alpha}_n^*$, the evaluation cost of the scatterer location is computed with $\left\|\bar{\boldsymbol{S}}\boldsymbol{\alpha_n}^* - \boldsymbol{e}\right\|_2$. The computation time of the PSO algorithm is reduced significantly since

1. No extra matrix inversion is required.

2. The high dimensional multiplication, $\bar{\boldsymbol{S}}^T\bar{\boldsymbol{S}}$, is exempted.

Originally, at each function evaluation, the complexity of the floating point operations (flops) is around $O(L^2MN)$. Using the proposed efficient function evaluation, the complexity of flops is reduced to $O(L^2M)$.

4.5.4 Efficient Monostatic Point Scatterer Model Simulation Result

The feasibility of the proposed approach is demonstrated using the monostatic RCS data of a 14-meter-long aircraft made up of PEC. The aircraft geometry STL file is obtained from [65] and is shown in Figure 4.11. The complex numbered RCS data is generated by the EM simulator, CST Studio Suite, with horizontal polarization. The frequency samples are between 100MHz and 150MHz with 1MHz increment, i.e. $N = 51$. The angle samples for $[\theta, \phi]$ range from 30^o to 150^o and 210^o to 330^o, respectively, and the increment is 1 degree. That is, $M = 121 \times 121 = 14641$. This range is chosen to indicate the RCS of the bottom of the aircraft. The total number of the complex numbered RCS data is $N \times M = 746691$. The RCS data image at 100MHz is shown in Figure 4.12.

In this experiment, 16 scatterers (i.e. $K = 16$) are solved in the local coordinate where each scatterer position ranges from -10 to 10 in the x, y, and z coordinates. The reflection gain of each scatterer is constructed with spherical harmonic functions of degree 11, which

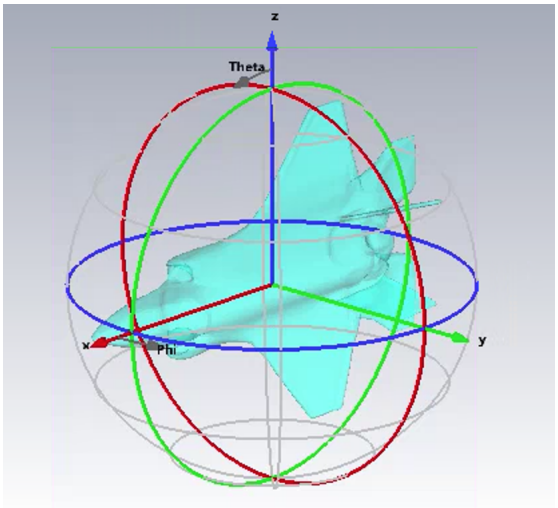

Figure 4.11: Aircraft geometry

means that $L = (1 + 11)^2 = 144$. Figure 4.13 represents the residual between the RCS from CST and the modeled RCS using one scatterer when moving the scatterer position in the x, y, and z coordinates, respectively. The figure shows the nonlinearity of the cost function. When applying the Greedy Scatterer Position Search Algorithm, the computation time of each function evaluation $\min_{\boldsymbol{\alpha}_n} \left\| \bar{\boldsymbol{S}}\boldsymbol{\alpha_n} - \boldsymbol{e} \right\|_2$ is 14.17 seconds using the QR decomposition because of the extremely large size of the matrix $\bar{\boldsymbol{S}} \in \mathbb{R}^{1493382 \times 144}$. The accumulated computation time becomes unacceptable since the cost function is evaluated numerous times (around 36000 times in this example). Using the proposed simplified pseudoinverse, the computation time is reduced to 0.62 second, which is 22 times faster than that of the QR decomposition.

The constructed monostatic point scatterer model is shown in Figure 4.14. Each scatterer has a position coordinate and an angular-dependent spherical harmonic based reflection gain. The brightness indicates the value of the real numbered reflection gain at the corresponding aspect angle. Figure 4.15 shows the modeled RCS image at 100MHz. By comparing Figure 4.12 and Figure 4.15, we observe that the real and imaginary parts of the RCS data across aspect angles are effectively represented by the point scatterer model. The error distribution between the RCS from CST and the modeled RCS at 100MHz is shown

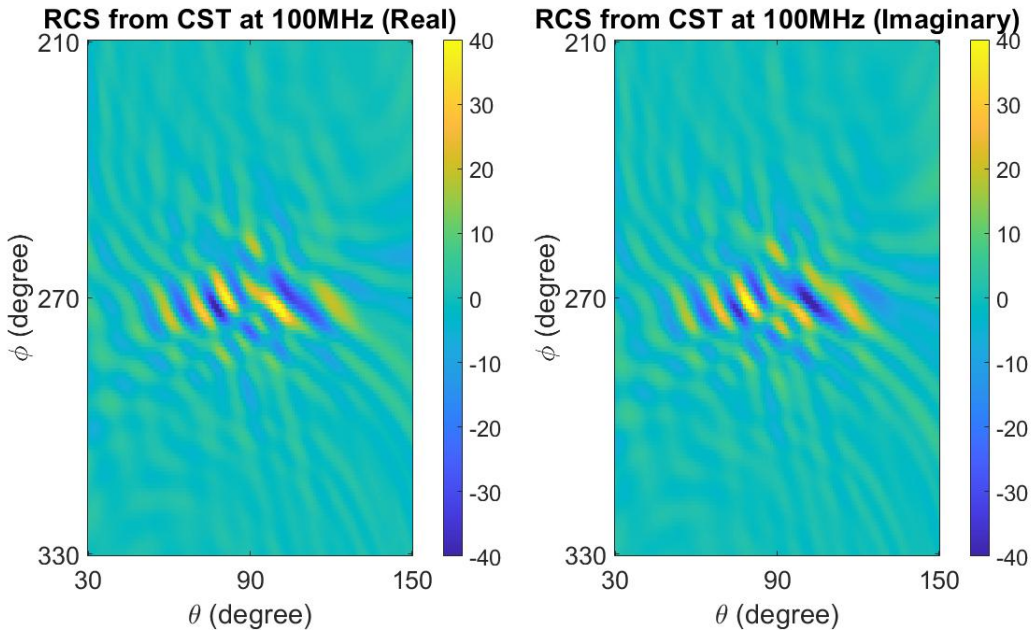

Figure 4.12: RCS data image from CST at 100MHz.

in Figure 4.16, where the error is centered around the highly reflected region. Figure 4.17 shows the comparison between the RCS from CST and the modeled RCS at 100MHz and $\phi = 270$ when varying θ. Figure 4.18 shows the comparison at $[\theta = 30, \phi = 210]$ and $[\theta = 90, \phi = 270]$ when varying the frequency. The RCS data across frequencies is observed to be effectively represented by the point scatterer model as well. The ellipsoid model [59] is compared with the proposed spherical harmonic based point scatterer model as shown in Figure 4.19. The structural similarity index is used to quantify the accuracy of the models [66]. The similarity of the RCS power in the dB scale between the CST data and the ellipsoid model converges to 0.11 in 30 minutes. The similarity between the CST data and the proposed spherical harmonic based point scatterer model continuously increases to 0.38 in 6 hours. The spherical harmonic based model is thus 27% more accurate than the ellipsoid model. The MATLAB code of this example is publicly available at https://github.com/howeri/SH_MonoAnisoPSM_PSO.

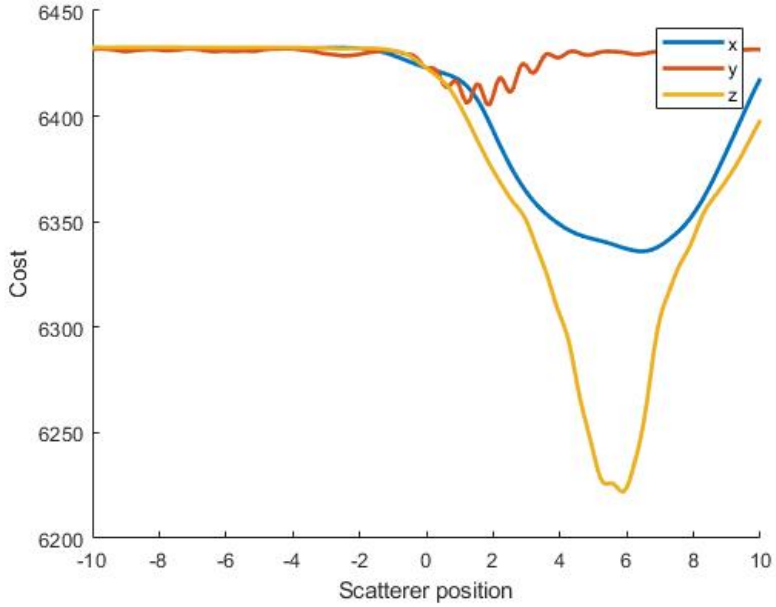

Figure 4.13: Residual while moving the first scatterer position in the x, y, and z coordinate.

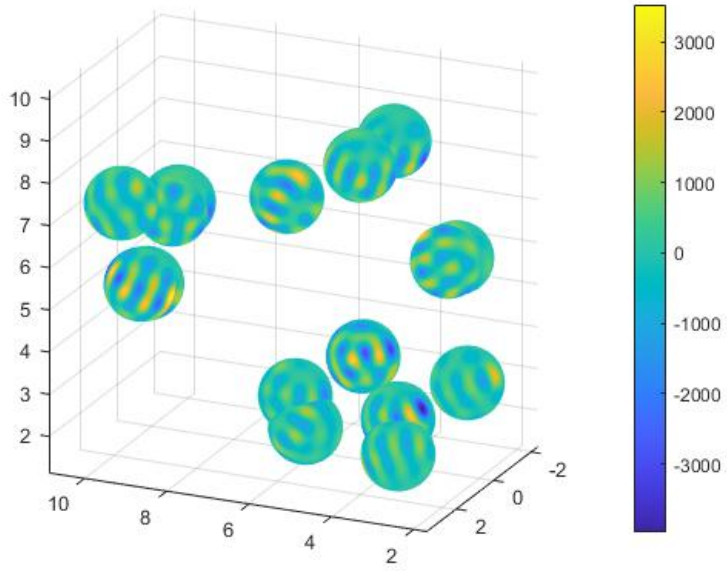

Figure 4.14: Monostatic point scatterer model.

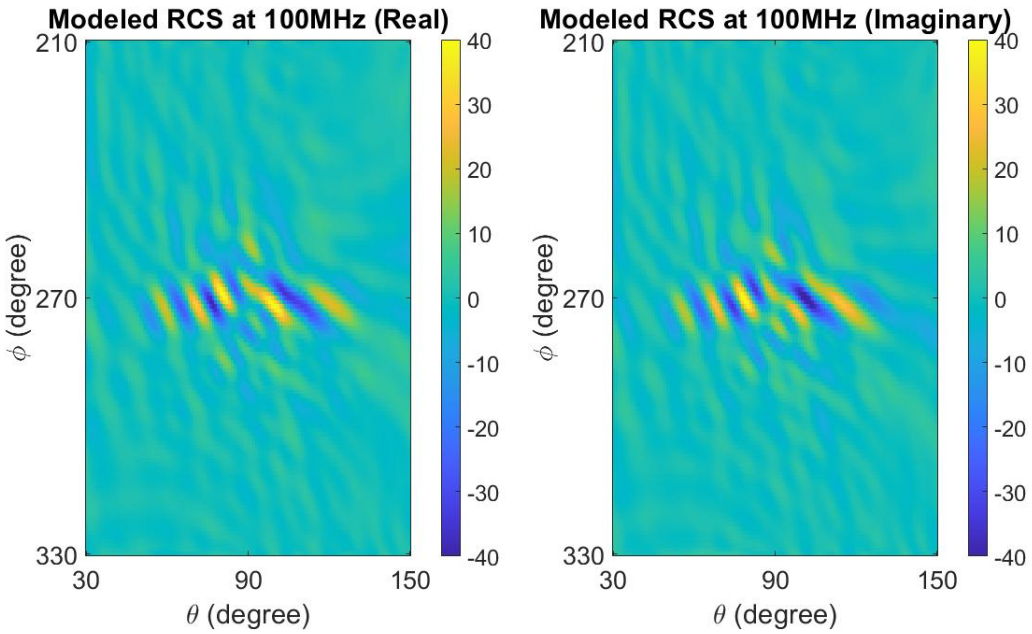

Figure 4.15: Modeled RCS data image at 100MHz.

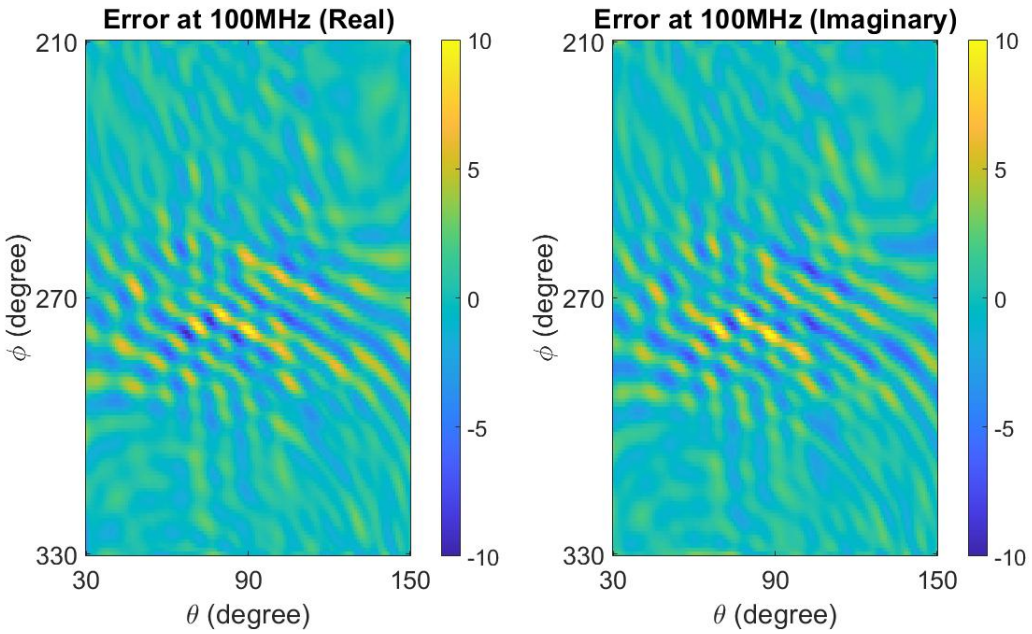

Figure 4.16: Error between the RCS from CST and the modeled RCS at 100MHz.

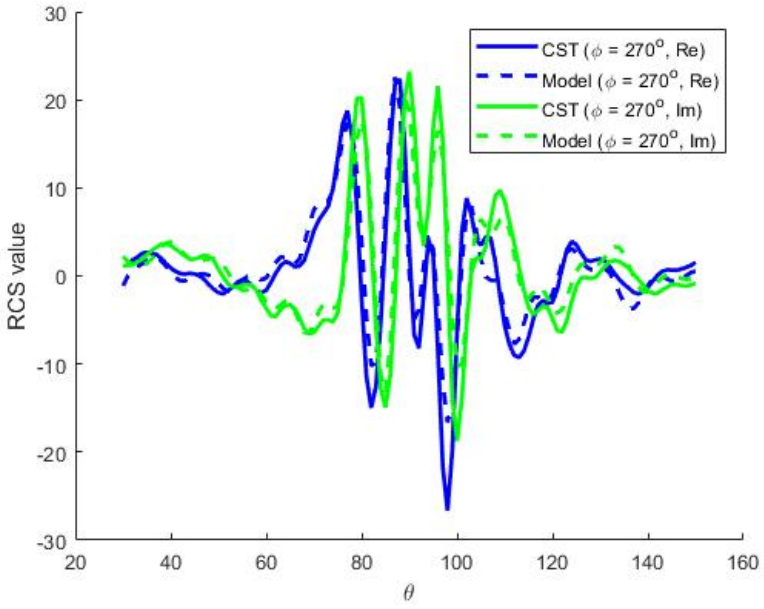

Figure 4.17: Comparison between the RCS from CST and the modeled RCS when varying θ.

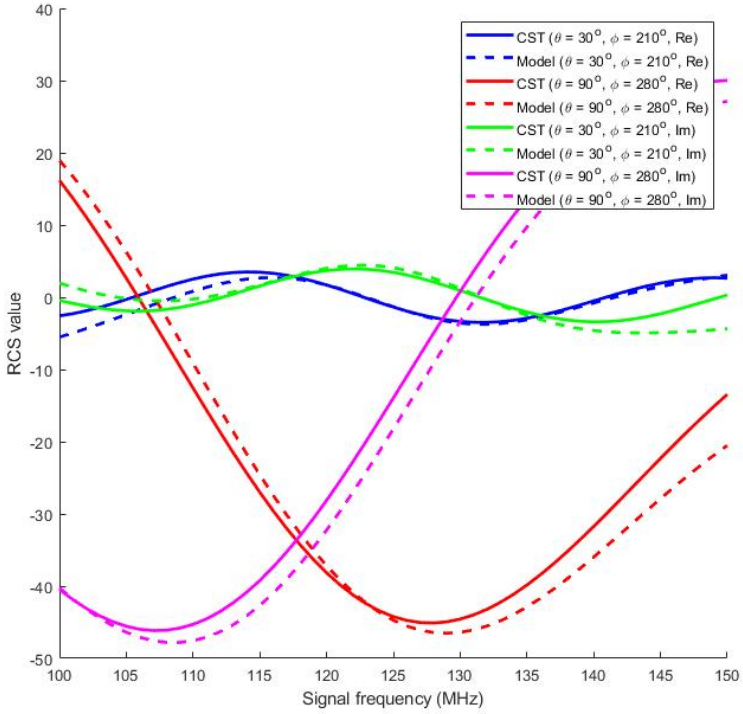

Figure 4.18: Comparison between the RCS from CST and the modeled RCS when varying the frequency.

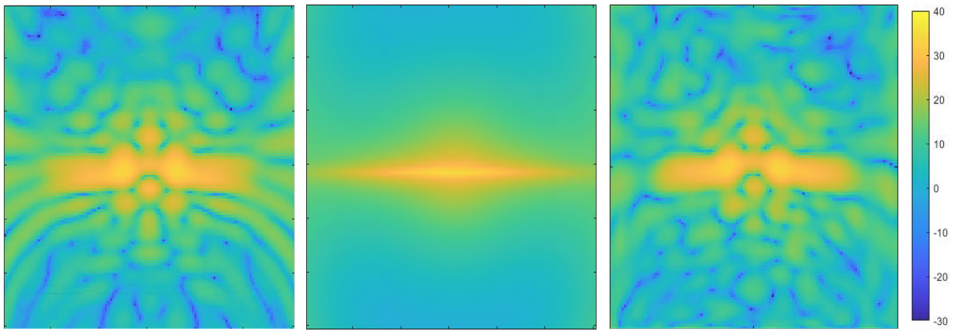

(a) RCS from CST

(b) Modeled RCS of ellipsoid model [13]

(c) Modeled RCS of proposed spherical harmonic model

Figure 4.19: RCS comparison between the ellipsoid model and the proposed spherical harmonic based point scatterer model.

The proposed anisotropic point scatterer model describes the monostatic RCS data of a radar target with a finite number of scatterer positions and spherical harmonic coefficients. The point scatterer model is constructed off-line and can be used by the HPC EM emulator to simulate EM wave interactions between multiple radar targets in real-time. To increase the model fidelity of the point scatterer model, one can

(i) Use more RCS data in the model generation process.

(ii) Increase the number of spherical harmonic basis functions so that the reflection profile of each scatterer becomes more complex.

(iii) Increase the number of scatterers.

Approach (i) and (ii) increase the computation time of the point scatterer model generation procedure since the algorithm involves more matrix computations. Approach (iii) not only increases the computation time of the model generation procedure, but also slows down the HPC EM emulator since the FIR filter will include more taps. Therefore, it is important to use as less scatterers as possible. Figure 4.20 shows the residual and the computation time of the point scatterer model as the number of scatterers increases.

To summarize this section, the spherical harmonic based monostatic anisotropic point scatterer model is proposed specifically for HPC EM interaction simulations where the scat-

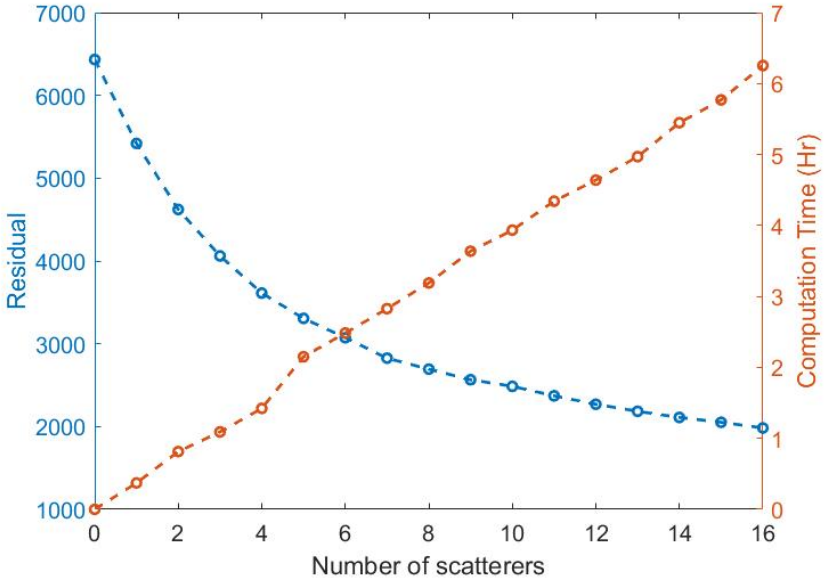

Figure 4.20: Residual and computation time

tering response can be computed with an FIR filter. An efficient algorithm for constructing this model with large-scale RCS data is discussed. The scatterer position and the reflection profile of each scatterer are solved using PSO and least squares methods. In addition, the function evaluations in PSO are accelerated by taking advantage of the matrix structure, making the algorithm 22 times faster compared to the naive approach, making the iterative method feasible. The results show that the point scatterer model can effectively represent the RCS data of a radar target. Same as mentioned in the previous section, the position obtained with this algorithm can be used to further compute the spherical harmonic based bistatic point scatterer model using the full bistatic RCS data.

In this Chapter, HPC-based EM emulators are discussed to simulate real-time complex EM wave interactions between multiple radar targets, transmitters, and receivers. RCS of the radar targets is required to be stored as a table. The needed storage size increases dramatically with the angle and frequency sampling density. We present innovative approaches of constructing concise point scatterer models that the emulators can use as part of the computations. These point scatterer models are constructed directly from the precomputed RCS data. The isotropic sphere and anisotropic ellipsoid scatterer models are

obtained by solving least square inverse problems. To improve the correlation with EM solvers, we further break down the optimization problem by considering the shadowing effect and use multiple models to represent a subset of the RCS data. Next, spherical harmonic based anisotropic point scatterer models are presented. We use only the monostatic RCS data and compute the spherical harmonic based monostatic point scatterer model by solving a linear least squares problem which has a group sparsity constraint. Then, we further compute the spherical harmonic based bistatic point scatterer model using the full bistatic RCS data. This problem is formulated as a bilinear least squares problem and solved using the normalized iterative algorithm, which linearly solves two parameters in a back-and-forth manner. The results show that the point scatterer model can effectively represent the bistatic RCS data of a radar target. Lastly, we lift the restriction of having to know a finite number of possible scatterer positions, which restricts the solutions of the scatterer positions from the continuous space. This is achieved by the proposed efficient monostatic point scatterer modeling technique, which takes advantage of the matrix structure, making the algorithm 22 times faster compared to the naive approach.

CHAPTER 5
HIGH DIMENSIONAL BAYESIAN OPTIMIZATION FOR MICROWAVE DESIGN

Another arising application of EM analysis is microwave design optimization problems. The mathematical optimization problems can be written as:

$$\min_{\boldsymbol{x}}/\max f(\boldsymbol{x}) \text{ subject to } \boldsymbol{x} \in \mathcal{X} \tag{5.1}$$

where $\boldsymbol{x}$ is the vector of input parameters, $f(\boldsymbol{x})$ is the objective function, and $\mathcal{X}$ is the feasible range of input parameters, also called the design space. Linear and convex optimization problems (LP and CP) can be solved efficiently using iterative methods or linear algebraic techniques due to the properties of simple function surfaces. However, in microwave design scenarios, the nonconvex function surfaces often consist of many local optima and make the optimization problems more challenging. In addition, the black-boxed nature of the problem (Figure 5.1) indicates the lack of gradient information. Gradient-free global optimization algorithms, such as genetic algorithm (GA) and particle swarm optimization algorithm (PSO) have been proposed to solve optimization problems using heuristic methods. Yet, due to the complex EM structures in microwave designs, the function evaluation $f(\boldsymbol{x})$ often requires lengthy EM simulations. The accumulated computation time hinders the feasibility of GA and PSO due to the large number of iterations that these algorithms require. Bayesian Optimization (BO) is a machine learning based method that enables fast convergence towards a global optimum and is well-known for reducing the computation time by efficient sampling. This is achieved by fitting a probabilistic surrogate model with existing data and optimizing the acquisition function to decide the next sampling point in a heuristic manner. This method has been applied to multi-physic microwave design

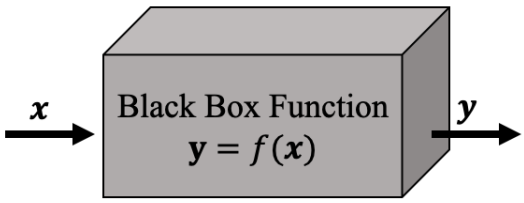

Figure 5.1: Black-boxed function

applications with experimental validation as shown in [67][68].

The general problem with BO is the low dimensionality of the problem that needs to be addressed which is contrary to microwave design. We propose an innovative method that prioritizes a subset of the design parameters for Gaussian process (GP) regression and acquisition function optimization in each iteration, where the subset selections are based on the estimated sensitivity of each parameter to the objective function. To illustrate the advantage obtained using BO with parameter prioritization, we apply this modified BO to two emerging system designs, namely the beamforming antenna in package design for wireless communication and the wireless power transfer (WPT) for Internet of Things (IoT), where the dimensionality of the problems to be addressed needs to be quite large. The results based on the modified BO described in this paper show that the optimization is possible with a smaller number of function evaluations.

The mathematical background of BO is introduced. Next, we propose the methodology that further improves the performance and include the algorithm pseudo code. Simulation results of the antenna and WPT designs are presented and the results between multiple algorithms are compared.

5.1 Bayesian optimization

The majority of microwave design problems require CPU-intensive and time-consuming simulations of multiphysic structures. BO is a well-known method for optimizing expensive black-boxed functions where a closed-form expression is unavailable. BO is an active learning algorithm including two steps in each iteration:

1. Learning a GP surrogate model that represents the data, where the posterior distribution of the function is obtained from the prior knowledge of the previously sampled points.

2. Using the GP model along with an acquisition function $u(\boldsymbol{x})$ to choose the next sampling point $\boldsymbol{x}_{t+1}$ for evaluation.

5.1.1 Gaussian Process Regression

GP is an extension of standard multivariate Gaussian distribution to the function space, where a finite number of samples form a joint Gaussian distribution. The prior of a GP model is defined with two quantities, namely a mean μ and a covariance matrix K, given by:

$$y = f(\boldsymbol{x}) \sim \mathcal{N}(\mu(\boldsymbol{x}), K) \tag{5.2}$$

where $\mathcal{N}$ represents a GP, $\boldsymbol{x} \in \mathbb{R}^D$ represents the input of the function, and y represents the function evaluation. For general nonlinear regression, a constant mean function $\mu(\boldsymbol{x}) = m$ is used [69]. The covariance matrix $K(\boldsymbol{X})$ describes the relation between a number of points $\boldsymbol{X}$ in the function and is written as:

$$K_{\boldsymbol{X}} = \begin{bmatrix} k(\boldsymbol{x}_1, \boldsymbol{x}_1) & \dots & k(\boldsymbol{x}_1, \boldsymbol{x}_t) \\ \vdots & \ddots & \vdots \\ k(\boldsymbol{x}_t, \boldsymbol{x}_1) & \dots & k(\boldsymbol{x}_t, \boldsymbol{x}_t) \end{bmatrix} \tag{5.3}$$

Appropriate kernel functions can be applied to capture different patterns in the dataset. For example, the Matern 5/2 kernel is commonly used [69][70]:

$$k\left(\boldsymbol{x}_i, \boldsymbol{x}_j\right) = \sigma_f^2 \left(1 + \sqrt{5}r + \frac{5}{3}r^2\right) e^{-\sqrt{5}r} \tag{5.4}$$

$$r = \left(\sum_{d=1}^{D} \frac{\left(\boldsymbol{x}_{i,d} - \boldsymbol{x}_{j,d}\right)^2}{\sigma_d^2}\right)^{\frac{1}{2}} \tag{5.5}$$

where σ_f is the output scale and σ_d is the length scale of the d^{th} dimension. $[\sigma_f, \sigma_1, ..., \sigma_D]^T$ is defined as $\boldsymbol{\theta}$ and represents the hyperparameters of $K_{\boldsymbol{X}}$. These hyperparameters are updated during the training process by minimizing the negative log marginal likelihood of the GP using the dataset $\mathcal{D} = \{\boldsymbol{X}, \boldsymbol{Y}\}$:

$$\boldsymbol{\theta}^* = \underset{\boldsymbol{\theta}}{\operatorname{argmin}} - \log p(\boldsymbol{Y}|\boldsymbol{X}, \boldsymbol{\theta}) \tag{5.6}$$

After training, the GP model can then predict the unknown function evaluation $\tilde{y}$ of a new input data $\tilde{\boldsymbol{x}} \in \mathbb{R}^D$ using the following conditional rules [44]:

$$p(\tilde{y}, \boldsymbol{Y}|\tilde{\boldsymbol{x}}, \boldsymbol{X}, \boldsymbol{\theta}^*) = \mathcal{N}\left(\begin{bmatrix} \mu_{\boldsymbol{X}} \\ \mu_{\tilde{\boldsymbol{x}}} \end{bmatrix}, \begin{bmatrix} K_{\boldsymbol{X}} & K_{\boldsymbol{X},\tilde{\boldsymbol{x}}} \\ K_{\boldsymbol{X},\tilde{\boldsymbol{x}}}^T & K_{\tilde{\boldsymbol{x}},\tilde{\boldsymbol{x}}} \end{bmatrix}\right) \tag{5.7}$$

$$\tilde{y} \sim \mathcal{N}(\tilde{\mu}(\boldsymbol{x}), \tilde{K}) \tag{5.8}$$

$$\tilde{\mu}(\boldsymbol{x}) = K_{\boldsymbol{X},\tilde{\boldsymbol{x}}}^T K_{\boldsymbol{X}}^{-1} f(\boldsymbol{X}) \tag{5.9}$$

$$\tilde{K} = K_{\tilde{\boldsymbol{x}},\tilde{\boldsymbol{x}}} + K_{\boldsymbol{X},\tilde{\boldsymbol{x}}}^T K_{\boldsymbol{X}}^{-1} K_{\boldsymbol{X},\tilde{\boldsymbol{x}}} \tag{5.10}$$

Along with the trained GP model, an acquisition function chooses the next sampling

point to be evaluated.

5.1.2 Acquisition Functions

There are three commonly used acquisition functions, namely the probability of improvement (PI), expected improvement (EI), and upper confidence bound (UCB) given by:

$$I(\boldsymbol{x}) = \begin{cases} 0 & f(\boldsymbol{x}) > f' \\ 1 & f(\boldsymbol{x}) \leq f' \end{cases} \tag{5.11}$$

$$I_2(\boldsymbol{x}) = \max\left(0, f' - f(\boldsymbol{x})\right) \tag{5.12}$$

$$u_{\mathrm{PI}}(\boldsymbol{x}) = \mathbb{E}[I(\boldsymbol{x})] \tag{5.13}$$

$$u_{\mathrm{EI}}(\boldsymbol{x}) = \mathbb{E}[I_2(\boldsymbol{x})] \tag{5.14}$$

$$u_{\mathrm{UCB}} = \mu(\boldsymbol{x}) + \beta\sigma(\boldsymbol{x}) \tag{5.15}$$

where f' is the optimal evaluation so far, β is a hyperparameter [44] [71]. EI outperforms PI since PI ignores the amount of improvement and thus oftentimes converges to an unsatisfying local optimum. UCB is used when the trade-off between exploration and exploitation is defined. The set of input parameters that maximizes $u(\boldsymbol{x})$ is selected as the next sampling point, $\boldsymbol{x}_{t+1}$. Since $u(\boldsymbol{x})$ is no longer a CPU-intensive or time-consuming black-boxed function, the maximization or minimization procedure can be performed more easily. A robust and commonly used optimization method for acquisition functions is as follows: First, create a number of quasi-random points from the design space, $\mathcal{X}$. Next, assign weights to the points according to the acquisition function evaluations. A number of samples are

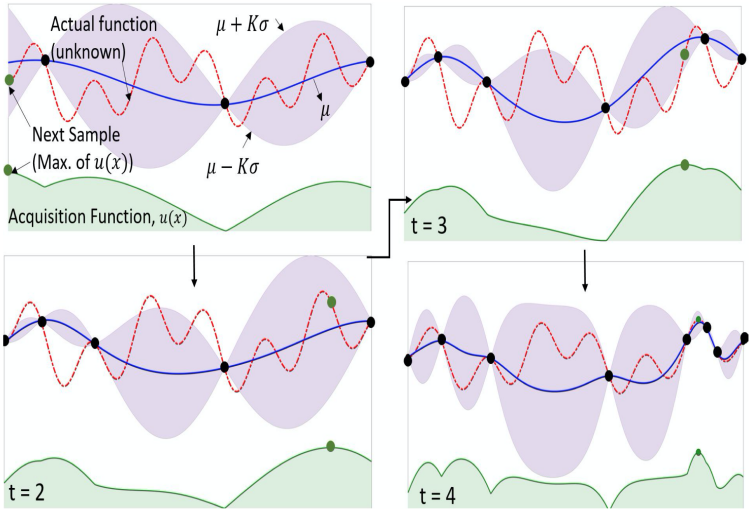

Figure 5.2: Graphical illustration of BO [67]

then drawn according to these weights. Lastly, these new samples are used as initial points for gradient descent methods to reach the maximal $u(\boldsymbol{x})$. In summary, BO transforms the original optimization problem into a series of smaller and easier optimization problems, which enables less number of function evaluations. The detailed illustration of BO can be found in [45] and the graphical illustration is shown in Figure 5.2. In the next section, an innovative method to address high-dimensional optimization problems is proposed.

5.2 High Dimensional Bayesian Optimization

A general problem with BO is the low dimensionality of the problem that needs to be addressed which is contrary to microwave design that often requires many parameters to be optimized with precision. The challenges of implementing conventional BO to high dimensional problems are due to the curse of dimensionality [46] [47]. For example, the search space, $\mathcal{X}$, expands exponentially as the number of input parameters increases. Thus, the surrogate models cannot well represent a function without an extremely large number of data. This is infeasible for microwave designs due to the CPU-intensive and time-consuming EM simulations. In addition, the acquisition function optimization becomes unsolvable or time-consuming, which leads to poor suggestions of the next sampling point.

Microwave design often requires many parameters to be optimized. Yet, BO has been observed to perform poorly on high-dimensional problems. We propose to prioritize a subset of the design parameters for GP regression and acquisition function optimization in each iteration, where the subset selections are based on the estimated sensitivity of each parameter to the objective function. These sensitivity estimations are obtained from the automatic relevance determination (ARD) kernel functions.

5.2.1 Automatic Relevance Determination

A GP regression with ARD kernel functions assumes independent relations between each dimension to another and applies independent priors over the length scales in the kernel functions [70]. Matern 5/2 kernel, as shown in Equation 5.4, is an ARD kernel since each hyperparameter σ_d represents only the length scale of the d^{th} dimension. Due to the independency, these length scales can be used as sensitivity estimations. For example, consider maximizing a 2-dimensional function with BO using 10 sample points:

$$y(\boldsymbol{x}) = -((x_1 - 0.5)^2 + 4(x_2 - 0.5)^2) \tag{5.16}$$

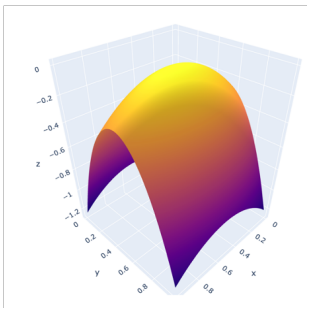

(a) True function

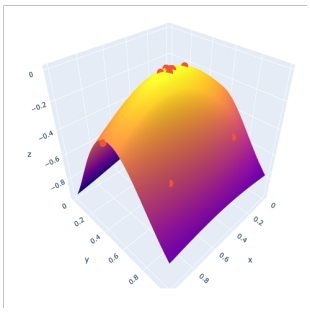

(b) Approximated function

Figure 5.3: Simple function

, where $\boldsymbol{x} = [x_1, x_2]^T \in \mathbb{R}^2$. The Z-axis represents the function surface. As shown in Figure 5.3, the function is well captured with the GP model after the training process. The updated hyperparameter σ_1 and σ_2 is 1.06 and 0.57, respectively. This indicates that the modeled function is flatter and smoother along the first dimension, whereas more sensitive and varies more along the second dimension.

5.2.2 Bayesian Optimization with Parameter Prioritization

We propose to prioritize a subset of the design parameters for GP regression and acquisition function optimization during each BO iteration according to these length scales. The detailed algorithm is shown as Algorithm 4. First, the objective function $f(\boldsymbol{x})$, acquisition function $u(\boldsymbol{x})$, kernel function $k(\boldsymbol{x}_i, \boldsymbol{x}_j)$, and the number of total evaluation budget T are defined as in conventional BO. The number of initial random sample points M determines the random exploration before running the GP regression process. Compared to conventional BO, this modified BO algorithm requires more exploration for the sensitivity

prioritization. The number of design parameters subset S indicates the number of parameters considered for the GP regression and acquisition function optimization. It is chosen to be less than the original dimension D enabling BO to operate in a lower dimension.

For each iteration, the statistical model, GP, is trained to minimize the negative log marginal likelihood of the data set $\mathcal{D}$ as shown in Equation 5.6. The trained hyperparameters, namely the length scales of the ARD kernel in Equation 5.5, are used as the sensitivity estimations. The S most sensitive parameters are extracted. These parameters along with the output form the new data set $\overline{\mathcal{D}}$ are used to train a low dimensional GP model $\overline{GP}$. This model more concisely represents the function while treating the contribution from other dimensions as noise. Using $\overline{GP}$, the acquisition function is optimized to suggest a low dimensional candidate for the next sampling point, $\overline{\boldsymbol{x}}_{t+1}$ as mentioned in Section II B. Note that $\overline{GP}$ is low dimensional thus the candidate grants more improvements compared to the candidate obtained from the high dimension GP models. The candidate is combined with the previously obtained optimizer in the remaining dimensions to create the new full-dimensional candidate for the next sampling point, $\boldsymbol{x}_{t+1}$.

$$\boldsymbol{x}_{t+1} = [\bar{x}_{t+1}, x^*_{S+1:D,t}]^T \tag{5.17}$$

Lastly, $\boldsymbol{x}_{t+1}$ is evaluated and the data is added to update the data set $\mathcal{D}$. These steps are iterated until the evaluation budget is used up.

Algorithm 4: BO with Parameter Prioritization

Result: Global optimizer and optima

Initialization:

1. Define $f(\boldsymbol{x})$, $u(\boldsymbol{x})$, $k\left(\boldsymbol{x}_i, \boldsymbol{x}_j\right)$, T, M, S.
2. Evaluate initial sample points $y_{1:M} = f\left(\boldsymbol{x}_{1:M}\right)$
3. Collect data $\mathcal{D} = \{\boldsymbol{X}, \boldsymbol{Y}\} = \{\boldsymbol{x}_{1:M}, y_{1:M}\}$

for $t = 1 \rightarrow T$ **do**

Fit GP with $\mathcal{D}$
Select S parameters with small length scales σ
Create low dimensional data set $\overline{\mathcal{D}} = \left\{\overline{\boldsymbol{X}}, \boldsymbol{Y}\right\}$
Fit $\overline{GP}$ with $\overline{\mathcal{D}}$
Optimize acquisition func: $\overline{\boldsymbol{x}}_{t+1} = \operatorname{argmax}_{\overline{\boldsymbol{x}}} u(\overline{\boldsymbol{x}})$
Merge $\overline{\boldsymbol{x}}_{t+1}$ with previous optimizer to get $\boldsymbol{x}_{t+1}$
Evaluate at the new sample point $f(\boldsymbol{x}_{t+1})$
Update data set $\mathcal{D}$

end

5.3 Microwave Design Simulation Results

The BO with parameter prioritization is applied to two high-dimensional system design problems, namely the beamforming antenna in package design for wireless communication and the WPT for IoT. The comparison between the performances using multiple algorithms is also provided.

5.3.1 Beamforming Antenna Design

A Butler matrix subarray consisting of four microstrip antennas is shown in Figure 5.4 and Table 5.1 [72] [73]. The number of geometrical configuration design parameters is increased to 21 as opposed to 7 used in [73]. The Butler matrix subarray is designed such that every four elements have eight phase shift combination options controlled by the phase shifter switch as shown in Figure 5.5. These switches are implemented by sending power to the corresponding ports. Each phase shift combination creates a beam pointing along a certain direction. This is considered as the first-level beamforming. Then, the beamformers provide continuous phase shifts and are tunable according to the desired beam direction. This second-level beamforming fine-tunes the beam direction. Several subarrays as in Figure 2.1 and Figure 5.6 are connected together to steer the beam along a two-dimensional direction.

The optimization problem can be defined as:

$$\min_{\boldsymbol{x}} \int_{\Theta_d} J\left(\theta_d; \boldsymbol{x}\right) d\theta_d \tag{5.18}$$

where $\boldsymbol{x} \in R^D$ is the geometrical configuration parameter vector. In this example, $D = 21$ represents the number of geometrical configuration parameters, $\theta_d \in R^2$ is the desired beam direction in spherical coordinates and Θ_d is the set of possible desired beam directions. In Equation 5.18, $J\left(\theta_d\right)$ is the cost function that captures the performance degradation due to the radiation towards undesired angles when the desired beam direction is θ_d. This

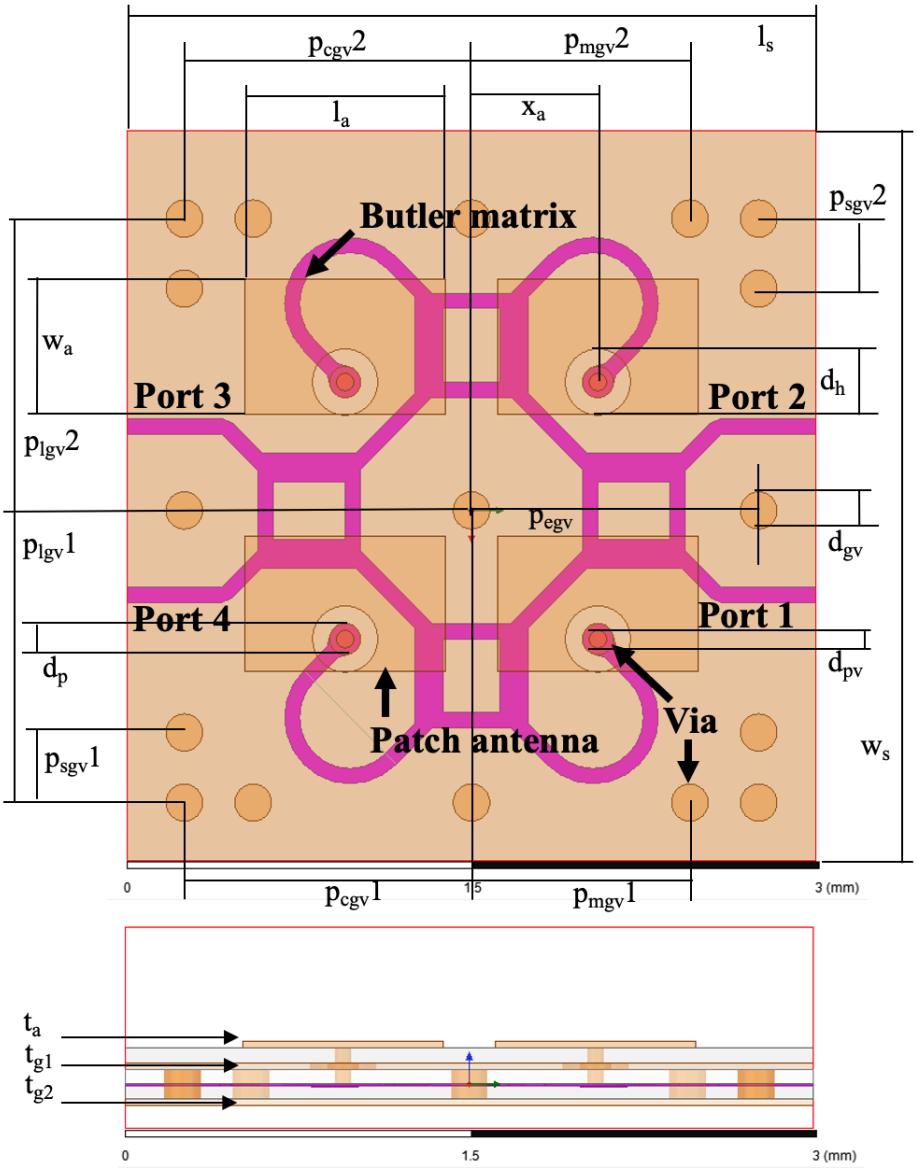

Figure 5.4: Geometrical configuration of subarray

Table 5.1: Design parameters for beamforming antenna

Parameter (μm)	**Manual**	**Optimized**	**Range**
Patch antenna width (w_a)	870.0	718.8	[670, 1070]
Patch antenna length (l_a)	580.0	540.0	[430, 730]
Patch antenna position (x_a)	0.0	51.8	[0, 100]
Antenna copper thickness (t_a)	20.0	15.0	[10, 25]
Hole diameter offset (d_h)	150.0	135.1	[120, 140]
Patch via diameter (d_{pv})	75.0	101.6	[70, 120]
Pad diameter offset (d_p)	60.0	65.8	[60, 100]
Ground via diameter (d_{gv})	160.0	148.8	[110, 200]
Substrate width offset (w_s)	0.0	0.0	[0, 300]
Substrate length offset (l_s)	0.0	74.4	[0, 300]
Gnd copper thickness 1 (t_g1)	20.60	25.0	[10, 25]
Gnd copper thickness 2 (t_g2)	20.0	10.0	[10, 25]
Side via position 1 ($p_{sgv}1$)	300.0	281.8	[250, 300]
Corner via position 1 ($p_{cgv}1$)	50.0	45.8	[40, 60]
Middle via position 1 ($p_{mgv}1$)	300.0	314.2	[280, 320]
Lower via position 1 ($p_{lgv}1$)	0.0	13.6	[0, 30]
Side via position 2 ($p_{sgv}2$)	300.0	500.0	[250, 500]
Corner via position 2 ($p_{cgv}2$)	50.0	54.7	[40, 60]
Middle via position 2 ($p_{mgv}2$)	300.0	296.1	[280, 320]
Lower via position 2 ($p_{lgv}2$)	0.0	1.28	[0, 30]
Edge via position (p_{egv})	50.0	46.6	[40, 60]

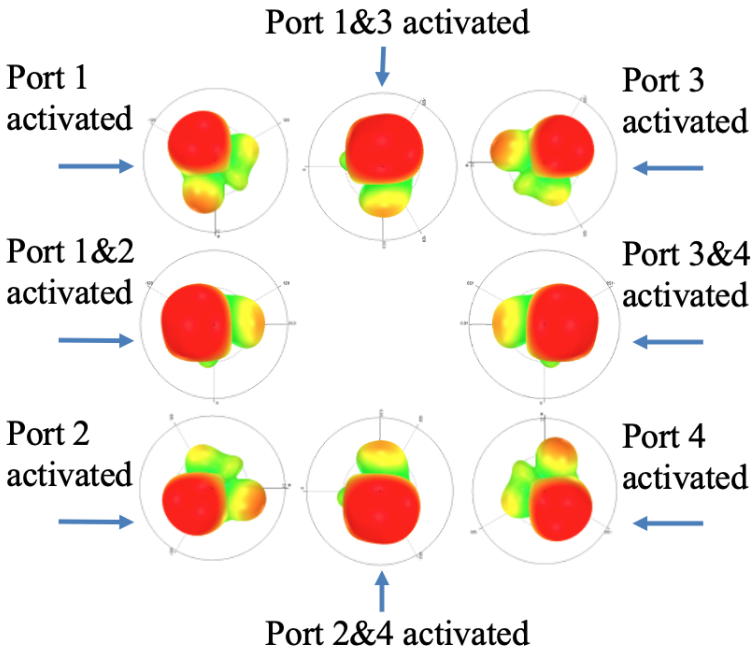

Figure 5.5: Phase shifter options

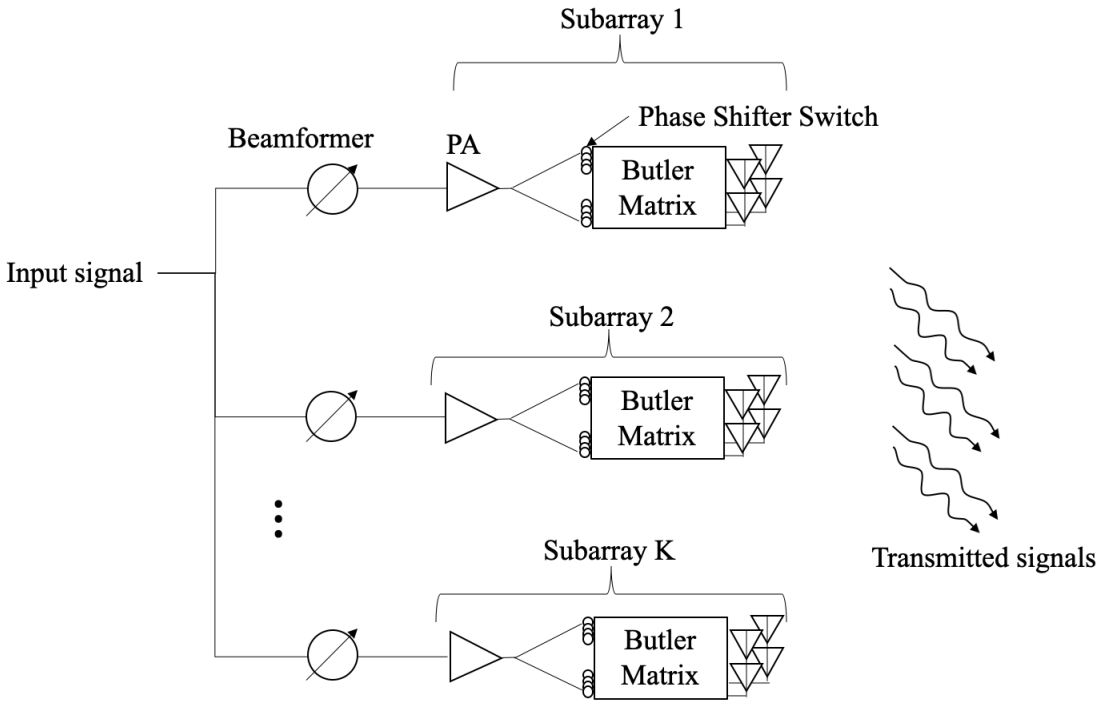

Figure 5.6: Signal flow

degradation integrated along all possible desired beam directions needs to be minimized. $J(\theta_d; \boldsymbol{x})$ is defined as:

$$J(\theta_d, \boldsymbol{\xi}, \boldsymbol{\psi}; \boldsymbol{x}) = \frac{\max_{\theta_c \in \Theta_c} |G(\theta_c, \boldsymbol{\xi}, \boldsymbol{\psi}; \boldsymbol{x})|^2}{|G(\theta_d, \boldsymbol{\xi}, \boldsymbol{\psi}; \boldsymbol{x})|^2} \tag{5.19}$$

where $\boldsymbol{\xi} \in C^K$ is the beamformer vector, K is the number of beamformers (same as the number of subarrays), $\boldsymbol{\psi}$ indicates the positions of the phase shifter switches, $\theta_c \in R^2$ is the interference direction in spherical coordinates, and Θ_c is the set of interfering directions given θ_d. A 2D illustration of the relation between θ_d and Θ_c is shown in Figure 5.7. $G(\theta, \boldsymbol{\xi}, \boldsymbol{\psi}; \boldsymbol{x})$ is the complex response of the antenna along the direction θ using beamformers $\boldsymbol{\xi}$ and phase shifter switches $\boldsymbol{\psi}$ given by:

$$G(\theta; \boldsymbol{\xi}, \boldsymbol{\psi}, \boldsymbol{x}) = \sum_{k=1}^{K} g_{sub,k}(\theta, \boldsymbol{\psi}_k, \boldsymbol{x})\, e^{-2\pi i f \tau_{sub,k}(\theta)} \xi_k \tag{5.20}$$

$$\tau_{sub,k}(\theta) = -\frac{\langle \boldsymbol{x}_{sub,k}, \boldsymbol{d}(\theta) \rangle}{c} \tag{5.21}$$

where $g_{sub,k}(\theta, \boldsymbol{\psi}_k, \boldsymbol{x})$ is the radiation pattern of the k^{th} subarray (computed using EM simulators such as Ansys HFSS) given the subarray structure in Equation 5.20. In Equation 5.20, $\boldsymbol{\psi}_k$ is the phase shifter switch of the k^{th} subarray, $\tau_{sub,k}(\theta)$ is the time delay between the signal transmitted from the k^{th} subarray and the center of the entire array, $\boldsymbol{x}_{sub,k}$ is the position of the center of the k^{th} subarray, $\boldsymbol{d}(\theta)$ is the unit vector of the angle direction θ transformed to the Cartesian coordinate, and c represents the speed of light and $\langle \cdot, \cdot \rangle$ is the standard inner product in $\mathbb{R}^3$.

We repose Equation 5.18 for numerical computations in the form:

$$\min_{\boldsymbol{x}} \frac{1}{N} \sum_{\theta_d \in \Theta_d} J(\theta_d; \boldsymbol{x}) \tag{5.22}$$

where N is the number of desired beam angle samples in Θ_d.

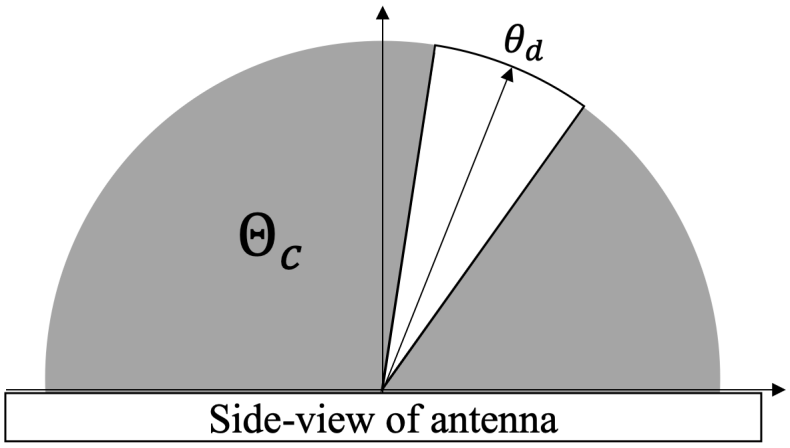

Figure 5.7: 2D illustration of the relation between θ_d and Θ_c

The optimization problem in Equation 5.22 is highly nonlinear and with a large number of decision variables. To simplify the problem, we apply the same phase shifter switches to all Butler matrices, and set the switches to maximize the Butler matrix response along the desired beam direction. In addition, the beamformers are assumed to compensate for the delays due to the position difference of the subarrays. In other words:

$$\boldsymbol{\psi}_1(\theta_d) = \boldsymbol{\psi}_2(\theta_d) = ... = \boldsymbol{\psi}_K(\theta_d) = \boldsymbol{\psi}^*_{sub}(\theta_d) \tag{5.23}$$

$$\boldsymbol{\psi}^*_{sub}(\theta_d) = \arg\max_{\boldsymbol{\psi}_{sub}} |g_{sub}(\theta_d, \boldsymbol{\psi}_{sub}, \boldsymbol{x})|^2 \tag{5.24}$$

$$\xi_k(\theta_d) = e^{2\pi i f \tau_{sub,k}(\theta_d)} \tag{5.25}$$

The subarray antenna design problems are solved as an optimization problem in Equation 5.22, where the objective function is a black box and involves time-consuming EM simulations. In our experiment, EI is chosen as the acquisition function. The function evaluation time is 7 minutes and the total evaluation budget T is set to 55. The number of initial random sample points M is chosen as $T/3 \cong 20$ for exploration. The number of design parameter subset S is set to 5 indicating that there are at least 5 parameters

dominating the function surface. The cost (based on Equation 5.22) comparison between the manual design [72], the design using PSO, the conventional BO, the BO with adaptive bound (BOAB) [73], and the proposed modified BO is shown in Figure 5.8 indicating the advantage obtained using BO with parameter prioritization. The manual design here refers to the design process without the use of optimization. The figure shows that the conventional BO and BOAB could not reach the global optima within 55 iterations. PSO shows unsatisfying improvement as well due to the small number of iterations. Although the modified BO with parameter prioritization does not find better optima within the beginning 20 random samplings, the obtained sensitivity information helps the algorithm to reach a better optimum within a small number of iterations. In addition, the modified BO reaches the performance of the manually hand-tuned design in the 20th iteration, while the conventional BO reaches the performance in the 34th iteration. This shows a time saved of 44%. The BOAB method reaches the performance of the manually hand-tuned design in the 22nd iteration, yet does not reach the global optimum. The counts of each parameter used for the GP regression and acquisition function optimization are shown in Figure 5.9 to demonstrate the parameter sensitivity ranking. Note that the parameters la and $tg1$ are chosen a lot which means that the GP model believes these parameters are worth focusing on during the GP regression process, while the parameters wa and ls are less contributive to the objective function. Figure 5.10 shows the comparison between the beam patterns from multiple optimization methods described where the mainbeam points towards $\theta_d = [30, 0]$, $[30, 15]$, $[30, 25]$, and $[30, 60]$, respectively. The radiation power is normalized with respect to the mainbeam of the manual design. The result shows that most of the mainbeam powers are increased significantly with the small amount of sidelobe increasements. Furthermore, in the $\theta_d = [30, 0]$ case, the mainbeam power is increased and the sidelobe is reduced after the optimization. The comparison of the parameters between the manually designed antenna and the optimized design is shown in Table 5.1.

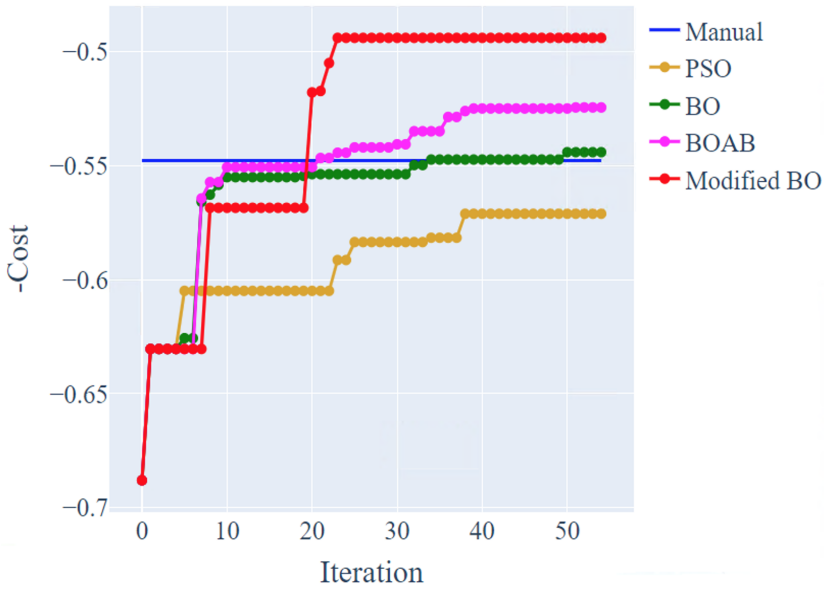

Figure 5.8: Cost comparison between the manual design, the design using PSO, the conventional BO, the BO with adaptive bound, and the proposed modified BO. Manual here refers to the design process without the use of optimization.

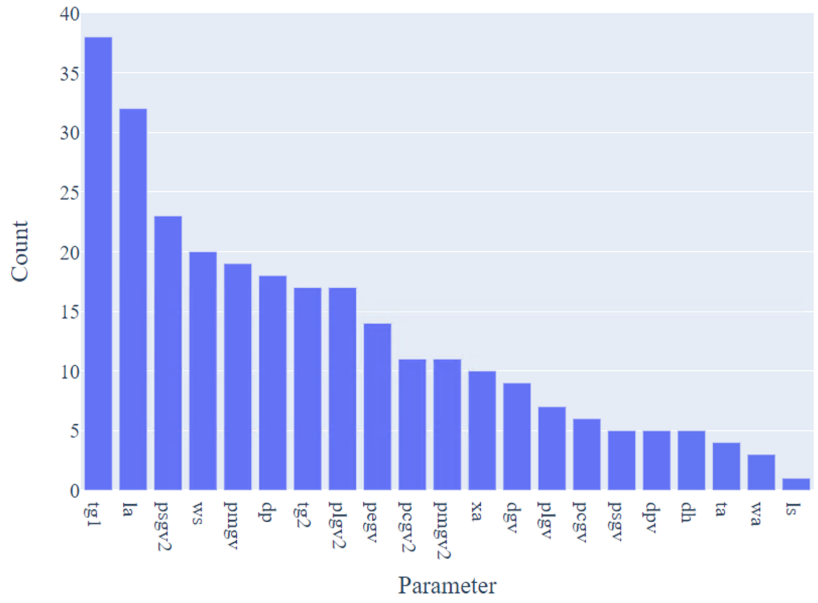

Figure 5.9: Beamforming antenna parameter sensitivity ranking

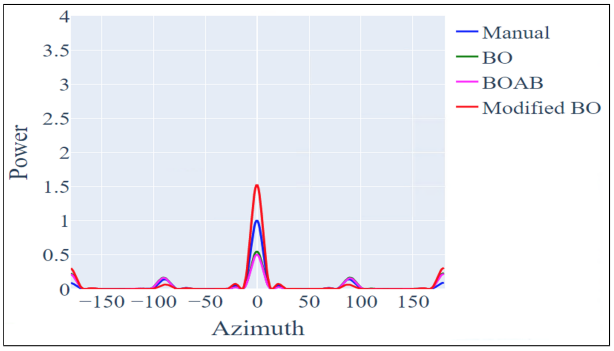

(a) $\theta_d = [30, 0]$

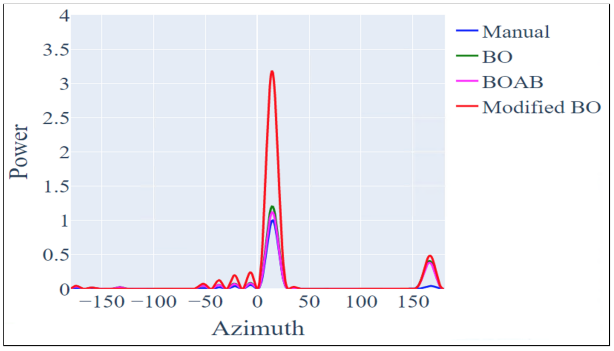

(b) $\theta_d = [30, 15]$

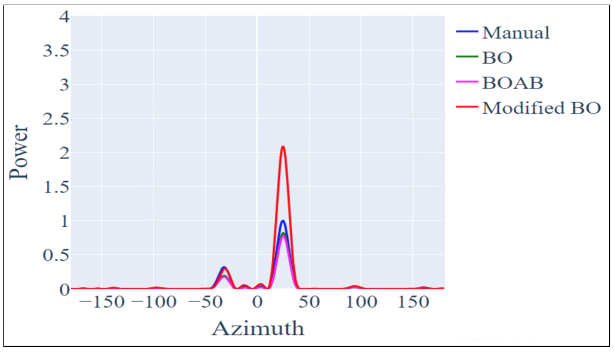

(c) $\theta_d = [30, 25]$

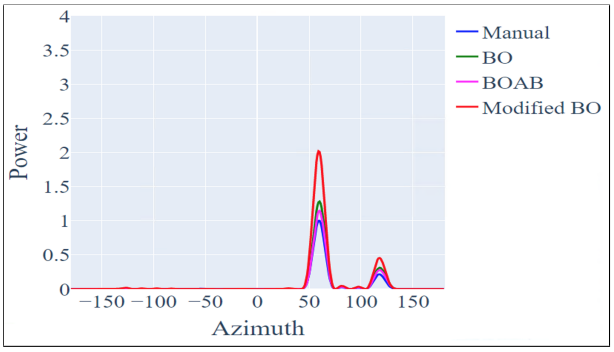

(d) $\theta_d = [30, 60]$

Figure 5.10: Antenna beam pattern comparison

Additional Beamforming Method

Other beamforming methods are also applicable to the subarray design optimization problem. For example, in the case where each beamformer includes the phase delay and magnitude modulation functions, the optimization problem is instead defined as:

$$J\left(\theta_d;\boldsymbol{x}\right)=\min_{\boldsymbol{\xi},\boldsymbol{\psi}}\int_{\Theta_c(\theta_d)}\left|G\left(\theta_c,\boldsymbol{\xi},\boldsymbol{\psi};\boldsymbol{x}\right)\right|^2 d\theta_c \quad \text{s.t. } G\left(\theta_d,\boldsymbol{\xi},\boldsymbol{\psi};\boldsymbol{x}\right)=1 \tag{5.26}$$

The constraint $G\left(\theta_d,\boldsymbol{\xi},\boldsymbol{\psi};\boldsymbol{p}\right)=1$ is posed in order to solve for the ratio between the magnitudes of the beamformers such that the directivity of the antenna is maximized. With the phase shifter switches determined, the problem is simplified to

$$J\left(\theta_d;\boldsymbol{x}\right)=\min_{\boldsymbol{\xi}}\frac{1}{B}\sum_{\theta_c\in\Theta_c(\theta_d)}\left|G\left(\theta_c,\boldsymbol{\xi};\boldsymbol{x}\right)\right|^2 \quad \text{s.t. } G\left(\theta_d,\boldsymbol{\xi};\boldsymbol{x}\right)=1 \tag{5.27}$$

, where

$$G\left(\theta;\boldsymbol{\xi},\boldsymbol{x}\right)=\sum_{k=1}^{K}g_{sub}\left(\theta,\boldsymbol{x}\right)e^{-2\pi i f\tau_{sub,k}(\theta)}\xi_k \tag{5.28}$$

This problem can be formulated as a Quadratic Programming (QP) problem in the complex domain:

$$\bar{J}\left(\theta_d;\boldsymbol{x}\right)=\min_{\boldsymbol{\xi}\in C^K}\boldsymbol{\xi}^H\boldsymbol{A}\boldsymbol{\xi} \quad \text{s.t. } \bar{\boldsymbol{b}}^H\boldsymbol{\xi}=1 \tag{5.29}$$

$$\boldsymbol{A}=\frac{1}{B}\sum_{\theta_c\in\Theta_c(\theta_d)}\bar{\boldsymbol{a}}\bar{\boldsymbol{a}}^H \tag{5.30}$$

$$\boldsymbol{a}=g_{sub}\left(\theta_c,\boldsymbol{x}\right)e^{-2\pi i f\boldsymbol{\tau}_{sub}(\theta_c)} \tag{5.31}$$

$$\boldsymbol{b}=g_{sub}\left(\theta_d,\boldsymbol{x}\right)e^{-2\pi i f\boldsymbol{\tau}_{sub}(\theta_d)} \tag{5.32}$$

, where $\boldsymbol{\tau}_{sub} \in R^K$ is a vector of time delays of all subarrays. $\boldsymbol{A} \in C^{K \times K}$, and it is positive definite since it is a scaled summation of quadratic functions. $\bar{\boldsymbol{a}}$ is the conjugate of $\boldsymbol{a}$. $\bar{\boldsymbol{b}}$ is the conjugate of $\boldsymbol{b}$. QP problems are convex thus the optimal beamformers can be computed with off-the-shelf solvers. The flow chart for the cost function evaluation of this beamforming method is shown in Figure 5.11.

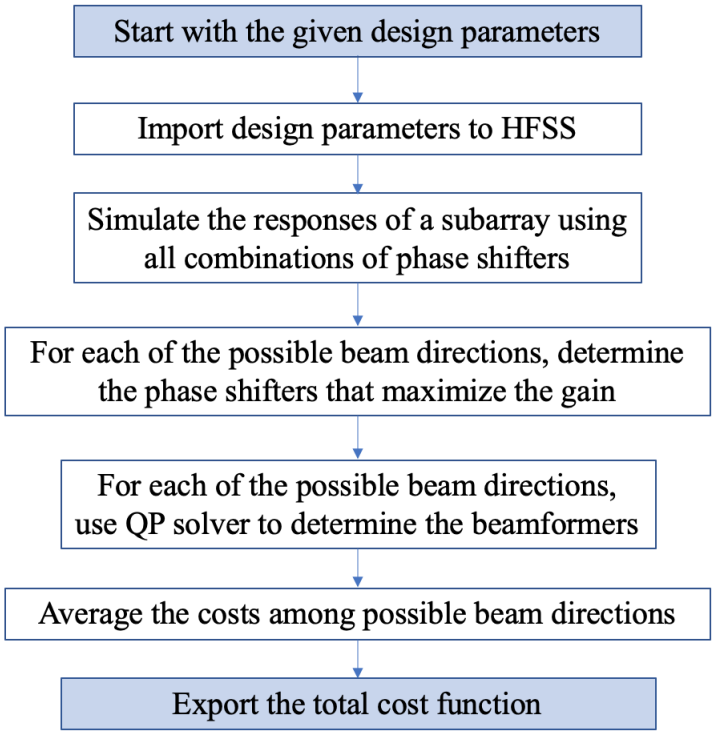

Figure 5.11: Beamforming method for cost function evaluation

5.3.2 Wireless Power Transfer Design

A WPT system targets power transmission and conversion without wires or physical links. The power is transmitted through the magnetic fields with inductive couplings by coils. The challenges arise when the coils are operated at high frequency due to the low efficiency and increased power loss. We address this problem in two parts i) maximizing the RF-to-DC conversion efficiency, and ii) maximizing the RF-to-DC conversion efficiency while minimizing the coil area. The purpose here is to address both a single-objective and multi-objective optimization problem. The architecture of the inductive coupling-based WPT system is shown in Figure 5.12 [67] [73]. The system operates at 1GHz and is an integrated board solution consisting of embedded rectangular RF coils. These coils are connected to the transmit (TX) and receive (RX) matching networks which consist of the LC networks. A full bridge diode rectifier is connected and a buck converter (BC) with an embedded inductor is used for DC regulation. The design parameters for the system are shown in Table 5.2.

In this experiment, the number of parameters is 30 ($D = 30$). EI is used as the acquisition function. Similar to before, the total evaluation budget T is set to 55, and the number of initial random sample points M is set to 20. The number of design parameter subset S is set to 15. The time of each function evaluation experiment is 3.5 minutes. The power transfer efficiency comparison between the WPT design using PSO, the conventional BO, and the proposed modified BO is shown in Figure 5.13. The figure shows that the efficiency is improved using BO with parameter prioritization since the conventional BO is stuck in a local optimum. As in the previous example, the design using PSO shows unsatisfying improvement due to the small number of iterations. The counts of each parameter used for the GP regression and acquisition function optimization are shown in Figure 5.14 demonstrating the parameter sensitivity ranking. The optimized parameters that maximize the power transfer efficiency of the WPT system are shown in Table 5.2. Note that the modified BO requires only 21 iterations to reach the maximum efficiency obtained using

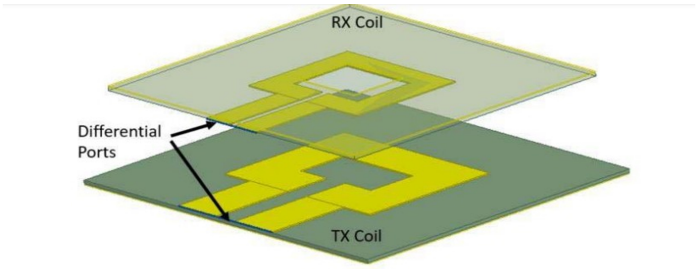

(a)

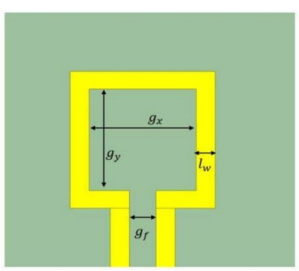

(b)

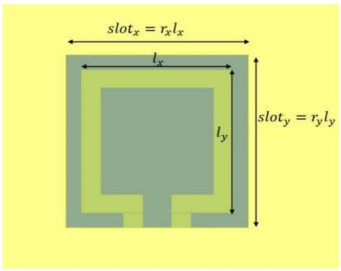

(c)

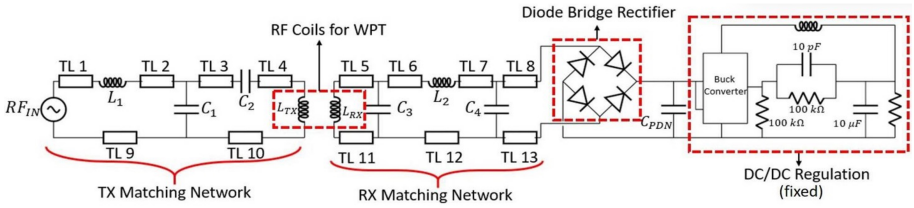

(d)

Figure 5.12: (a)∼(c) Geometry of the embedded RF coils defining the design parameters, and (d) Schematic of the WPT-based power delivery architecture [67]

Table 5.2: Design parameters for WPT system

Parameter	**Optimized**	**Range**
Feeding gap for TX coil ($g_{f,TX}$)	2.99 mm	[2, 3]
Feeding gap for RX coil ($g_{f,RX}$)	2.12 mm	[2, 3]
Width/height of TX coil ($g_{xy,TX}$)	2.25 mm	[2, 3]
Width/height of RX coil ($g_{xy,RX}$)	2.42 mm	[2, 3]
Gnd cut-out ratio TX ($slot_{xy,TX}$)	1.14	[1, 1.2]
Gnd cut-out ratio RX ($slot_{xy,RX}$)	1.01	[1, 1.2]
Match capacitor TX (C_1)	4.87 pF	[4, 5]
Resonance capacitor TX (C_2)	4.78 pF	[4, 5]
Resonance capacitor RX (C_3)	2.91 pF	[2, 3]
Match capacitor RX (C_4)	0.75 pF	[0.1, 1]
Match inductor TX (L_1)	0.13 nH	[0.1, 2]
Match inductor RX (L_2)	7.22 nH	[7, 8]
Line width TX coil ($l_{w,TX}$)	1.57 mm	[1, 2]
Line width RX coil ($l_{w,RX}$)	0.81 mm	[0.5, 1]
Width TL1 (W_{TL1})	0.63 mm	[0.35, 1.15]
Width TL2 (W_{TL2})	0.58 mm	[0.35, 1.15]
Width TL3 (W_{TL3})	0.82 mm	[0.35, 1.15]
Width TL4 (W_{TL4})	0.53 mm	[0.35, 1.15]
Width TL5 (W_{TL5})	0.90 mm	[0.35, 1.15]
Width TL6 (W_{TL6})	0.78 mm	[0.35, 1.15]
Width TL7 (W_{TL7})	0.83 mm	[0.35, 1.15]
Width TL8 (W_{TL8})	1.02 mm	[0.35, 1.15]
Length TL1 (L_{TL1})	0.97 mm	[0.5, 5]
Length TL2 (L_{TL2})	3.64 mm	[0.5, 5]
Length TL3 (L_{TL3})	0.71 mm	[0.5, 5]
Length TL4 (L_{TL4})	3.17 mm	[0.5, 5]
Length TL5 (L_{TL5})	0.83 mm	[0.5, 5]
Length TL6 (L_{TL6})	1.75 mm	[0.5, 5]
Length TL7 (L_{TL7})	0.99 mm	[0.5, 5]
Length TL8 (L_{TL8})	1.60 mm	[0.5, 5]

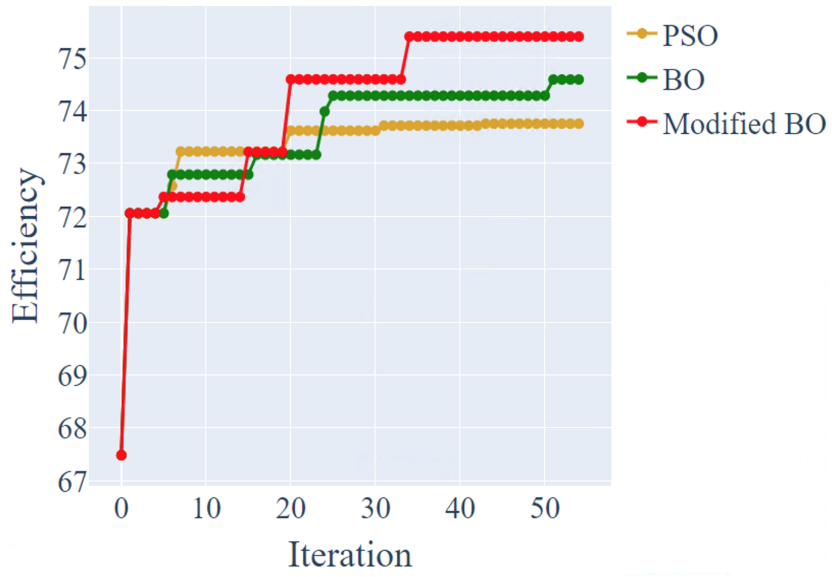

Figure 5.13: Efficiency comparison between the design from PSO, the conventional BO, and the proposed modified BO.

the conventional BO. This shows a time saving of 62%.

In addition to maximizing the efficiency of the WPT system design, one important metric is reducing the coil area. Another example is conducted where the area of the coil is minimized by including it in the objective function. This objective function of a multiple-objective optimization problem can be defined as:

$$f(\boldsymbol{x}) = \sum_{i=1}^{N} w_i f_i(\boldsymbol{x}) \tag{5.33}$$

where $f_1(\boldsymbol{x})$ and $f_2(\boldsymbol{x})$ represent the efficiency and the coil area respectively. Here we set $w_1 = 2$ and $w_2 = 1$ indicating more importance given to efficiency. The range of the width/height of RX coil, namely $g_{xy}RX$, is changed to [1, 5] for the optimization problem. $f_1(\boldsymbol{x})$ and $f_2(\boldsymbol{x})$ are normalized according to the function ranges. The objective function convergence between the WPT design using the conventional BO, PSO, and the proposed modified BO is shown in Figure 5.15. As shown in the figure, the modified BO with parameter prioritization uses the beginning 20 random sampling to obtain sensitivity information,

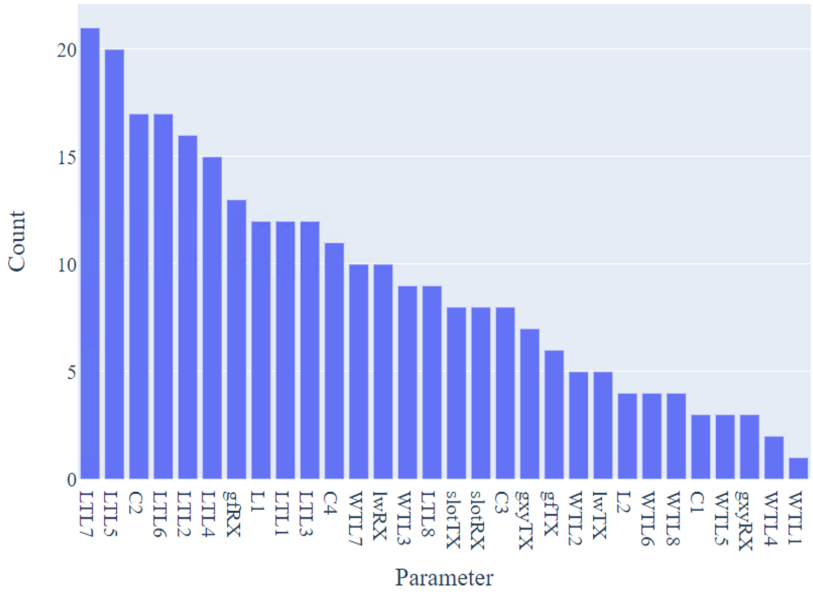

Figure 5.14: WPT parameter sensitivity ranking to efficiency

then a better optimum is found within a small number of iterations. Compared to PSO and the conventional BO approach, modified BO provides better results. The proposed modified BO requires only 29 iterations to reach the maximum efficiency obtained using the conventional BO. The time saved is thus 15%. As shown in Figure 5.16, the parameter sensitivity ranking of $g_{xy}RX$ goes from 28th to 4th, indicating the sensitivity increased while considering the area reduction.

The optimization results are given in Table 5.3. Optimization using the modified BO results in 73.3% RF–DC conversion efficiency and RX coil area of 215.8 mm^2. It outperforms PSO in terms of both the RX coil area and the RF–DC efficiency. The conventional BO provides a similar RX coil area, yet worse RF–DC efficiency. The optimization results from [74] are shown in Table 5.4 and compared. ADD-MES indicates the maximum entropy search with additive GP. DPT-BO indicates the Bayesian optimization with deep partitioning tree, where the hierarchical partitioning tree is used for fast exploration, and the GP is used for exploitation. In all 3 cases, compared with our results, the RX coil areas are smaller, while the RF-DC efficiencies are lower. These different results might be due to the different initial random points, number of simulation iterations, design parameters,

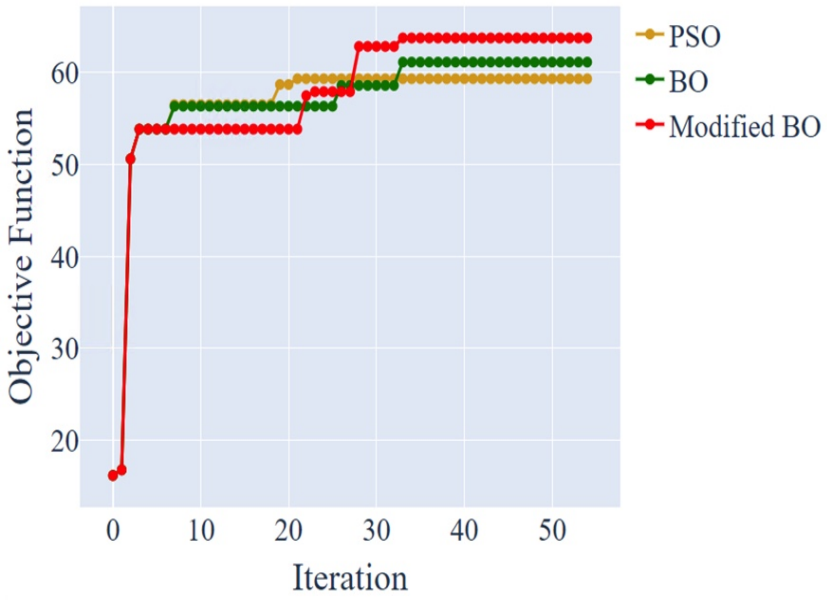

Figure 5.15: Objective function comparison between the design from the PSO, the conventional BO and proposed modified BO.

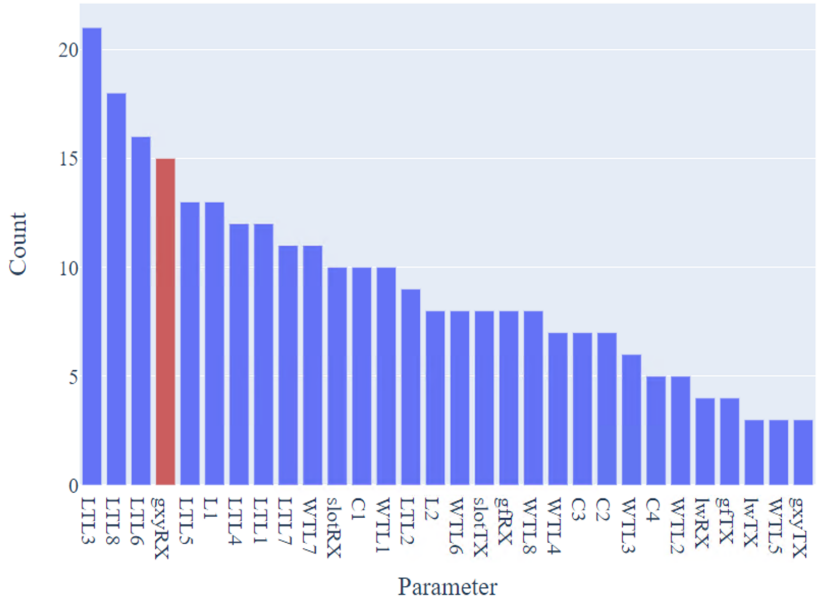

Figure 5.16: WPT parameter sensitivity ranking to efficiency and area reduction

Table 5.3: Optimization results for WPT system

	PSO	**BO**	**Modified BO**
RX Coil Area (mm^2)	230.9	215.5	215.8
RF-DC Efficiency $(\%)$	72.7	72.2	73.3
Number of Simulations	22	34	34
CPU Time (hr)	1	1.4	1.4

Table 5.4: Optimization results for WPT system from [74]

	PSO	**ADD-MES**	**DPT-BO**
RX Coil Area (mm^2)	7.48	19.26	11.04
RF-DC Efficiency $(\%)$	45.83	58.86	59.57
Number of Simulations	192	163	145
CPU Time (minutes)	691.2	603.1	536.5

or design parameter ranges.

In this Chapter, we discuss optimizations of microwave design problems. Since the performance evaluations of RF structure designs involve CPU-intensive and time-consuming electromagnetic simulations, BO can be used to converge to the global optimum by training a surrogate model and choosing the next sampling point in a heuristic manner. The general problem with BO is the low dimensionality of the problem that needs to be addressed which is contrary to microwave design. We propose to prioritize a subset of the design parameters for GP regression and acquisition function optimization in each iteration based on the estimated sensitivity of the parameters. The low dimensional model more concisely

represents the function, thus the solution process provides more improvements compared to the solution obtained directly from the high dimension GP models. The resulting candidate solutions are combined with the previously obtained optimizer solutions in the remaining dimensions to create a new full-dimensional solution used as the next sampling point. We apply this method to the beamforming antenna in package design for wireless communication and the WPT for IoT. The results based on the proposed modified BO show that the optimization is possible with a smaller number of function evaluations. In the beamforming array design example, the proposed modified BO reaches the performance of the manually hand-tuned design in the 20th iteration, while the conventional BO reaches the performance in the 34th iteration. This shows a time saved of 44%. In the WPT system design problem, the proposed modified BO requires only 21 iterations to reach the maximum efficiency obtained using the conventional BO. The time saved is thus 62%. In the multiple-objective case where coil area is also minimized, the time saved is 15% as compared to the conventional BO approach. In both cases, PSO shows unsatisfying results due to the small number of iterations.

CHAPTER 6
SUMMARY AND FUTURE WORK

In **Chapter 1**, an introduction to the EM field characteristic is provided. The RCS is defined as the complex numbered reflection profile of a radar target and is an angular dependent frequency response. The HPC EM emulators are shown to simulate real-time complex EM wave interactions between numerous radar targets. The phased array antenna and wireless power transfer system are two microwave design applications of EM analysis that are also highly related to EM wave propagation.

In **Chapter 2**, we review the literature regarding RCS data compression. This includes the point scatterer modeling, dominant scattering feature analysis, and statistical modeling. We also study the literature on design methods for microwave systems, specifically the antenna designs targeting minimal sidelobe effects. These design methods used optimization techniques with iterative algorithms and successfully minimized the interference from other radiating sources, which degrades the antenna performance. We also discuss the general bottlenecks regarding to high dimensional optimization problems, which is commonly encountered in microwave designs.

In **Chapter 3**, the problem of point scatterer modeling is defined. The reflection profile of a radar target can be represented as a point scatterer model, which consists of a number of isotropic or anisotropic scatterers. Constructing an isotropic point scatterer model means finding the positions and the angular independent reflection gains for all scatterers, while constructing an anisotropic point scatterer model means finding the positions and the angular dependent reflection gains for all scatterers, which best represent a given radar target. Two channel modeling methods are defined where each has its advantages in simulating EM wave propagation. Then, we proposed four point scatterer modeling methods, shape

approximation, anisotropic ellipsoid scatterer modeling, isotropic sphere point scatterer modeling, and spherical harmonic based anisotropic point scatterer modeling. Simulations are provided to show the advantages of each modeling method.

In **Chapter 4**, we focus on the spherical harmonic based anisotropic point scatterer modeling, which outperforms isotropic sphere and anisotropic ellipsoid scatterer modeling in three aspects: (1) Spherical harmonic functions are orthogonal, therefore the spherical function that represents the RCS can be approximated better, (2) the spherical harmonic based bistatic RCS model is separable, and (3) the model captures the complex-numbered RCS data while the ellipsoid model captures only the RCS power. Spherical harmonic functions frequently used in the area of mathematics and physical science are introduced. We find the model by solving the position and the spherical harmonic coefficients of each scatterer. First, the monostatic RCS modeling is constructed. The problem is defined as a least squares linear problem using two assumptions: (1) The angular dependent reflection gain of each anisotropic scatterer is a linear combination of spherical harmonics, and (2) a finite number of possible scatterer positions are known. In the example, we assume that all scatterers are located in a 10m×10m×10m grid in the local coordinate system. In addition to solving the linear least squares problem, a group sparsity constraint is used to limit the number of scatterers by choosing a limited number of optimal scatterer positions among the finite possible scatterer positions. To construct the bistatic point scatterer model, we assume that the scatterer positions are the same as the positions solved from the monostatic RCS data. This leaves us with the problem of solving the separable spherical functions of the incident and scatter angles for each scatterer. By assuming that these functions are linear combinations of spherical harmonics, the problem becomes solving a number of spherical harmonic coefficients. This can be formulated as a bilinear least squares problem and this problem is solved with the normalized iterative algorithm. Simulation results are provided and show the fitting result between the RCS data and the RCS of the point scatterer model.

Next, we illustrate an efficient method that finds the monostatic point scatterer model of continuous scatterer positions. This is achieved by a greedy scatterer position search using the particle swarm optimization. Due to the large number of function evaluations, the problem was not feasible until we introduce an efficient function evaluation method taking advantage of the matrix structure and reduce the computation time of the algorithm. The computation time is reduced significantly since (1) no extra matrix inversion is required, and (2) the high dimensional multiplication is exempted. Simulations are included to show good fitting between the RCS data and the RCS of the point scatterer model.

To reduce the error and improve the model fidelity of the point scatterer model in future works, one can (1) use more RCS data in the model generation process, (2) increase the number of spherical harmonic basis functions so that the reflection profile of each scatterer becomes more complex, or (3) increase the number of scatterers. Approach (1) and (2) increase the computation time of the point scatterer model generation procedure since the algorithm involves more matrix computations. Approach (3) not only increases the computation time of the model generation procedure, but also slows down the HPC EM emulator since the FIR filter will possess more taps. Therefore, it is important to use as less scatterers as possible. Another interesting research topic is efficient RCS generation. The presented works assume that the complex numbered RCS data is given. Yet, the time required to generate a large number of RCS data is not neglectable. This difficulty increases when the size of the radar object or the signal frequency increases. Thus, it is important to generate RCS data more efficiently while considering the point scatterer model generations. In addition, there exists a limitation to the number of data. That is, as the number of RCS data increases to a certain level, the storage size of $\bar{Q}$ in Equation 4.13 becomes too large and limits the computations. Future works include a point scatterer modeling algorithm targeting larger scale RCS data.

In **Chapter 5**, we discuss optimization problems specifically in the microwave design

area. Bayesian Optimization (BO) is a well-known machine learning based method that enables fast convergence towards a global optimum of low dimensional functions without closed-form expressions. The BO method reduces the computation time by training a surrogate model and choosing the next sampling point in a heuristic manner. Since the microwave design problems involve a large number of parameters, we propose an innovative method that prioritizes only a subset of the design parameters for the Gaussian process (GP) regression and acquisition function optimization in each iteration, where the subset selections are based on the estimated sensitivity of each parameter to the objective function. Such a lower dimensional model more concisely represents the function while treating the contribution from other dimensions as noise. Thus the solution process provides more improvements compared to the solution obtained directly from the high-dimension GP models. The resulting candidate solutions are combined with the previously obtained optimizer solutions in the remaining dimensions to create a new full-dimensional solution which is then used as the next sampling point. We apply this process to two emerging system designs: (1) A beamforming antenna in package design for wireless communication and (2) the wireless power transfer (WPT) for Internet of Things (IoT). The results based on the modified BO described show that the optimization is possible with a smaller number of function evaluations. Future works include studies of EM structure simulation algorithms, acquisition function optimizations, and Gaussian process regression with prior knowledge of parameter sensitivity.

REFERENCES

[1] G. D. Dockery, "Modeling electromagnetic wave propagation in the troposphere using the parabolic equation," *IEEE Transactions on Antennas and Propagation*, vol. 36, no. 10, pp. 1464–1470, 1988.

[2] G. Goubau and F. Schwering, "On the guided propagation of electromagnetic wave beams," *IRE Transactions on Antennas and Propagation*, vol. 9, no. 3, pp. 248–256, 1961.

[3] C. Warren, A. Giannopoulos, and I. Giannakis, "Gprmax: Open source software to simulate electromagnetic wave propagation for ground penetrating radar," *Computer Physics Communications*, vol. 209, pp. 163–170, 2016.

[4] M. I. Skolnik, "Introduction to radar," *Radar handbook*, vol. 2, p. 21, 1962.

[5] W.-T. Chen and H.-R. Chuang, "Numerical computation of human interaction with arbitrarily oriented superquadric loop antennas in personal communications," *IEEE Transactions on Antennas and Propagation*, vol. 46, no. 6, pp. 821–828, 1998.

[6] J. M. Rius, M. Ferrando, and L. Jofre, "High-frequency rcs of complex radar targets in real-time," *IEEE Transactions on Antennas and Propagation*, vol. 41, no. 9, pp. 1308–1319, 1993.

[7] R. H. Bartels and G. H. Golub, "The simplex method of linear programming using lu decomposition," *Communications of the ACM*, vol. 12, no. 5, pp. 266–268, 1969.

[8] S. Boyd, S. P. Boyd, and L. Vandenberghe, *Convex optimization*. Cambridge university press, 2004.

[9] M. Hurst and R. Mittra, "Scattering center analysis via prony's method," *IEEE Transactions on Antennas and Propagation*, vol. 35, no. 8, pp. 986–988, 1987.

[10] L. C. Potter, D.-M. Chiang, R. Carriere, and M. J. Gerry, "A gtd-based parametric model for radar scattering," *IEEE Transactions on Antennas and Propagation*, vol. 43, no. 10, pp. 1058–1067, 1995.

[11] J. B. Keller, "Geometrical theory of diffraction," *Josa*, vol. 52, no. 2, pp. 116–130, 1962.

[12] R. Bhalla and H. Ling, "Three-dimensional scattering center extraction using the shooting and bouncing ray technique," *IEEE Transactions on Antennas and Propagation*, vol. 44, no. 11, pp. 1445–1453, 1996.

[13] H. Ling, R.-C. Chou, and S.-W. Lee, "Shooting and bouncing rays: Calculating the rcs of an arbitrarily shaped cavity," *IEEE Transactions on Antennas and propagation*, vol. 37, no. 2, pp. 194–205, 1989.

[14] R. Bhalla and H. Ling, "A fast algorithm for signature prediction and image formation using the shooting and bouncing ray technique," *IEEE Transactions on Antennas and Propagation*, vol. 43, no. 7, pp. 727–731, 1995.

[15] M. J. Gerry, L. C. Potter, I. J. Gupta, and A. Van Der Merwe, "A parametric model for synthetic aperture radar measurements," *IEEE Transactions on Antennas and Propagation*, vol. 47, no. 7, pp. 1179–1188, 1999.

[16] E. J. Hughes and M. Leyland, "Using multiple genetic algorithms to generate radar point-scatterer models," *IEEE Transactions on Evolutionary Computation*, vol. 4, no. 2, pp. 147–163, 2000.

[17] S.-Y. Wang and S.-K. Jeng, "Generation of point scatterer models using ptd/sbr technique," in *IEEE Antennas and Propagation Society International Symposium. 1995 Digest*, IEEE, vol. 4, 1995, pp. 1914–1917.

[18] K. Schuler, D. Becker, and W. Wiesbeck, "Extraction of virtual scattering centers of vehicles by ray-tracing simulations," *IEEE Transactions on Antennas and Propagation*, vol. 56, no. 11, pp. 3543–3551, 2008.

[19] B. Haywood, W. Anderson, J. Morris, and R. Kyprianou, "Generation of point scatterer models for simulating isar images of ships," 1997.

[20] J. S. Daba and M. R. Bell, "Statistics of the scattering cross-section of a small number of random scatterers," *IEEE Transactions on Antennas and Propagation*, vol. 43, no. 8, pp. 773–783, 1995.

[21] R. H. Delano, "A theory of target glint or angular scintillation in radar tracking," *Proceedings of the IRE*, vol. 41, no. 12, pp. 1778–1784, 1953.

[22] R. J. Mailloux, "Electronically scanned arrays," *Synthesis Lectures on Antennas*, vol. 2, no. 1, pp. 1–82, 2007.

[23] M. A. Zaman and M. Abdul Matin, "Nonuniformly spaced linear antenna array design using firefly algorithm," *International Journal of Microwave Science and Technology*, vol. 2012, 2012.

[24] I. C. Trelea, "The particle swarm optimization algorithm: Convergence analysis and parameter selection," *Information processing letters*, vol. 85, no. 6, pp. 317–325, 2003.

[25] X.-S. Yang and A. Slowik, "Firefly algorithm," in *Swarm Intelligence Algorithms*, CRC Press, 2020, pp. 163–174.

[26] M.-H. Golbon-Haghighi, H. Saeidi-Manesh, G. Zhang, and Y. Zhang, "Pattern synthesis for the cylindrical polarimetric phased array radar (cppar)," *Progress in Electromagnetics Research*, vol. 66, pp. 87–98, 2018.

[27] J. R. Mohammed and K. H. Sayidmarie, "Sidelobe nulling by optimizing selected elements in the linear and planar arrays," in *Array Pattern Optimization*, IntechOpen, 2019.

[28] J. R. Mohammed, "Thinning a subset of selected elements for null steering using binary genetic algorithm," *Progress in Electromagnetics Research*, vol. 67, pp. 147–155, 2018.

[29] R. Haupt, "Optimization of subarray amplitude tapers," in *IEEE Antennas and Propagation Society International Symposium. 1995 Digest*, IEEE, vol. 4, 1995, pp. 1830–1833.

[30] K. Yang, Y. Wang, and H. Tang, "A subarray design method for low sidelobe levels," *Progress In Electromagnetics Research*, vol. 89, pp. 45–51, 2020.

[31] C. Pardue, A. Davis, M. Bellaredj, and M. Swaminathan, "Wireless power transfer integrated board for low power iot applications," in *2017 IEEE Conference on Technologies for Sustainability (SusTech)*, IEEE, 2017, pp. 1–6.

[32] R. Jay and S. Palermo, "Resonant coupling analysis for a two-coil wireless power transfer system," in *2014 IEEE Dallas Circuits and Systems Conference (DCAS)*, IEEE, 2014, pp. 1–4.

[33] A. Laha, A. Kalathy, and P. Jain, "Efficiency optimization of wireless power transfer systems having multiple receivers with cross-coupling by resonantfrequency adjustment of receivers," in *2021 IEEE Energy Conversion Congress and Exposition (ECCE)*, IEEE, 2021, pp. 5735–5742.

[34] H.-D. Lang, A. Ludwig, and C. D. Sarris, "Convex optimization of wireless power transfer systems with multiple transmitters," *IEEE Transactions on Antennas and Propagation*, vol. 62, no. 9, pp. 4623–4636, 2014.

[35] N. Hasan, T. Yilmaz, R. Zane, and Z. Pantic, "Multi-objective particle swarm optimization applied to the design of wireless power transfer systems," in *2015 IEEE Wireless Power Transfer Conference (WPTC)*, IEEE, 2015, pp. 1–4.

[36] J. Bito, S. Jeong, and M. M. Tentzeris, "A real-time electrically controlled active matching circuit utilizing genetic algorithms for wireless power transfer to biomed-

ical implants," *IEEE Transactions on Microwave Theory and Techniques*, vol. 64, no. 2, pp. 365–374, 2016.

[37] A. R. Conn, K. Scheinberg, and L. N. Vicente, *Introduction to derivative-free optimization*. SIAM, 2009.

[38] S. J. Park, B. Bae, J. Kim, and M. Swaminathan, "Application of machine learning for optimization of 3-d integrated circuits and systems," *IEEE Transactions on Very Large Scale Integration (VLSI) Systems*, vol. 25, no. 6, pp. 1856–1865, 2017.

[39] J. Jin, F. Feng, J. Zhang, J. Ma, and Q.-J. Zhang, "Efficient em topology optimization incorporating advanced matrix padé via lanczos and genetic algorithm for microwave design," *IEEE Transactions on Microwave Theory and Techniques*, vol. 69, no. 8, pp. 3645–3666, 2021.

[40] W. Wang, Y. Lu, J. S. Fu, and Y. Z. Xiong, "Particle swarm optimization and finite-element based approach for microwave filter design," *IEEE Transactions on Magnetics*, vol. 41, no. 5, pp. 1800–1803, 2005.

[41] S. Goudos and J. Sahalos, "Microwave absorber optimal design using multi-objective particle swarm optimization," *Microwave and Optical Technology Letters*, vol. 48, no. 8, pp. 1553–1558, 2006.

[42] S. Ülker, "Particle swarm optimization application to microwave circuits," *Microwave and Optical Technology Letters*, vol. 50, no. 5, pp. 1333–1336, 2008.

[43] B. Shahriari, K. Swersky, Z. Wang, R. P. Adams, and N. De Freitas, "Taking the human out of the loop: A review of bayesian optimization," *Proceedings of the IEEE*, vol. 104, no. 1, pp. 148–175, 2015.

[44] N. Srinivas, A. Krause, S. M. Kakade, and M. Seeger, "Gaussian process optimization in the bandit setting: No regret and experimental design," *arXiv preprint arXiv:0912.3995*, 2009.

[45] M. Balandat *et al.*, "Botorch: A framework for efficient monte-carlo bayesian optimization," *Advances in neural information processing systems*, vol. 33, pp. 21 524–21 538, 2020.

[46] P. I. Frazier, "A tutorial on bayesian optimization," *arXiv preprint arXiv:1807.02811*, 2018.

[47] R. Moriconi, M. P. Deisenroth, and K. Sesh Kumar, "High-dimensional bayesian optimization using low-dimensional feature spaces," *Machine Learning*, vol. 109, no. 9, pp. 1925–1943, 2020.

[48] A. Nayebi, A. Munteanu, and M. Poloczek, "A framework for bayesian optimization in embedded subspaces," in *International Conference on Machine Learning*, PMLR, 2019, pp. 4752–4761.

[49] Z. Wang, F. Hutter, M. Zoghi, D. Matheson, and N. De Feitas, "Bayesian optimization in a billion dimensions via random embeddings," *Journal of Artificial Intelligence Research*, vol. 55, pp. 361–387, 2016.

[50] K. Kandasamy, J. Schneider, and B. Póczos, "High dimensional bayesian optimisation and bandits via additive models," in *International conference on machine learning*, PMLR, 2015, pp. 295–304.

[51] H. M. Torun, "Machine learning based design and optimization for high-performance semiconductor packaging and systems," Ph.D. dissertation, Georgia Institute of Technology, 2020.

[52] E. F. Knott, *Radar cross section measurements*. Springer Science & Business Media, 2012.

[53] C. M. STudio, "C st studio suite 2013," *Computer Simulation Technology AG*, 2013.

[54] X.-J. Shan, J.-Y. Yin, D.-L. Yu, C.-F. Li, J.-J. Zhao, and G.-F. Zhang, "Analysis of artificial corner reflector's radar cross section: A physical optics perspective," *Arabian journal of geosciences*, vol. 6, no. 8, pp. 2755–2765, 2013.

[55] K. D. Trott, "Stationary phase derivation for rcs of an ellipsoid," *IEEE Antennas and Wireless Propagation Letters*, vol. 6, pp. 240–243, 2007.

[56] R. Okada, *B787-8 dreamliner*, Online, https : / / grabcad . com / library / b787 - 8 - dreamliner-1 Accessed October 27, 2020.

[57] C. M. S. Manual, "Cst," *Darmstadt, Germany*, 2002.

[58] J. Nocedal, F. Öztoprak, and R. A. Waltz, "An interior point method for nonlinear programming with infeasibility detection capabilities," *Optimization Methods and Software*, vol. 29, no. 4, pp. 837–854, 2014.

[59] E. Huang, C. DeLude, J. Romberg, S. Mukhopadhyay, and M. Swaminathan, "Anisotropic scatterer models for representing rcs of complex objects," in *2021 IEEE Radar Conference (RadarConf21)*, IEEE, 2021, pp. 1–6.

[60] R. A. Kennedy and P. Sadeghi, *Hilbert space methods in signal processing*. Cambridge University Press, 2013.

[61] M. A. Wieczorek and M. Meschede, "Shtools: Tools for working with spherical harmonics," *Geochemistry, Geophysics, Geosystems*, vol. 19, no. 8, pp. 2574–2592, 2018.

[62] J. A. Tropp and A. C. Gilbert, "Signal recovery from random measurements via orthogonal matching pursuit," *IEEE Transactions on information theory*, vol. 53, no. 12, pp. 4655–4666, 2007.

[63] E.-W. Bai and Y. Liu, "Least squares solutions of bilinear equations," *Systems & control letters*, vol. 55, no. 6, pp. 466–472, 2006.

[64] E. Huang, C. DeLude, J. Romberg, S. Mukhopadhyay, and M. Swaminathan, "Spherical harmonic based anisotropic point scatterer models for radar applications using inverse optimization," *IEEE Transactions on Antennas and Propagation*, 2022.

[65] R. Okada, *B787-8 dreamliner*, Online, https : / / grabcad . com / library / b787 - 8 - dreamliner-1, Accessed October 27, 2020.

[66] Z. Wang, A. C. Bovik, H. R. Sheikh, and E. P. Simoncelli, "Image quality assessment: From error visibility to structural similarity," *IEEE transactions on image processing*, vol. 13, no. 4, pp. 600–612, 2004.

[67] H. M. Torun, C. Pardue, M. L. Belleradj, A. K. Davis, and M. Swaminathan, "Machine learning driven advanced packaging and miniaturization of iot for wireless power transfer solutions," in *2018 IEEE 68th Electronic Components and Technology Conference (ECTC)*, IEEE, 2018, pp. 2374–2381.

[68] P. Chen, B. M. Merrick, and T. J. Brazil, "Bayesian optimization for broadband high-efficiency power amplifier designs," *IEEE Transactions on Microwave Theory and Techniques*, vol. 63, no. 12, pp. 4263–4272, 2015.

[69] J. Snoek, H. Larochelle, and R. P. Adams, "Practical bayesian optimization of machine learning algorithms," *Advances in neural information processing systems*, vol. 25, 2012.

[70] C. K. Williams and C. E. Rasmussen, *Gaussian processes for machine learning*. MIT press Cambridge, MA, 2006, vol. 2.

[71] H. M. Torun, M. Swaminathan, A. K. Davis, and M. L. F. Bellaredj, "A global bayesian optimization algorithm and its application to integrated system design," *IEEE Transactions on Very Large Scale Integration (VLSI) Systems*, vol. 26, no. 4, pp. 792–802, 2018.

[72] K.-Q. Huang and M. Swaminathan, "Antennas in glass interposer for sub-thz applications," in *2021 IEEE 71st Electronic Components and Technology Conference (ECTC)*, IEEE, 2021, pp. 1150–1155.

[73] M. Swaminathan, O. W. Bhatti, Y. Guo, E. Huang, and O. Akinwande, "Bayesian learning for uncertainty quantification, optimization, and inverse design," *IEEE Transactions on Microwave Theory and Techniques*, 2022.

[74] M. Swaminathan, H. M. Torun, H. Yu, J. A. Hejase, and W. D. Becker, "Demystifying machine learning for signal and power integrity problems in packaging," *IEEE Transactions on Components, Packaging and Manufacturing Technology*, vol. 10, no. 8, pp. 1276–1295, 2020.